FATIGUE MODELING OF NANO-STRUCTURED CHIP-TO-PACKAGE INTERCONNECTIONS

A Dissertation
Presented to
The Academic Faculty

By

Sau W Koh

In Partial Fulfillment
Of the Requirements for the Degree
Doctor of Philosophy in
Materials Science and Engineering

Georgia Institute of Technology

May, 2009

FATIGUE MODELING OF NANO-STRUCTURED CHIP-TO-PACKAGE INTERCONNECTIONS

Approved by:

Dr. Rao R. Tummala, Advisor
School of Material Science and Engineering
Georgia Institute of Technology

Dr. Ashok Saxena, Co-Advisor
School of Material Science and Engineering
Georgia Institute of Technology

Dr Thomas H. Sanders, Jr
School of School of Material Science and Engineering
Georgia Institute of Technology

Dr. Suresh Sitaraman
School of Mechanical Engineering
Georgia Institute of Technology

Dr. Karl Jacob
School of Polymer, Textile & Fiber Engineering
Georgia Institute of Technology

Date Approved: Nov 25th, 2008

ACKNOWLDGEMENTS

I want to thank my advisors, Dr. Ashok Saxena and Dr. Rao R. Tummala for their guidance, and support in defining the problem and scope of this work. Their tremendous zeal, vast knowledge and infinite patience have been a great source of inspiration for me. Their insight has provided invaluable lessons on both technical and non-technical matters. I also wish to express my gratitude to Dr. Suresh Sitaraman, Dr. Tom Sanders and Dr. Karl Jacob for helping me with valuable suggestions and serving on my committee.

I would like to thank my peers in the MSE department and at the University of Arkansas. I greatly enjoyed working with my fellow group members including Dr. Kip Findley, Dr. Heather Sharpe, Dr. Shuhbra Bansal, Rahul Rajgarhia, Dr. Jeff Evans and Dr. Paul Millet. I owe special thanks to Dr. Douglas Spearot, Dr. Panneer Selvam and Dr. Amy Apon for their technical support in running the molecular dynamics simulations

Most importantly, I would like to thank my family; my brothers, my mom and my Dad for their continued support and encouragement. I could not have graduated without their love and faith in me. Furthermore, I will like to thank XinXin Wu for bringing so much happiness from the past year.

TABLE OF CONTENTS

Page

ACKNOWLELDGEMENTS....iii

LIST OF TABLES....xii

LIST OF FIGURES....xiii

NOMENCLATURE....xiv

SUMMARY....xvi

CHAPTER 1: INTRODUCTION....1

1.1 Introduction....1

1.2 Dissertation Objectives....8

1.3 Overview of the Thesis....9

CHAPTER 2: LITERATURE REVIEW....10

2.1 Off-Chip Interconnect Technologies....10

2.2 Nanocrystalline Materials....14

2.2.1 Synthesis of Nanocrystalline Materials....15

2.2.2 Mechanical Behavior of Nanocrystalline Materials....18

2.2.3 Grain Growth....42

2.3 Summary of Literature Survey....53

CHAPTER 3: ATOMISTIC SIMULATION OF MATERIAL BEHAVIOR....55

3.1 Introduction....55

3.2 Molecular Statics....56

3.3 Molecular Dynamics....58

3.3.1 Governing Equation....58

3.3.2 Time Integration Technique……...59
3.3.3 Periodic Boundaries Condition……………………………………60
3.3.4 Neighbor Lists……………………………….………………62
3.3.5 Ensembles………………...…………………..………………63
3.3.6 Computing Physical Quantities……………………………………68
3.3.7 Inter-Atomic Potentials………………………………...……70
3.3.8 Visualization of Atoms……………………………………….....79
3.4 Nanostructures…………………………………………………….....82
3.4.1 Nanocrystalline Structure……………..…………………………..82
CHAPTER 4: CRACK GROWTH ANALYSIS……………………………..............84
4.1 Proposed Methodology For Crack Growth Analysis......................................84
4.2 Model Verification...89
4.3 Material Properties for Crack Growth Analysis of Interconnects.. 94
4.3.1 Nanocrystalline Material..95
4.3.2 Microcrystalline copper……………………….........................99
4.4 Crack Growth Analysis...101
4.5 Conclusions from Crack Growth Analysis..105
CHAPTER 5: MOLECULAR SIMULATION OF MECHANICAL BEHAVIOR OF SINGLE AND NANOCRYSTALLINE COPPER.............................106
5.1 Introduction……..106
5.2 Single crystal analysis……………...107
5.2.1 Verification of the model used..107
5.2.2 Evolution of the microstructure...109

5.2.3 Temperature and Strain Rate Effect……….................................110

5.2.4 Cyclic Loading…...116

5.3 Nanocrystalline copper...117

5.3.1. Stacking Fault Energy……..…...118

5.3.2 Simulation Model…..121

5.3.3 Monotonic Loading……………………..127

5.3.4 Cyclic Loading……………...136

5.4 Conclusion………………………...147

CHAPTER 6: MOLECULAR SIMULATION OF GRAIN SIZE STABILIZATION DURING CYCLIC LOADING IN ANTIMONY DOPED NANOCRYSTALLINE COPPER...149

6.1 Introduction………...149

6.2 Simulation methodology...150

6.2.1 Inter-Atomic Potential..150

6.2.2 Simulation Model...150

6.3 Monotonic Loading………………………………...................................151

6.4 Cyclic Loading……………...155

CHAPTER 8: CONCLUSIONS AND RECOMMENDATIONS.................................158

REFERENCES..163

LIST OF TABLES

Page

Table 1.1: Fatigue life estimation of solder column……………………..………………..4

Table 3.1: Lennard-Jones Parameters compiled from the literature……………………..72

Table 3.2: Reduce Lennard Jones units…………………………………………….....73

Table 5.1: Summary of the modulus obtained from experiment………………………109

Table 5.2 Summary of the number of grains and the average grain size for each model………………………………………………………………………………123

LIST OF FIGURES

Page

Figure 1.1: Effect of interconnect pitch and substrate properties on the stress experienced by outer most interconnection in a peripheral arrary packages…………………….……3

Figure 1.2: Distribution of maximum principal inelastic strain of a 200µm interconnect on a package with substrate CTE of 18 ppm and chip thickness 640µm ……………..…5

Figure 1.3: The new proposed re-workable nano-interconnections as a new interconnection paradigm………..…………………………………………………….6

Figure 2.1: Schematic of wire bonding………………………………………………..11

Figure 2.2: Schematic of tape automated bonding…………………………………….11

Figure 2.3: Schematic of tape flip chip………………………………………………..12

Figure 2.4: (a) Wide Area Vertical Expansion, (b) Wire on Wafer and (c) G-Helix…….13

Figure 2.5: Nanostructured nickel interconnections using (a) thin conductive adhesives, (b) solder……………………………………………………………………………14

Figure 2.6: Microstructure of ECAE copper subjected to (a) 1 passes (b) 2 passes (c) 4 passes (d) 8 passes (e) 12 passes and (f) 16 passes………….…………………………..17

Figure 2.7: Summary of the experimental data from the literature on grain size dependence of copper specimen's nano-hardness ………………………………...19

Figure 2.8: Summary of the experimental data from the literature on grain size dependence of copper specimen's yield strength…………………………………….20

Figure 2.9: Summary of room temperature strain rate sensitivity m as a function of grain size………………………………………………………………………………22

Figure 2.10: Schematic illustration of fracture in nanocrystalline material postulated by Kumar et al……………………………………………………………………….25

Figure 2.11: Summary of the experimental data from the literature on creep rates of nanocrystalline copper………………………………………………..…………..29

Figure 2.12: Summary of range of stress intensity factors required for growth rate of 10^{-6} mm/cycle in ultra fine grain and nanocrystalline nickels as a function of the maximum stress intensity factor Kmax……………………………………..……………..32

Figure 2.13: The relationship of cyclic stress as a function of the number of cyclic to failure for nanoscale copper at various temperatures…………………..……………34

Figure 2.14: The relationship of cyclic stress as a function of the number of cyclic to failure and the volume fraction of vacancies…………………………..…………34

Figure 2.15: Comparison of crack growth rate from both experimental and simulation results……………………………………………………………...……..…..35

Figure 2.16: Top left and right: bright field-dark field pair showing no indication of dislocation in the grain and (Bottom) another grain that contains a twin, a single dislocation at the boundary and a small dislocation loop…………………….……..38

Figure 2.17: (a) Comparison between the computed stress-strain response to their simulation results and (b) comparison of the contribution of each of the deformation mechanisms to the accumulated shear strain………………………………….....42

Figure 2.18: FIB images of a nanocrystalline Cu film (a) immediately after processing (b) after storage for three months at RT. The size of the marker is 1 μm……………..…..44

Figure 2.19: Effect of sample density [125] on grain growth of copper at room temperature……………………………………………………………..…...46

Figure 2.20: Decrease in shear stress required with increasing number of free dislocations at a tilt grain boundary. Thermal effects are not considered in this model………………51

Figure 2.21: Comparisons of resistivity of nanocrystalline and micro-crystalline nickel and copper………………………………………………………………………….….…53

Figure 3.1: Schematic of a simulation cell with periodic boundary condition in 2d space……………………………..……………………………………………….…….61

Figure 3.2: The Lennard-Jones potential and its force derivative of copper…………..…72

Figure 3.3: Correlation between Lennard-Jones parameters for antimony………………75

Figure 3.4: Schematic of the generalized stacking fault energy…………………………79

Figure 3.5: Visualization technique in molecular simulation: (a) Centro-symmetry parameters (b) slip vector parameter (c) coordination number and common neighbor analysis…………………………………………………………………………………..80

Figure 3.6: schematic of Voronoi decomposition and the resulting nanocrystalline copper constructed using Voronoi Tessellation methodology…………………………………..83

Figure 4.1: Parameters for the semi elliptical cracks……………………………………..…86

Figure 4.2: Plot of the correction factor, F1, versus a/c………………………………….88

Figure 4.3: Copper interconnects measuring 25 µm wide and 20 µm tall……………….89

Figure 4.4: Finite element model of a semi-elliptical crack in a round bar used in this analysis…………………………………………………………………………………...90

Figure 4.5: Comparison between the J-integral results obtained from Newman and Raju, and finite element analyses in this research……………………………………………...91

Figure 4.6: Fatigue crack striations marking on RENE88………………………………92

Figure 4.7: Comparison of experimental measured aspect ratio evolution with respect to the finite element solution……………………………………………………………94

Figure 4.8: A typical nanocrystalline microstructure constructed using Voronoi method………………………………………………………………………………….96

Figure 4.9: Computed grain boundaries volume fraction as a function of grain size…..97

Figure 4.10: The function of elastic modulus as a function of grain boundaries volume fraction……………………………………………………………………………………99

Figure 4.11: Regression of experimental data with Ramberg–Osgood relationship for microcrystalline copper……………………………………………………………….100

Figure 4.12: da/dN- ΔK behavior for nanocrystalline and microcrystalline copper….101

Figure 4.13: da/dN- ΔK behavior for nanocrystalline and microcrystalline copper at lower ΔK values……….....…………………………………………………………..……102

Figure 4.14: Crack evolution of nanocrystalline copper and microcrystalline copper.103

Figure 4.15: Crack growth evolution for nano-crystalline copper with different initial a/c ratio………………………………………………………………………………………104

Figure 5.1: Initial microstructure with <100> and <110> crystal orientation…………108

Figure 5.2: Evolution of the microstructure during tensile loading……………………110

Figure 5.3: Influence of the temperature with different loading rate…………………..…111

Figure 5.4: Relationship of the influence of the strain rate on nucleation stress ….….112

Figure 5.5: Comparison of computed m with experimental result obtained from Wang et al………………………………………………………………………………………..113

Figure 5.6: close agreement between the regressed values and the molecular dynamics values……………………………………………………………………………………..114

Figure 5.7: The relationship of activation volume as a function of temperature………115

Figure 5.8: Comparison of the computed fatigue life of single crystal and experimental fatigue life of microcrystalline copper………………………………………………117

Figure 5.9: Schematic of the model used to reproduced the generalized stacking fault curve……………………………………………………………………………………119

Figure 5.10: Generalized stacking fault curve of copper from three EAM potential from the literature review…………………………………………………………………….120

Figure 5.11: Initial nanocrystalline microstructure of copper………………………….121

Figure 5.12: Grain size distribution for nanocrystalline copper with 5 nm grain size…123

Figure 5.13: Comparison of the grain misorientations density function of the microstructure created in this research with the Mackenzie distribution function…….126

Figure 5.14: Stress strain constitutive relationship as a function of grain size………...128

Figure 5.15: The relationship between grain size and yield strength………………….129

Figure 5.16: Evolution of the volume fraction of disorder atoms as nanocrystalline copper is deformed………………………………………………………………………...…132

Figure 5.17: Evolution of grain rotation as nanocrystalline copper is deformed………133

Figure 5.18: Comparison of strain rate sensitivities with experimental result and single crystal results…………………………………………………………………….…..134

Figure 5.19: Summary of the room temperature strain rate sensitivity m as a function of grain size for nanocrystalline copper…………………………………………………...135

Figure 5.20: Fatigue life for different grain sizes…………………………………….....137

Figure 5.21: Evolution of the microstructure during stress relief………………………138

Figure 5.22: Evolution of the microstructure at the 5th cycles and 30th cycle……..…139

Figure 5.23: Comparisons of the degradation of peak stress with the evolution of microstructure for copper with 20nm under 10% strain range……………………..…140

Figure 5.24: Comparisons of the degradation of peak stress with the evolution of microstructure for copper with 20nm under 1% strain range………………………..141

Figure 5.25: Evolution of the microstructure at the 5th cycles and 30th cycle………141

Figure 5.26: Evolution of grain rotation as the simulation times increases…………143

Figure 5.27: Fatigue life as a function of total strain range………………………….144

Figure 5.28: Fatigue life as a function of temperature……………………………….144

Figure 5.29: Summary of the fatigue life as a function of grain size and temperature.145

Figure 5.30: Summary of the fatigue life as a function of total strain range…………145

Figure 5.31: Comparison of molecular dynamics results and fatigue model results....147

Figure 6.1: Simulation model for 1% antimony doped copper………………………151

Figure 6.2: Stress strain constitutive relationship for antimony doped copper with a grain size of 10nm…………………..…………………………………………………....152

Figure 6.3: Stress strain constitutive relationship for antimony doped copper with a grain size of 20nm……………..………………………………………………………153

Figure 6.4: The relationship of the ultimate tensile strength copper with a grain size of 10nm………………………………………………………………………………154

Figure 6.5: Comparison magnitude of grain rotation between pure nanocrystalline copper and nanocrystalline copper doped with 5% antimony……………………………….154

Figure 6.6: Comparisons of the evolution of microstructure for pure copper and doped copper under a cyclic loading of 1% total strain range………………………………156

Figure 6.6: Comparison of the microstructure before and after fatigue loading (a) the initial microstructure just before loading and (b) pure and (c) doped nanocrystalline copper after 100 cycles…………………………………………………………...157

NOMENCLATURE

ECAE	Equi-channel angular extrusion
FEM	Finite element modeling
nc	Nanocrystalline
mc	Microcrystalline
EAM	Embedded-Atom Method
FCC	Face-centered-cubic crystal structure
GB	Grain boundary
LJ	Lennard-Jones
da/dN	rate of crack growth over number of cycles
NVE	Constant number of atoms, volume, energy ensemble
NVT	Constant number of atoms, volume, temperature ensemble
NPT	Constant number of atoms, pressure, temperature ensemble
LCF	Low cycle fatigue
E	Young's modulus
J	A path independent integral characterizing stress intensity
K	Linear elastic stress intensity parameter
ψ	Grain boundary misorientation angle
d	Average grain diameter
γ_{SF}	Intrinsic stacking fault energy
γ_{USF}	Unstable stacking fault energy

N	Number of atoms
F^i	Force on atom i
a^i	Acceleration of atom i
v^i	Velocity of atom i
T	Temperature
V	Volume of simulation cell
r^{ij}	Separation vector between atoms i and j
Δt	Time step
r_{cut}	Cut-off radius for compiling neighbor lists
k	Boltzmann's constant
ε	Lennard-Jones potential parameter for cohesive energy
σ	Lennard-Jones potential parameter for atomic radius
m	Strain rate sensitivity

SUMMARY

Driven by the need to increase the system functionality and concomitant decrease in the feature size, the International Technology Roadmap for Semi-conductors (ITRS) has predicted that integrated chip (IC) packages will have interconnections with I/O pitch of 90 nm by the year 2018. Lead-based solder materials that have been used for many decades as interconnections in flip chip technology will not be able to satisfy the thermal mechanical requirements of these fine pitch electronic packages. Of all the known interconnect technologies, interconnects such as those made from nanocrystalline copper are the most promising for meeting the high mechanical and electrical performance requirements of next generation devices. However, there is a need to understand their properties of these materials such as deformation mechanisms and microstructural stability. Accordingly, the goal of this research is to study the mechanical strength and fatigue behavior of nanocrystalline copper using atomistic simulations and to evaluate their performance as nanostructured interconnect materials. Mechanical behavior simulations were conducted for single crystal nano-rods and for nano grain size polycrystals.

The results from the crack growth analysis indicate that nanocrystalline copper is in fact a suitable candidate for ultra-fine pitch interconnects applications. This study also predicts that crack growth is a relatively small portion of the total fatigue life of

interconnects under low cycle fatigue (LCF) conditions. Hence, crack initiation life is the main factor in determining the fatigue life of interconnects

The results of simulations conducted on the single crystal nano- rods of copper show that the nucleation stress for dislocation is dependent on temperature but insensitive to strain rate. The limiting deformation mechanism in this case is the nucleation of dislocations.

In the case of nanocrystalline copper, material properties such as elastic modulus and yield strength have been found to be dependent on the grain size. The Hall-Petch and inverse Hall-Petch relationships have been investigated in this research and the highest yield strength of 1.93GPa has been found to be for copper with average grain size of 15nm. Dislocation activity has been found to be the primary deformation mechanism for nanocrystalline copper in the Hall-Petch region with some or minimal grain rotation. On the other hand, simulation results of this research have shown that higher amounts of grain rotation that require grain boundaries sliding is the dominant deformation mechanism in the inverse Hall-Petch regime. Hence, it is shown that there is competition between the dislocation activity and grain boundary sliding as the main deformation mode in nanocrystalline materials and the grain size is extremely important in determining the dominant mode.

This research has also shown that stress induced grain coarsening is the main reason for loss of mechanical performance of nanocrystalline copper during cyclic loading. Further, the simulation results have shown that grain growth during fatigue loading is assisted by the dislocation activity and grain boundary migration. A fatigue

model for nanostructured interconnects has been developed in this research using the above observations. Comparisons between simulation results and experimental results from the literature are used to validate the behavior predicted from the computer simulations based on molecular dynamics (MD).

Lastly, simulation results have shown that addition of the antimony into nanocrystalline copper that readily segregates to the grain boundary will not only increase the microstructure stability during cyclic loading, it will also increase its strength. It is shown that the strength in nanocrystalline copper can be increased by as much as 8% by adding 1.2% atomic fraction of antimony in nanocrystalline copper.

CHAPTER 1

INTRODUCTION

In the past, the primary function of micro-systems packaging was to interconnect, power, cool and protect integrated circuits (ICs). It has been assumed that this focus will lead to systems as the IC integration progresses to SOC or system–on-Chip. But SOC has not materialized and a variety of new directions are currently emerging to achieve systems. One such approach is a concept called SOP or system-on-package ,the end goal of which is a highly miniaturized system with two components-- device component and system component and the system is achieved by interconnecting, powering ,cooling and protecting both such components [1]. A very important part of this approach, therefore, is to design and fabricate interconnections that meet electrical pitch and reliability requirements. This thesis addresses this need by a new and unique approach to interconnections. It is referred to as nano-interconnections.

Currently, there are three main approaches to achieving these convergent systems, namely the system-on-chip (SOC), system-in-package with stacked ICs and Packages (SIP) and system on package (SOP). SOC seeks to integrate numerous system functions on one silicon chip. However, this approach has numerous fundamental and economical limitations which include high fabrication costs and integration limits on wireless communications, which due to inherent losses of silicon and size restriction. SIP is a 3-D packaging approach, where vertical stacking of multi-chip modules is employed. Since all of the ICs in the stack are still limited to CMOS IC processing, the fundamental integration limitation of the SOC still remains. SOP on the other

hand, seeks to achieve a highly integrated microminiaturized system on the package using silicon for transistor integration and package for RF, digital and optical integration [1]. IC packaging is one of the key enabling technologies for microprocessor performance. As performance increases, technical challenges increase in the areas of power delivery, heat removal, I/O density and thermo-mechanical reliability. These are the most difficult challenges for improving performance and increasing integration, along with decreasing manufacturing cost.

Chip-to-package interconnections in microsystems packages serve as electrical interconnections but often fail by mechanisms such as fatigue and creep. Furthermore, driven by the need for increase in the system functionality and decrease in the feature size, the International Technology Roadmap for Semi-conductors (ITRS) has predicted that integrated chip (IC) packages will have interconnections with I/O pitch of 90 nm by the year 2018 [2]. Lead-based solder materials have been used for interconnections in flip chip technology and the surface mount technology for many decades.

The traditional lead-based and lead-free solder bumps will not satisfy the thermal mechanical requirement of these fine pitch interconnects. These electronic packages, even under normal operating conditions, can reach a temperature as high as 150°C. Due to differences in the coefficient of thermal expansion of the materials in an IC package, the packages will experience significant thermal strains due to the mismatch, which in turn will cause lead-free solder interconnections to fail prematurely.

Aggarwal et al [3] had modeled the stress experienced by chip to package interconnect. In his work, he developed interconnects with a height of 15 to 50µm on different substrate using

classical beam theory. Figure 1 shows the schematic of his model and a summary of some of his results.

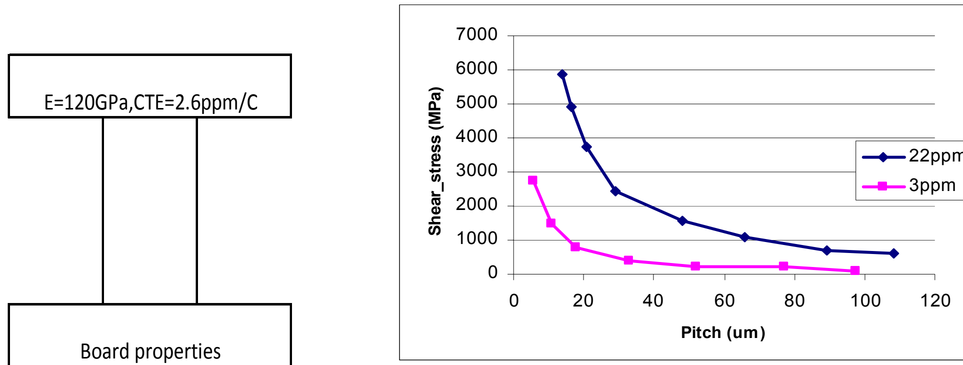

Figure 1.1: Effect of interconnect pitch and substrate properties on the stress experienced by outer most interconnection in peripheral arrary packages.

As shown in Figure 1.1, the shear stress in the joints exceeds the lead-free solders' tensile strength of 26 MPa.

Although compliant interconnects could reduce the stress experienced by the interconnects, it is still insufficient. Chng *et al*. [4] performed a parametric study on the fatigue life of a solder column for a pitch of 100µm using a macro-micro approach. In her work, she developed models of a solder column/bump with a pad size of 50µm and heights of 50 µm to 200 µm. Table 1.1 shows a summary of some of her results.

Table 1.1: Fatigue life estimation of solder column

chip thickness (μm)	250	640	640	640
board CTE (ppm/K)	18	18	10	5
solder column height (μm)	Fatigue life estimation/cycle)			
50	81	N.A	171	3237
100	150	27	276	3124
150	134	31	518	4405
200	74	38	273	5772

It can be seen from Table 1.1 that the fatigue lives of all solder columns are extremely short except for the 5ppm/K board where there is excellent CTE matching. The largest fatigue life of the solder column is only about 518 cycles. As expected, the fatigue life increases significantly when the board CTE decreases from 18ppm/K to 10ppm/K and as the height increases from 50μm to 200μm.This is mainly due to the large strain induced by the thermal mismatch as shown in Figure 1.2. The maximum inelastic principal strain was about 0.16 which exceeds the maximum strain that the material can support. Although the fatigue life of the chip to package interconnection can be increased by increasing the interconnect height, it will not be able to meet the high frequency electrical requirements of the future ICs where they need to be operating at a high frequencies of 10-20 GHz and a signal bandwidth of 20 Gbps,

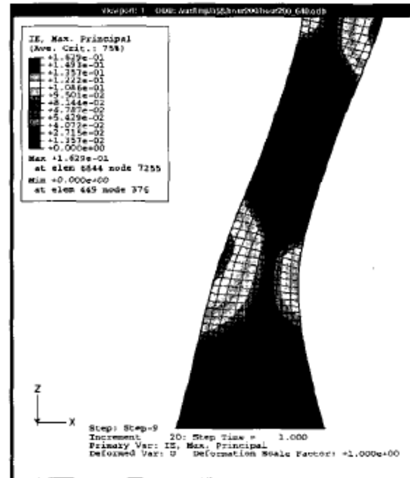

Figure 1.2: Distribution of maximum principal inelastic strain of a 200μm interconnect on a package with substrate CTE of 18 ppm and chip thickness 640μm [4]

The Microsystems Packaging Research Center at Georgia institute of Technology is proposing re-workable nano-interconnections as a new interconnection paradigm, as shown in Figure 1.3, for future low-cost, high performance and high reliability packages [1]. The idea is to use nano-crystalline (nc) copper as interconnection material due to its excellent mechanical and electrical properties.

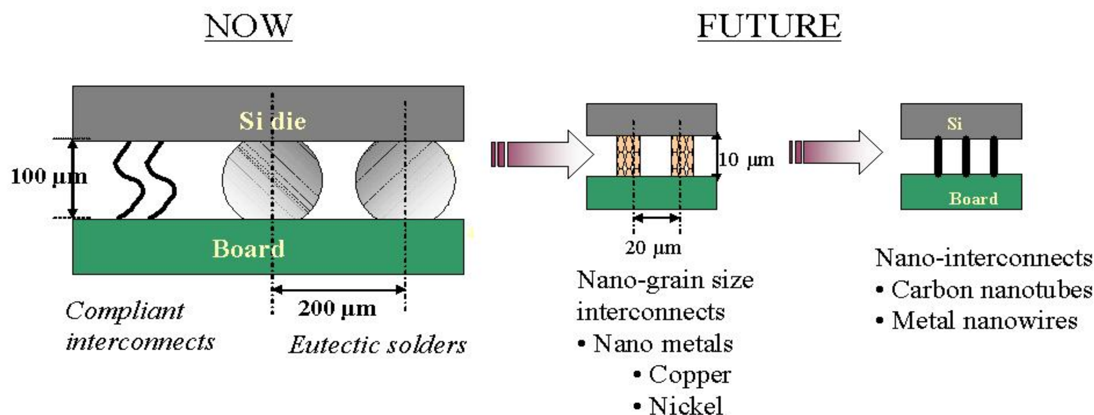

Figure 1.3: The new proposed re-workable nano-interconnections as a new interconnection paradigm [5]

By definition, nanocrystalline materials are materials that have grain sizes less than 100nm and these materials are not new since nanocrystalline materials have been observed in several naturally-occurring specimens including seashells, bone, and tooth enamel [6, 7]. Recently, the nanocrystalline materials have been attracting a lot of research interest due to their superior mechanical and electrical properties as compared to their coarse-grained counterparts. For example, the nano-crystalline copper has about 6 times the strength of bulk copper [8]. The improvement in the mechanical properties due to the reduction in grain size has been well-documented. Increase in strength due to the reduction in grain-size is predicted by the Hall-Petch relationship which has also been confirmed numerically by Van Swygenhoven et al [9] and was first demonstrated experimentally by Weertman [10].

The insertion of nanocrystalline copper as an interconnect material also seems to be feasible from the processing viewpoint. Copper has been used as an interconnect materials since 1989 whereas nano-copper has also been widely processed using electroplating and other severe

plastic deformation techniques in the past few years. For instance, Lu et al. [11] have reported electroplating of nano-copper with grain size less than 100 nm and electrical conductivity comparable to microcrystalline copper. Furthermore, Aggarwal et al [12] have demonstrated the feasibility of using electrolytic plating processes to deposit nanocrystalline nickel as a back-end wafer compatible process. However, several challenges still remain prior to the use of nanocrystalline copper as interconnects materials.

As discussed above, nanocrystalline copper has a high potential of being used as the next generation interconnect for electronic packaging. However, it is vital to understand their material properties, deformation mechanisms and microstructural stability. Although the increase in strength due to the Hall-Petch relationship which has also been confirmed numerically and experimentally by Weertman [10], the improvement in the fatigue properties is not well documented and no model has been established to predict/characterize these nano materials in interconnection application; conflicting results regarding the fatigue properties have also been reported. Kumar et al [13] reported that for nano-crystalline and ultra-fine crystalline Ni, although there is an increase in tensile stress range and the endurance limit, the crack growth rate also increases. However, Bansal et al. [8] reported that with decreasing grain size, the tensile stress range increases but the crack growth rate decreases substantially at the same cyclic stress intensity range. Thus, nanostructured materials can potentially provide a solution for the reliability of low pitch interconnections. However, the fatigue resistance of nanostructured interconnections needs to be further investigated.

Since grain boundaries in polycrystalline material increases the total energy of the system as compared to a single crystal, it will result in a driving force to reduce the overall grain boundary area by increasing the average grain size. In the case of nanocrystalline materials

which have a high volume fraction of grain boundaries, there is a significant driving force for the grains to grow and this presents a significant obstacle to the processing and use of nanocrystalline copper for interconnect applications. Millet et al [14] have shown, through a series of systematic molecular dynamics simulations, grain growth in bulk nanocrystalline copper during annealing at constant temperature of 800K can be impeded with dopants segregated in the grain boundary regions. However, it has been observed that stress can trigger grain growth in nanocrystalline materials [15] and there is no literature available on impeding stress assisted grain growth. There is an impending need to investigate the impediment to grain growth caused by the dopant during fatigue/stress assisted grain growth

1.2 Dissertation Objectives

The goal of present project is to develop a model for the fatigue resistance of nanocrystalline-materials that have been shown to have superior fatigue resistance. Accordingly, the following research objectives are proposed.

- Develop a model for predicting fatigue life of nanostructured chip-to-package copper interconnections
- Develop fundamental understanding on the fatigue behavior of nanocrystalline copper for interconnect application
- Develop an understanding of the stability of nanocrystalline materials undergoing cyclic loading

1.3 Overview of the Thesis

The thesis is organized so that past research on nanocrystalline materials forms the basis of the understanding and new knowledge discovered in this research. Chapter 2 reviews much of the pertinent literature regarding nanocrystalline materials, including synthesis, deformation mechanisms, and grain growth. Chapter 3 describes a detailed overview of the technical aspects of the molecular dynamics simulation method including inter-atomic potentials, time integration algorithms, the isobaric ensembles, isochoric ensembles and modified isobaric ensembles for constant strain rate, as well as periodic boundary conditions and neighbor lists. Chapter 4 describes the simulation procedure designed to investigate and develop the long crack growth analysis. The results of the long crack growth analysis will be presented at the end of Chapter 4. Chapter 5 presents the results and discussion on mechanical behavior of single and nanocrystalline copper subjected to monotonic and cyclic loading whereas Chapter 6 presents the results and discussion on the impediment to grain growth caused by the dopants during fatigue/stress assisted grain growth. Finally, conclusions and recommendations for future work are presented in Chapter 7.

CHAPTER 2

LITERATURE REVIEW

This chapter offers an expanded summary of the literature published on the topics of fabrication methods, characterization, and properties of nanocrystalline materials in addition to a description of existing interconnect technology.

2.1 Off-Chip Interconnect Technologies

Chip-to-package interconnections in microsystems packages serve as electrical interconnections but they often fail by mechanisms such as fatigue and creep. Furthermore, driven by the need for increasing system functionality and decreasing feature size, the International Technology Roadmap for Semi-conductors (ITRS) has predicted that interconnections of integrated chip (IC) packages will have a I/O pitch of 90 nm by the year 2018 [2]. This is a roadmap that semiconductor industry follows closely for projecting their technology needs over several generations. This section reviews some of the current interconnect technology.

Wire bonding [16] as shown in Figure 2.1, is generally considered as one of the most simple, cost-effective and flexible interconnect technology. The devices on the silicon die are (gold or aluminum) wire bonded to electrically connect from the chip to the wire bond pads on the periphery. However, the disadvantages of wire bonding are the slow rate, large pitch and long interconnect length and hence this will not be suitable for high I/O applications.

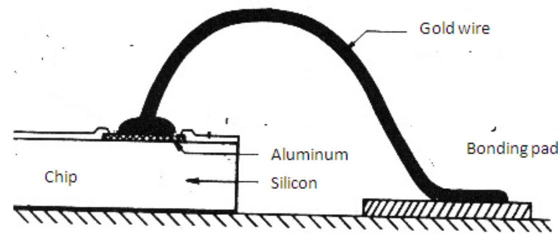

Figure 2.1: Schematic of wire bonding [17]

Instead of wires in the wire bonding, tape automated bonding (TAB) is an interconnect technology using a prefabricated perforated polyimide film, with copper leads between chip and substrate. The advantage of this technology is the high throughput and the high lead count. However, it is limited by the high initial costs of tooling.

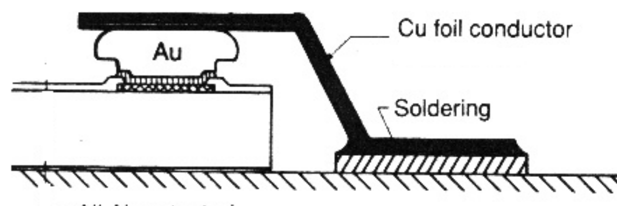

Figure 2.2: Schematic of tape automated bonding [17]

An alternative to peripheral interconnect technology is the area-array solution, as shown in Figure 2.3, that accesses the unused area by using the area under the chip. In area-array packaging, the chip has an array of solder bumps that are joined to a substrate. Under-fill is used to fill the gap between the chip and substrate to enhance mechanical adhesion. This technology gives the highest packaging density and best electrical characteristics of all the available interconnection technologies. However, not only is its initial cost high, it also requires

demanding technology to set up. Furthermore, reliability may be a concern due to the non-compliance of the solder ball.

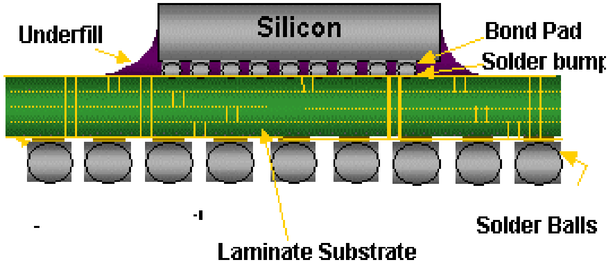

Figure 2.3: Schematic of tape flip chip

With the need for higher I/O density, compliant interconnects have been developed to satisfy the mechanical requirements of high performance micron sized interconnects. The basic idea is to reduce shear stress experienced by the interconnects by increasing their height or decreasing the shear modulus (i.e. increasing their compliance) and hence the name compliant interconnects. Some of the recent research in compliant interconnects includes Tessera's Wide Area Vertical Expansion, Form Factor's Wire on Wafer and Georgia Institute of Technology's Helix interconnects [18-20] as shown in Figure 2.4. Although compliant interconnects can solve the problem of mechanical reliability, it is accomplished at the expense of electrical performance because there is a need to also decrease line delays by reducing electrical connection length to increase the system working frequency. Hence, compliant interconnects may not meet the high electrical frequency requirements of future devices.

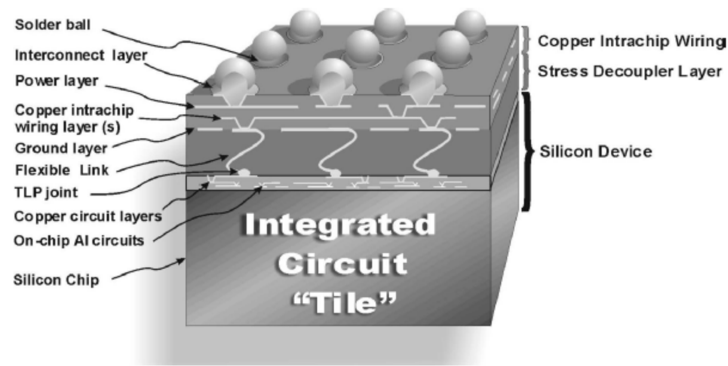

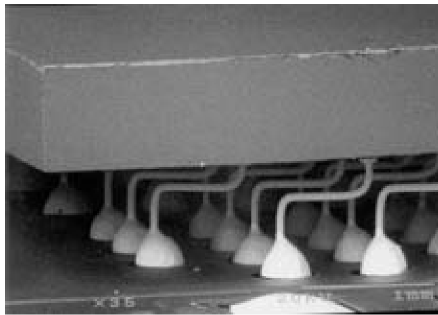

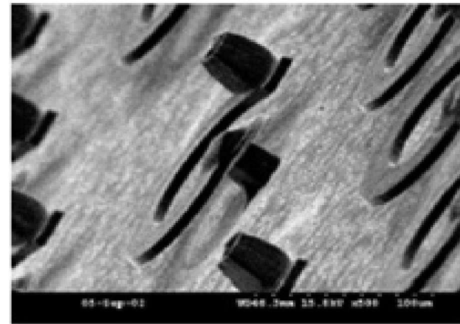

Figure 2.4: (a) Wide Area Vertical Expansion, (b) Wire on Wafer and (c) G-Helix [18-20]

Lead and lead-free solders typically fail mechanically due to their low strength when scaled down to less than to a pitch of 100 μm and as argued earlier compliant interconnections do not meet the high frequency electrical requirements. The Microsystems Packaging Research Center at Georgia institute of Technology has demonstrated the feasibility of using re-workable nanostructured interconnections. Aggarwal et al [21] have shown that nanostructured nickel interconnections, through a Flip Chip test vehicle, were able to improve the mechanical reliability while maintaining the shortest electrical connection length. However, the main disadvantages of this method were the significant signal loss at high frequency signal of nanocrystalline nickel [22].

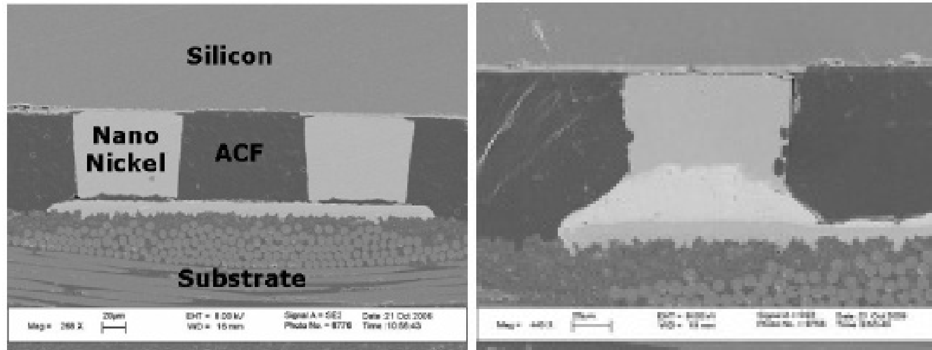

Figure 2.5: Nanostructured nickel interconnections using (a) thin conductive adhesives, (b) solder [21]

As discussed above, nanostructured interconnects technology is the most promising interconnect technology to meet the stringent mechanical and electrical requirements of the next generation devices. Consequently, there is need for alternate materials and nanocrystalline copper because of its high strength and superior electrical conductivity is an excellent candidate. However, due to a tendency for grain growth in nanocrystalline copper under the operating conditions of these packages, there is a major concern about its microstructural stability before using it in interconnects applications.

2.2 Nanocrystalline Materials

Nanocrystalline materials are polycrystalline materials with an average grain size of less than 100 nm [23]. Over the past decade, new nanocrystalline or nanostructured materials with key microstructural length scales on the order of a few tens of nanometers have gained considerable interest among materials scientists and engineers. This is mainly due to their unique and superior properties, such as increased strength [23] and wear resistance [24],

compared to their microcrystalline counterparts. These unique properties are primarily due to the large volume fraction of atoms located at or near the grain boundaries so the properties are representative of both the grain boundary surface characteristics and the grain. In the case of nanocrystalline metals, the high strength is derived from the small grain size but the high grain boundary mobility leading to microstructural instability occurs due to large number of atoms being placed in the grain boundary region. Thus, in order to take full advantage of the enhanced properties, the microstructural instability must be overcome.

2.2.1 Synthesis of Nanocrystalline Materials

Recent advances in synthesis and processing methodology for producing nanocrystalline materials such as inert gas condensation [25], mechanical milling [26, 27], electro-deposition [28], and severe plastic deformation [29] have made it possible to produce sufficient quantities of nanocrystalline materials for small scale application.

Inert gas condensation, the first method used to synthesize bulk nanocrystalline metals [30], consists of evaporating the metal inside a high-vacuum chamber and then backfilling the chamber with inert gas [31]. These evaporated metal atoms would then collide with the gas atoms, causing them to lose kinetic energy and condense into a powder of small nano-crystals. The powder is then compacted under high pressure and vacuum into nearly fully dense nanocrystalline solids. The grain size distribution obtained from this method is usually very narrow. However, the major draw backs of this method are its high porosity levels and other sintering defects. Grain coarsening also occurs due to the high temperature during the compaction stage [32].

Mechanical milling consists of heavy cyclic deformation of powders until the final composition of the powder corresponds to a certain percentages of the respective initial constituents [26, 27]. A wide grain size distribution is obtained by this method. This technique is a popular method to prepare nanocrystalline materials because of its applicability to any material and simplicity. However, it's main drawback includes contamination and grain coarsening during the consolidation stage.

Electro-deposition consists of using electrical current to reduce cations of a desired material from an electrolyte solution and coating a conductive object on the substrate. Electro-deposition has many advantages over other processing techniques and this includes its applicability to a wide variety of materials, low initial capital investment requirements and porosity-free finished products without a need for consolidation processing [28]. Furthermore, Shen et al. [33] and Lu et al[34] had recently showed that the right electro-deposition condition can produce a highly twinned structure which will lead to enhanced ductility. The main drawback of this method is the difficulty to achieve high purity.

Severe plastic deformation, such as high-pressure torsion, equal channel angular extrusion (ECAE), continuous confined shear straining and accumulative roll-bonding, uses extreme plastic straining to produce nanocrystalline materials by mechanisms such as grain fragmentation, dynamic recovery, and geometric re-crystallization [35]. It is the only technology that transforms conventional macro-grained metals directly into nanocrystalline materials without the need for potentially hazardous nano-sized powders. This is achieved by introducing very high shear deformations into the material under superimposed hydrostatic pressure. Two of the most commonly used methods are high-pressure torsion and ECAE [36]. In the study of the effect of ECAE on the microstructure of nanocrystalline copper, Dalla Torre et al [37] observed

that the grains become more equi-axial and randomly orientated as the number of passes increases, as shown in Figure 2.6.

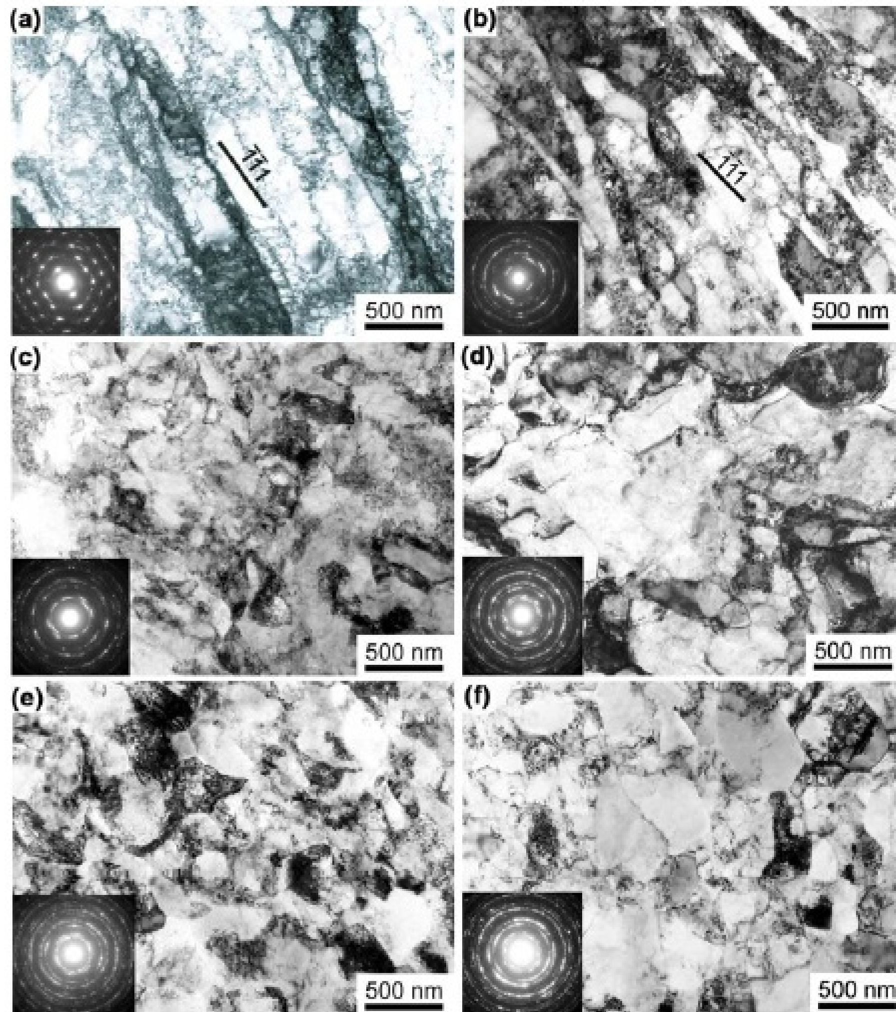

Figure 2.6: Microstructure of ECAE copper subjected to (a) 1 passes (b) 2 passes (c) 4 passes (d) 8 passes (e) 12 passes and (f) 16 passes [37]

2.2.2 Mechanical Behavior of Nanocrystalline Materials

Due to its small grain size and high volume fraction of grain boundaries, nanocrystalline materials exhibit significantly different properties and behavior as compared to their microcrystalline counterparts. The structure and mechanical behavior of nanocrystalline materials has been the subject of considerable interest recently, both experimentally [38-44] and theoretically [45-51]. This section reviews the principal mechanical properties and behavior of nanocrystalline materials.

2.2.2.1 Strength and ductility

Recent studies have shown that metals have five to ten times the strength and hardness compared to their microcrystalline state [8, 37, 38, 52, 53]. This increase in the strength is due to the presence of grain boundaries impeding the nucleation and movement of dislocations. Since decreasing grain size increases the number of barriers and thus the applied stress necessary to move dislocations across grain boundaries, this result in much higher yield strength. The inverse relationship between grain size and strength is characterized by the Hall-Petch relationship [54, 55] as shown in equation (2.1).

$$\sigma = \sigma_0 + \frac{k}{\sqrt{d}} \qquad \text{Eq (2.1)}$$

In equation (2.1), σ is the yield strength, k is a material constant and d is the average grain size. Hence, nanocrystalline materials are expected to exhibit higher strength as compared to their

microcrystalline counterpart. Figure 2.7 and Figure 2.8 show the summary of hardness and yield strength from tensile test that are reported in the literature. Indeed, hardness and yield strength of copper with a grain size of 10nm (3GPa) can be one order higher than their microcrystalline counterpart.

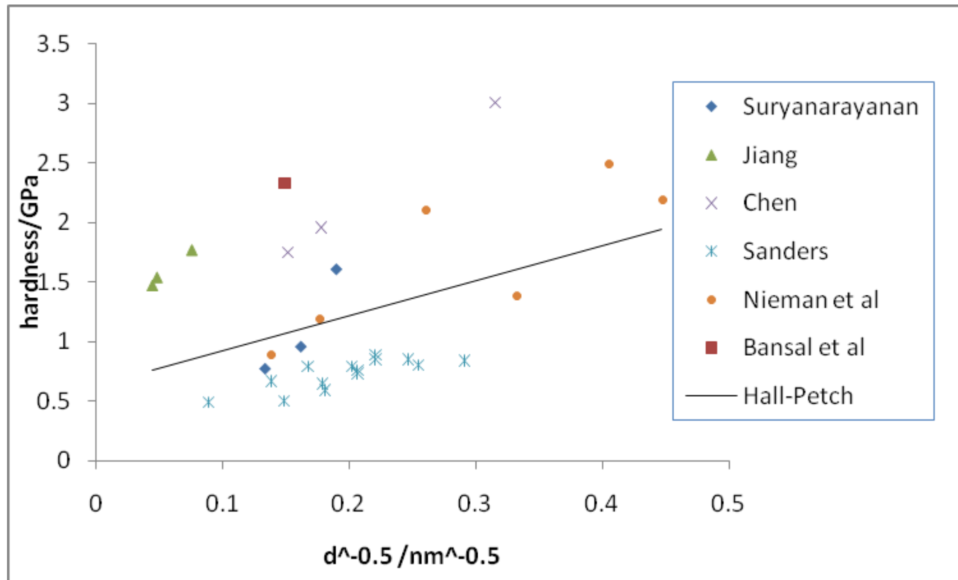

Figure 2.7: Summary of the experimental data from the literature on grain size dependence of copper specimen’s nano-hardness [52, 56-59]

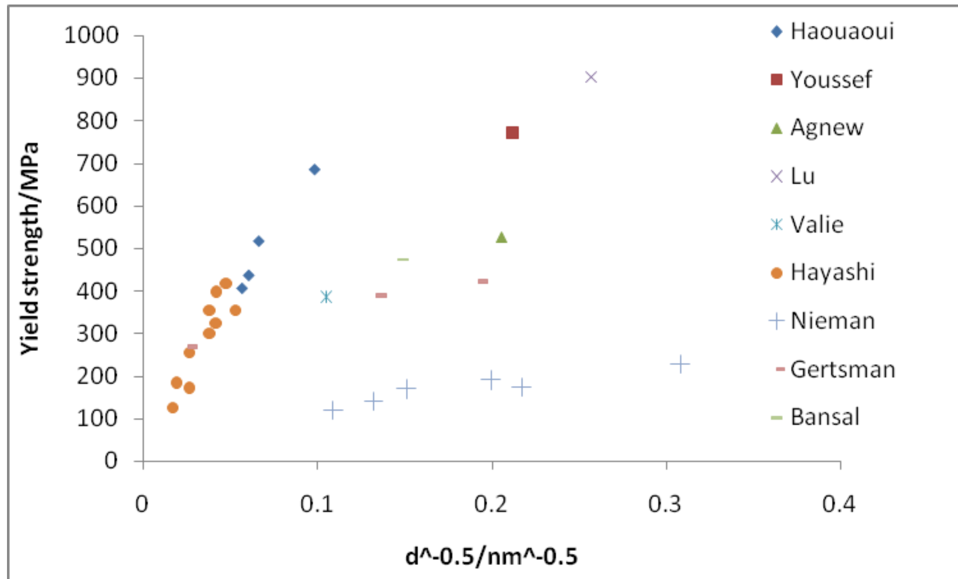

Figure 2.8: Summary of the experimental data from the literature on grain size dependence of copper specimen's yield strength [32, 57, 60-64]

As shown in Figure 2.7 and Figure 2.8, there is a significant scatter in the data from the literature with more deviation at smaller grain size. One of the reasons could be the significantly different processing routes used in the various studies. For example, nanocrystalline and ultra fine grain materials produced from severe plastic deformation have additional barriers to motion of dislocation due to the formation of dislocation walls, cells and sub-grain boundaries. Furthermore, smaller specimen will normally show higher strength as compared to the larger specimens. The specimens in Agnew et al [32] were much larger than that of Nieman et al [57] and this increased the possibility of larger interior and surfaces flaw for the latter and hence resulting in a lower strength for the latter.

Derivation from Hall-Petch relationship begins as the grain size approaches 30nm where the stresses needed to activate the dislocation multiplication via Frank-Read sources within the grains are too high and the plastic deformation is instead accommodated by grain boundaries sliding and migration [13]. Furthermore, as the grain size reduces, the volume fraction of the grain boundaries and the triple points increases. Material properties will be more representative of the grain boundary activity [65] and this will result the strength to be inversely proportional to grain size instead of square roots of the grain size as predicted by Hall- Petch relation [66]. Further reduction in the grain size will result in grain boundary processes controlling the plastic deformation and reverse Hall-Petch effect, where the materials soften, will take place. The earlier experimental observation of reverse Hall-Petch effect[25] was confirmed by Van Swygenhoven et al [67] and Schiotz et al [48], using molecular dynamics simulations Their results showed that nanocrystalline copper had the highest strength (about 2.3GPa) at a grain size of 8nm and 10-15nm, respectively. Conrad et al [68] pointed out that below this critical grain size, the mechanisms shifted to grain boundary–mediated from dislocation-mediated plasticity and this causes the material to become dependent on strain rate, temperature, Taylor orientation factor and the type of dislocation.

Figure 2.9 shows a summary of strain rate sensitivity m as a function of grain size for copper specimens in the literature [52, 69-71]. The strain rate sensitivity, m, in equation 2.2 is an engineering parameter which measures the dependency of the strain rate. From figure 2.8, it was observed that yield stress of nanocrystalline copper was highly sensitive to strain rate even though it is a FCC material. This was due to the high localized dislocation activities at the grain boundaries which results in enhanced strain rate sensitivities especially for materials with a grain size below 0.1 μm.

$$m = \frac{\partial \log\sigma}{\partial \log\dot{\varepsilon}}\Big|_{\varepsilon,T} \quad (2.2)$$

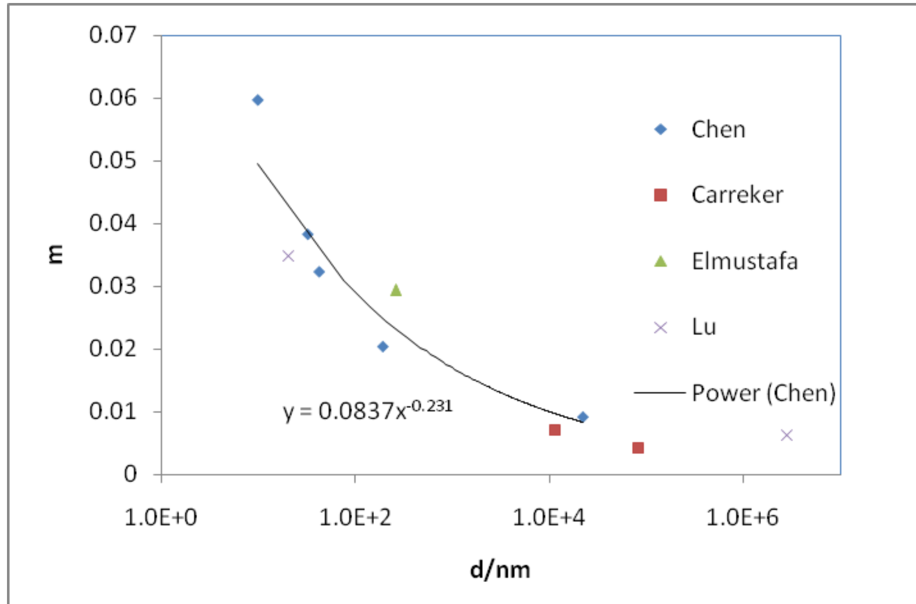

Figure 2.9: Summary of room temperature strain rate sensitivity m as a function of grain size [52, 69-71]

Room temperature strain rate sensitivity was found to dependent on dislocation activities and grain boundaries diffusion [53, 72, 73]. Due to the negligible lattice diffusion at room temperature, the rate controlling process for microcrystalline copper was the gliding dislocation cutting through forest dislocations, resulting in low strain rate sensitivities. However, due to the increasing presence of obstacles such as grain boundaries for nanocrystalline materials, the rate controlling process for smaller grain size shifted to the interaction of dislocation and the grain boundaries, a process that is strain rate and temperature dependent. By considering the length

scale of the dislocation and grain boundaries interaction, Cheng et al [53] proposed the following model for strain rate sensitivities.

$$m = \frac{kT}{\xi b\left(\alpha a + \frac{a\beta}{\sqrt{\rho d}}\right)}. \tag{2.3}$$

In equation 2.3, ζ is the distance swept by the dislocation during activation, ρ is the dislocation density and a, α and β are the proportional factors. With this model, they were able to predict higher strain rate sensitivities for nanocrystalline material produced by severe plastic deformation as compared to other techniques. Since the twin boundaries in nanocrystalline or ultra fine grain copper served as barriers for dislocation motion and nucleation which in turn led to highly localized dislocations near the twin boundaries, the strain rate sensitivity of copper with high density of coherent twin boundaries was found to be higher than those without any twin boundaries [34]. Lastly, the increase enhanced strain rate sensitivity in nanocrystalline copper had been credited for it increases in strength and ductility. For example, Valiev et al [61] credited the enhanced strain rate sensitivity of 0.16 for the high ductility.

In addition to a strong dependency on the strain rate, strength in nanocrystalline materials was also highly dependent on temperature. Wang et al [74] observed that the yield strength for ultra fine grain copper with a grain size of 300nm increased from approximately 370MPa to 500MPa when the temperature reduced from room temperature to 77K. The authors attributed this phenomenon of increase yield strength due to the absence of additional thermal deformation processes at 77K. This is consistent with Huang et al [75] observation where an increase in hardness of nanocrystalline copper with a decreased the temperature was noted

Ductility is another important characteristic of nanocrystalline materials. In microcrystalline materials, a reduction in grain size will increase the ductility due to the presence of grain boundaries acting as effective barriers to the propagation of micro-cracks [76]. However, this is not true for nanocrystalline copper as they had showed a lower strain to failure than that of their microcrystalline counterparts. This reduced ductility was attributed to the presence of processing defects [77]. Recent advanced in processing of nanocrystalline materials offer materials with fairly good ductility in addition to ultra-high strength. Although Basal [8] had reported only about 2% elongation to failure in her ECAE copper, Lu et al [11] reported that nanocrystalline copper with minimal flaw produced via electro-deposition had an elongation to fracture of 30%. Furthermore, Youssef et al [78] observed a 15.5% elongation to failure for defect free nanocrystalline copper produced via mechanical milling. Hence, it was possible for nanocrystalline copper to be both strong and ductile if the processing artifacts are minimized.

Noting the failure morphology of nanocrystalline materials usually consists of dimples several times larger than their grain size, Kumar et al [79] presented the following model as shown in Figure 2.9 for initiation and hence the eventual failure of nanocrystalline materials. In another studies, noting the ratio of strain hardening rate to prevailing stress in nanocrystalline materials, shear localization was found to be responsible for the presence of shear region [80, 81].

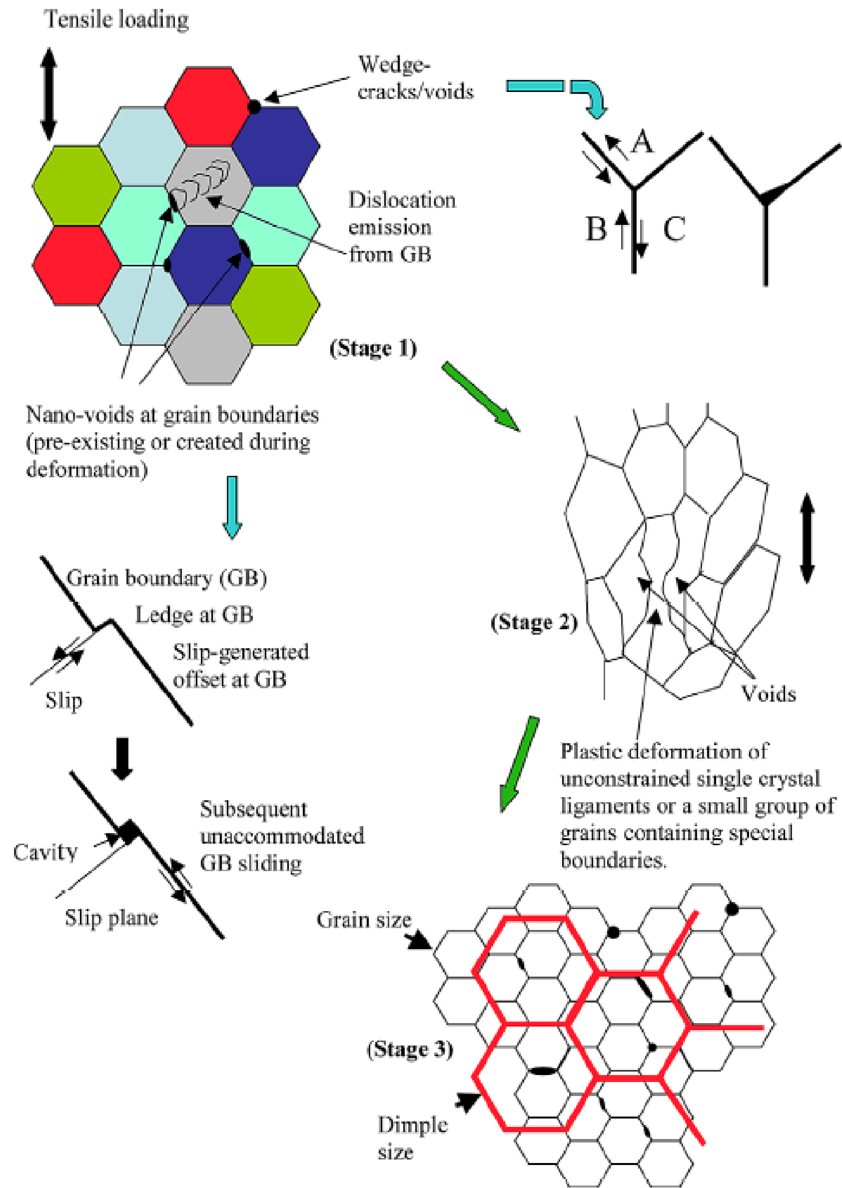

Figure 2.10: Schematic illustration of fracture in nanocrystalline material postulated by Kumar et al [79]

2.2.2.2 Creep in Nanocrystalline Materials

Nanocrystalline materials are expected to creep at temperatures much below the creep temperatures associated with their microcrystalline parts. Due to the higher fraction of grain boundaries and triple junctions, self diffusivity of nanocrystalline copper had been shown to increase by factor of three as compared to microcrystalline copper [82]. Since creep behavior is dependent on both the grain size and diffusivity, with creep rate increases with an increase in diffusivity or a decrease in grain size, the creeping temperature for nanocrystalline copper was known to reduce to a smaller fraction of melting temperature (about 0.22 of its melting point in degrees Kelvin). Furthermore, since creep had always been cited as one of the reason for grain size softening and grain growth in nanocrystalline materials, it has gained considerable attention from researchers.

Due to the high volume fraction of grain boundaries and enhanced diffusivity rate, diffusion creep is considered to be dominant. In general, the steady state creep rate of microcrystalline materials at high temperature was described by Bird-Dorn Mukherjee equation [83]

$$\dot{\varepsilon} = \frac{AD_oGb}{kT}\left(\frac{b}{d}\right)^p\left(\frac{\sigma}{G}\right)^n \exp\left(\frac{Q}{RT}\right) \tag{2.4}$$

where $\dot{\varepsilon}$ is the strain rate, A is a dimensionless constant, G is the shear modulus, b is the magnitude of Burgers vector, k is Boltzmann's constant, R the gas constant, T is the absolute temperature and p is the inverse grain size exponent. The stress exponent n will give an indication of the type of creep mechanism (for example, a value 4-5 for will represent dislocation

climb). Two of the more established creep models that showed linear dependence on stress were the Nabarro-Herring model and the Coble creep model. In Nabarro-Herring model, the creep rate is inversely proportional to the square of the average grain whereas in the case of coble creep model where grain boundaries sliding was the main mechanisms, the creep rate depends on the cube of its average grain size as shown in equation 2.5 and 2.6 respectively.

$$\dot{\varepsilon}_{NH} = \frac{28 D_L G b}{kT}\left(\frac{b}{d}\right)^2\left(\frac{\sigma}{G}\right) \tag{2.5}$$

where D_L is the lattice diffusion coefficient

$$\dot{\varepsilon}_{CO} = \frac{148 D_{gb} \Omega \delta \sigma}{\pi k T d^3} \tag{2.6}$$

where D_{gb} is the grain boundary diffusion coefficient, Ω is the activation volume and δ is the grain boundaries thickness,

As discussed above, nanocrystalline copper at room temperature was expected to creep due to its smaller grain size and enhanced diffusivity rate. However, some of the experimental results had been contradicting. Using equation 2.6 and parameters from Cai et al [84], the Coble creep rate should be in the order of $1\text{x}10^{-6}$/s for a effective stress of 25MPa and a temperature of 373K. However, Sanders et al [85] observed that the creep rates for nanocrystalline copper, over a range of temperature and stress, was two to four orders lower than that predicted by Coble creep model. Neiman et al [86] reported the same trend at room temperature for nanocrystalline

copper produced by inert gas condensation. Since low angle grain boundaries is known to resist grain boundary sliding and inhibit vacancy diffusion, they had concluded that the lower creep rate can be due to the presence of low angle grain boundaries. Lastly, the twin boundaries and the small grain size was cited as the other two main reasons for the lower creep rate since they had been found to act as inhibition to dislocation activities.

Bansal et al [8] showed that the creep rates of nanocrystalline copper produced by ECAE was in the order of $1x10^{-9}$/s. Although this was a few orders higher than grain boundaries diffusion predicted by Nabarro-Herring model, it was still three to four orders lower than that predicted by Coble creep model. Furthermore, by comparing the activation energy to that of the grain boundaries diffusion activation energy, she had concluded that creep in nanocrystalline materials was associated with grain boundary diffusion. The existence of a threshold stress below which the steady- state creep rate was negligible showed that the grain boundaries do not act as perfect sources and sinks. Lastly, stress assisted grain growth was also observed in her ECAE copper.

On the other hand, Cai et al [84] showed the creep rate for electrodeposited nanocrystalline copper, at a temperature from 0.22 to 0.24 of the melting temperature, was found to be the similar to that predicted by Coble creep model even though nanocrystalline copper produced by this methods had significant number of low angle grain boundaries. Furthermore, no grain growth had been detected for these temperatures. Similar observation was made by Grabovetskaya et al [87] using nanostructure copper produced by severe plastic deformation with a grain size from 100nm to 300nm Figure 2.11 shows the summary of the experimental data from the literature on creep rates of nanocrystalline copper.

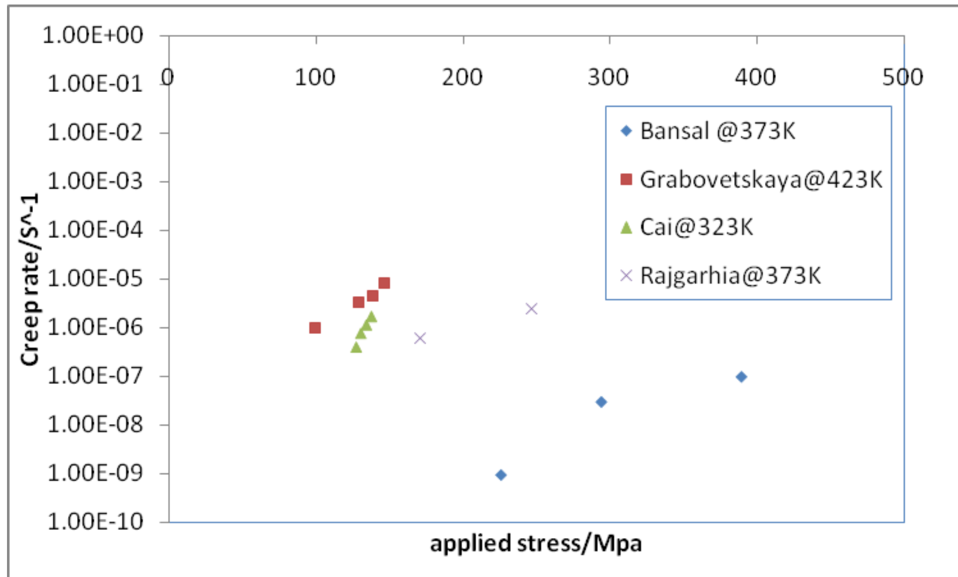

Figure 2.11: Summary of the experimental data from the literature on creep rates of nanocrystalline copper

One of the reasons for the discrepancy in the creep rate could be that none of the mechanisms were the dominant mechanisms. Valiev et al [88] showed that the grain boundary sliding contributions about 15-20% of the overall deformation of nanocrystalline copper with the rest by intra-granular slip. Since different grain size was found to have different dominant mechanism and due to the widely different grain size distribution of nanocrystalline copper, it was then suggested that the creep rate could be a composite of all the mechanisms. Lastly, another source of discrepancy on the computation of creep rate and activation energy was the lack of experimental data on the actual grain boundary thickness and its diffusion coefficient. This will result in more scattering in the literature data.

Yamakov et al. [89] using fully 3D molecular simulation showed that, under high tensile stresses, nanocrystalline palladium exhibits steady-state diffusion creep that could be described by the Coble-creep model. Furthermore, they found that when the grain boundary width was comparable with grain diameter, the creep mechanism changed from Nabarro-Herring creep to Coble creep. Furthermore, the first observation of Lifshitz sliding, an accommodation mechanism for the Coble-creep, had also been observed in that study. Haslam et al. [90] using molecular dynamics simulation showed that at the onset of grain growth, Coble creep was the mechanism for deformation. Furthermore, the enhanced creep rate, arising from topological changes during the initial growth phases, was reported to enhance both the stress-induced grain boundary diffusion fluxes and grain boundary sliding.

2.2.2.3 Fatigue

It has long been known that grain refinement improved the fatigue and fracture resistance of metals. For microcrystalline materials, reducing the grain size increases the fatigue endurance damage tolerance due to decreases in fracture toughness [91]. However, it may not be as straight forward in nanocrystalline materials because fatigue and fracture resistance of these materials are not well understood. This was mainly due to the limited studies conducted on the fatigue of nanocrystalline material.

Witney et al [92] conducted one of the earliest fatigue studies with 97.4–99.3% dense nanocrystalline materials. The nanocrystalline copper samples in their study with maximum stress amplitudes of 50% to 80% of the yield stress and a minimum of 10MPa, showed stress assisted grain growth, with the grain having grown by as much as 34% compared its original

grain size, had also been observed after a few hundred thousand cycles. The cyclic deformation was reported to be elastic. Furthermore, they had also observed parallel micrometer size extrusion on the surface of the specimen. Similar observation was reported by the work of Bansal et al [8] with ECAE nanocrystalline copper. In that study, she had showed that the average grain grew from 45 nm to 56nm for 1% total strain range and to 72nm for 1.5% total strain range. Similarly, she had also reported the formation persistence slip bands in the form of extrusions/ intrusions.

Hanlon et al [93], using electrodeposited nanocrystalline nickel (with average grain size of 20 to 40nm), showed that nanocrystalline nickel not only had a higher endurance limited as compared to their microcrystalline counterpart, it had also showed a significantly higher fatigue crack growth resistance. However, subsequent studies conducted by the same authors showed significantly lower fatigue crack growth resistance for a wide range of load ratios [94]. Figure 2.12 shows the summary of range of stress intensity factors required for a growth rate of 10^{-6}mm/cycle in ultra fine grain nickels as a function of the maximum stress intensity factor K_{max}

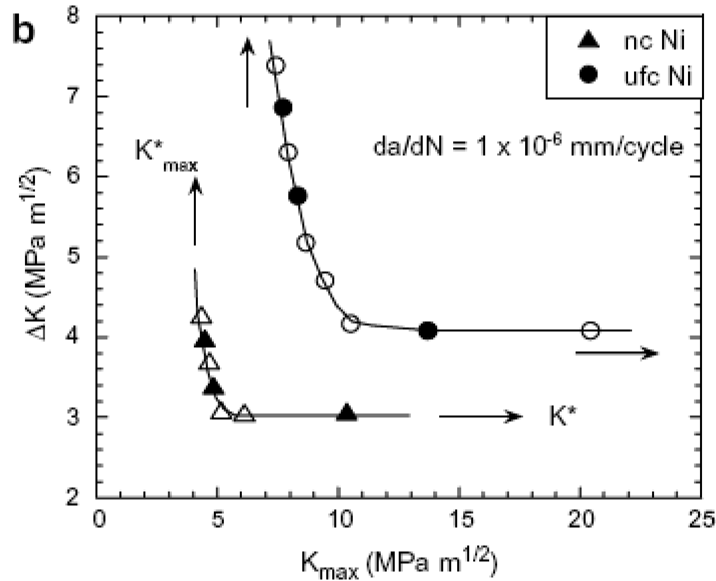

Figure 2.12: Summary of range of stress intensity factors required for growth rate of 10^{-6} mm/cycle in ultra fine grain and nanocrystalline nickels as a function of the maximum stress intensity factor Kmax [94]

Due to the lack of literature data on fatigue life of nanocrystalline materials, ultrafine grain materials had also been studied to understand the mechanisms of grain refinement and grain growth but even these results were very scattered. Agnews et al [95] had observed cyclic softening for ultrafine grain copper, produced by severe plastic deformation, whereas Vinogradov et al [96] did not observed any cyclic softening in their 200nm ultra fine grain copper which was also produced by severe plastic deformation. Furthermore, Hashimoto et al [97] observed grain hardening in equi-axial microstructure but grain softening in elongated grains. Mughrabi et al. [98] observed that a much improved high cycle fatigue life for ultrafine-grained copper produced by severe plastic deformation but low cycle fatigue life was shown to be worse than coarse-grained copper

Since the hardness of the cycled ultra fine grain copper did not scale with the inverse of the square root of the grain size, Agnews et al [95] suggested that the cyclic softening was caused by the decrease in the overall defect density and the changes in the mis-orientation. However, noting a smaller magnitude of cyclic softening and grain coarsening of a -50°C test to that obtained from a room temperature test, Hoppel et al [99] deduced that dynamic cyclic recrystallization process was responsible for the cyclic softening after comparing the microstructure. This prompted them to subject the ultrafine-grained (UFG) copper to recovery heat treatment which resulted in an enhanced fatigue life.

.

In order to have a better understanding of fatigue behavior of nanocrystalline materials, molecular dynamics simulations have also been employed to model the fatigue behavior. Using a model with 960 atoms, Chang et al [100, 101] conducted an investigation on the influence of temperature and vacancy on the fatigue properties of nano-scale copper undergoing tension-compression loading. Due to a higher allowable strain at higher temperature, the fatigue stresses increases with temperature. Figure 2.13 shows a summary of their results. Furthermore, they had observed that the failure transitions from a brittle failure at high stresses to a ductile failure as the number of cycles to failure increases. Figure 2.14 show that the fatigue endurance limited increases as volume fraction of vacancies decreases.

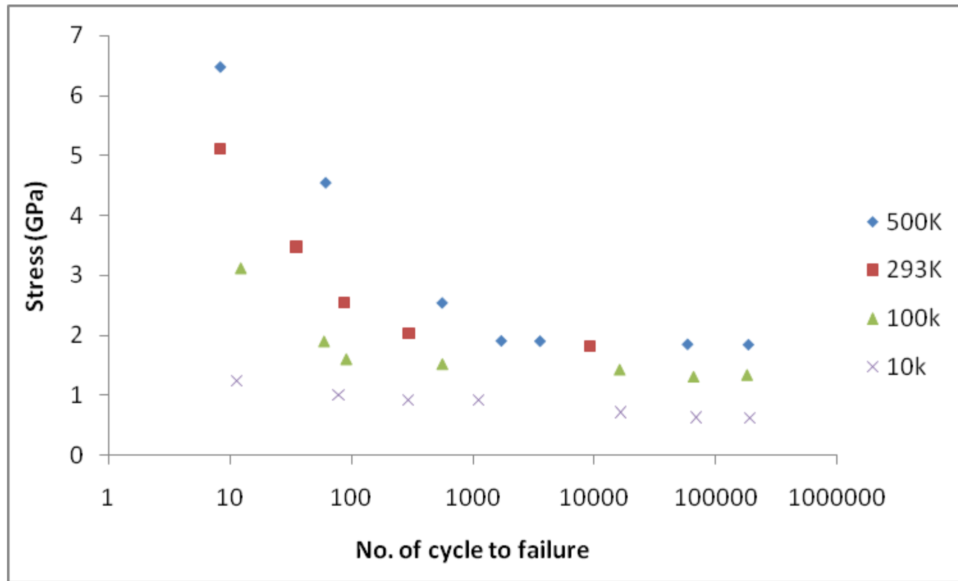

Figure 2.13: The relationship of cyclic stress as a function of the number of cyclic to failure for nanoscale copper at various temperatures [100, 101]

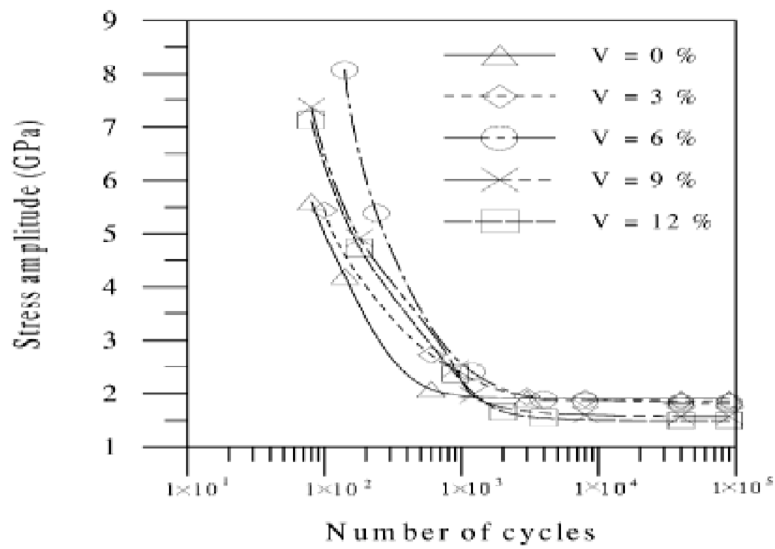

Figure 2.14: The relationship of cyclic stress as a function of the number of cyclic to failure and the volume fraction of vacancies.

In order to investigate the fatigue crack growth mechanisms in nanoscale copper, Farkas et al [102] used molecular dynamics to simulate crack propagation in nanocrystalline nickel with a grain size of 10nm. In that study, they had showed that fatigue crack growth mechanisms of nanoscale copper involved the emission of dislocation from the crack tips and the formation of the nano-voids ahead of the main crack. Although emission of Shockley partials from the grain boundaries and triple points, due to the high stress concentration, were observed, emission of unit dislocations was not observed. Furthermore, Farkas et al [103] showed in a parallel study that the predicted crack growth rates was dependent on the stress intensity amplitude and this appeared to be consistent with experimental results as shown in Figure 2.15

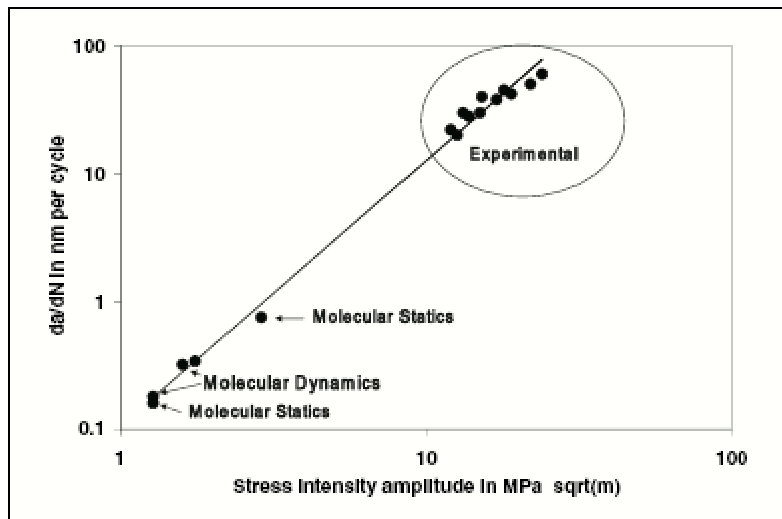

Figure 2.15: Comparison of crack growth rate from both experimental and simulation results

Nishimura et al [104] performed MD simulations on α-Fe undergoing cyclic loading and they had observed that the fatigue crack growth was due to the coalescence of cracks and

vacancies. Furthermore, a phase change from body center cubic to hexagonal close pack was also observed.

2.2.2.4 Deformation mechanisms

Experimental and computational results had shown that the strength of nanocrystalline metals and alloys increases with decreasing grain size. However, the actual mechanisms responsible for the observed behavior of nanocrystalline materials were not established until recently. Computational simulations and electron microscopy had been performed to understand the deformation mechanisms. Dislocation activities were quoted as the primary deformation mode for materials up to certain critical grain size, with the critical grain size depending on the stacking fault energy. Below this critical grain size, grain boundary sliding, grain rotation and Coble creep have been postulated to operate with dislocation activities. In this section, recent studies aimed at uncovering the deformation mechanisms will be presented.

2.2.2.4.1 TEM studies on deformation mechanisms

Kumar et al [79] used ex situ TEM technique to observe deformation of nanocrystalline nickel with a average grain size of 30nm. In that study, dislocation-mediated plasticity was found to be the dominant deformation mechanism with nucleation of voids at grain boundaries and triple junctions caused by the dislocation emission at grain boundaries. Furthermore, intra-granular slip and grain boundary sliding was found to be responsible for the nucleation of voids. However, the density of the dislocation observed cannot account for the high level of imposed plastic strain as shown in Figure 2.16. Hugo et al. [105] had the same observation on the lack of

debris with their magnetron sputtered nickel thin film. This lack of debris could be explained by molecular dynamics simulation studies on aluminum by Derlet et al [106]: after a partial dislocation was emitted from one side of the grain, it will travel across the grain and then absorbed on the other side of the grain, leaving behind very little debris in their path. Furthermore, after the stress had been removed, dislocation might relax and this will cause these dislocations being absorbed by the other grain. The presence of deformation twins and stacking faults found in deformed nanocrystalline copper also suggest that the presence of the partial dislocation mediated processes as one of the deformation mechanisms in nanocrystalline materials [107]. This was confirmed by the work of Wu et al [108] where they observed the partial-dislocation mediated processes during uniaxial tension when the tests are carried out at liquid nitrogen temperature and under high flow stresses. Furthermore, Youngdahl et al [109] observed dislocation pile up at the grain boundaries for nanocrystalline copper of up to 30nm grain size and Wu et al [108] in the study of tensile deformation of nanocrystalline nickel at room temperature, was able to image a full dislocation in 20nm nanocrystalline nickel. Hence, this showed that dislocation activities were still active at that grain size. Furthermore, by showing dislocation storage during liquid nitrogen temperature but not at room temperature, they had shown that the propagation and de-pinning of dislocations were thermally activated and this was consistent with the results from molecular dynamic simulations [110]. However, Ke et al [111] had observed grain rotation of up to 15° in the study on the 10nm grain size gold. This is consistent with Shan et al [112] observation where grain rotation in 10nm nanocrystalline nickel during straining was reported.

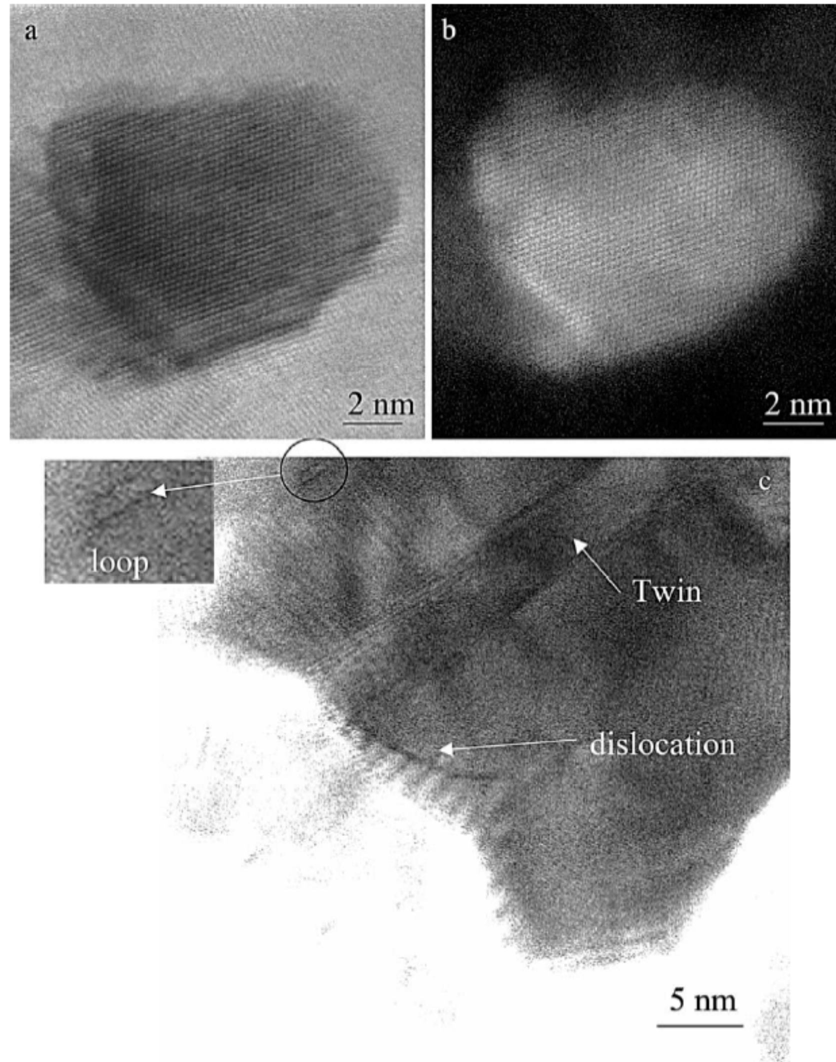

Figure 2.16: Top left and right: bright field-dark field pair showing no indication of dislocation in the grain and (Bottom) another grain that contains a twin, a single dislocation at the boundary and a small dislocation loop [79]

Even though experimental observations have noted isolated dislocation activity, grain boundary sliding and grain rotation is considered to be the main deformation mechanisms for

nanocrystalline materials, there is ample evidence to the contrary. For example, Ke et al [111] have observed grain rotation of up to 15° and no dislocation activity during the deformation of nanocrystalline gold with a grain size of 10nm using in-situ TEM, stress relaxation tests on 30nm grain size nanocrystalline nickel conducted by Wang et al [113] over a range of deformation temperatures (77-373K) have shown that boundary diffusion process such as Coble creep and grain boundary sliding are not the dominant deformation mechanisms. Instead they found that the deformation kinetics was all dominated by dislocation processes.

2.2.2.4.2 Molecular Simulation

In addition to the results from TEM studies, large scale molecular dynamics had also provided insight to the deformation mechanisms in nanocrystalline materials. Room temperature 3D simulation of 30nm nanocrystalline copper and nickel have demonstrated that the nanocrystalline materials accommodated the external applied deformation through grain boundary sliding and emission of partial dislocations [106, 114, 115]. Furthermore, the interaction of these two mechanisms would induce the formation of shear planes where grains with small mis-orientation will coalesce to form a larger grain. Van Swygenhoven et al [116] have identified the ratio of the energy associated with an unstable stacking fault to the stacking fault energy as a criterion for the nucleation of full dislocation: if this ratio was closer to unity, it would be easier for a full dislocation to be nucleated. Hence, this is the reason why only partial dislocations were observed in simulation of nanocrystalline copper in which this ratio is 7.81.

Molecular dynamics simulation have also shown that atomic shuffling, involving short-range atomic motion, in conjunction with emission of partial dislocations as another mechanism for triggering grain boundary sliding and dislocation plasticity. Atomic shuffling not only caused a local change in the grain boundary structure , it will also cause a redistribution of the peak stress [106]. Derlet et al [106] showed that the "*effective stacking fault energy*" reduced up to 50% through structural relaxation after the emission of partial dislocations from the grain boundaries.

Molecular dynamics simulations conducted at a much higher temperature had identified Coble creep mechanism with grain boundary sliding as accommodation mechanism known as Litshitz sliding [89]. However, extrapolation of Coble creep mechanisms to room temperature may not be justifiable as there was no reason to assume that the same rate controlling processes to be dominant at both high temperature and room temperature.

2.2.2.4.3 Theoretical Model

With the insight on the deformation mechanism of nanocrystalline materials gained from both the TEM and molecular simulation studies, constitutive models which could accurately predict the deformation behavior have become available. The only known constitutive models found in the literature was developed by Zhu et al. [117] using crystal plasticity theory and assuming that the grain interiors to be deformed by the emission of perfect or partial dislocations and grain boundary sliding. Since experimental and simulation results identified emission of partial and full dislocations and grain boundaries sliding as the three main deformation mechanisms in nanocrystalline materials, they have developed a physics based model which took

into account of these mechanisms. To account for slip rate caused by the emission of partial dislocation, the following laws were applied.

$$\dot{\gamma} = \dot{\gamma_0} \left\{ \frac{\frac{\tau^{(\alpha)}}{G} - \tilde{\alpha}\Gamma}{g^{(\alpha)}} \right\} \text{ if } \frac{\tau^{(\alpha)} - \tilde{\alpha}\Gamma}{G} > 0 \tag{2.7}$$

Where $g^{(\alpha)} = \frac{b}{3d} + f(n)$

In equation 2.7, $\dot{\gamma_0}$ is the pre-exponential constant, Γ is the stacking fault energy per unit area and α is the equilibrium spacing. Furthermore, in order to account for slip rate caused by the emission of full dislocation, following laws proposed by Asaro et al was used

$$\dot{\gamma} = \frac{b}{3d} + \frac{\alpha - 1}{\alpha}\tilde{\Gamma} \tag{2.8}$$

Lastly, for grain boundary sliding, following law proposed by Conrad et al can been used:-

$$\dot{\gamma} = \frac{6bv_d}{d} \sinh\left(\frac{v\tilde{\tau}}{kT}\right) \exp\left(\frac{-\Delta F}{RT}\right) \tag{2.9}$$

In equation 2.9, υ_D is the frequency of lattice vibration, v is an atomic volume and ΔF is the activation energy for lattice/grain boundary diffusion. Figure 2.17 the computed strains using their model compared pretty well to their computational results.

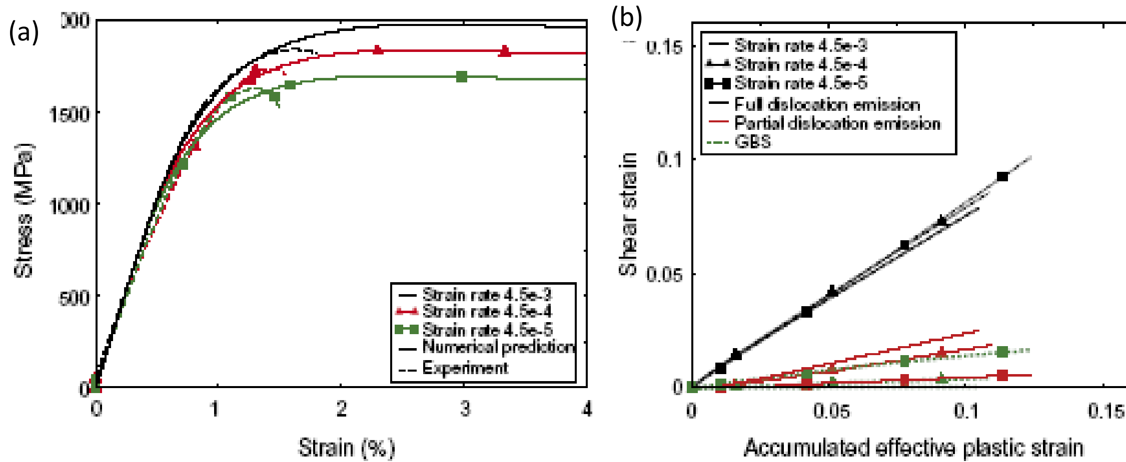

2.17: (a) Comparison between the computed stress-strain response to their simulation results and (b) comparison of the contribution of each of the deformation mechanisms to the accumulated shear strain

Although there are only these constitutive models currently available in the literature, more realistic mechanisms based models will be available as more insight is gained from the experimental and simulation results.

2.2.3 Grain Growth

Since grain boundaries in nanocrystalline materials increase the total energy of the system, there is a driving force to reduce grain boundaries by increasing the average grain size. This presents a significant obstacle to the processing and use of nanocrystalline materials for engineering applications. In order to overcome this obstacle, it is important to understand the underlying mechanisms of grain growth in nanocrystalline materials. However, accurate grain

growth studies in nanocrystalline materials are difficult to conduct due to the difficulty of accurately determining the grain size. Nevertheless, some studies have been conducted by measuring the grain size through direct electron microscopic techniques or through the X-ray diffraction peak broadening values size. However, it is important to note that X-ray diffraction may underestimate the grain size and the small thickness required for TEM may enhance the grain growth rate.

One of the main mechanism for grain growth in micro-crystalline materials is curvature-driven grain boundary migration in which the the grain boundaries move towards the center of their curvature [118]. This curvature in the grain boundaries which is on the order of the inverse of the grain size, arises from the angular equilibrium requirement of triple junctions and this is known as the Herring relation [119]. Due to the high volume fraction of the triple points in nanocrystalline materials, they are especially unstable against grain growth and this will cause grain growth to occur even at a relatively low temperatures. Simulation work by Haslam el al. [120] has identified grain rotation and coalescence as another mechanism for grain growth in nanocrystalline materials. Grain rotation and coalescence is the elimination of the grain boundaries between two grains through grain rotation, leaving behind two highly curved grain boundaries which then further promote rapid grain growth by grain boundaries migration.

Considering the non conservative dislocation motion due to unbalanced forces at the triple points at grain boundaries and using Read-Shockley model for the dependence of grain boundary energy during mis-orientation at low angle and sub-grain boundaries, Li [121] formulated the rate of grain rotation in terms of evolution of inter-dislocation spacing via non conservative dislocation motion. However, this mechanism of grain coarsening is only possible in nanocrystalline materials due to the need for rotational mobility. Furthermore, recent studies

[15, 122, 123] have shown that this mechanism for grain growth can be accelerated considerably by externally-applied stress.

2.2.3.1 Temperature Driven Grain Growth.

Due to the high driving force for grain growth through grain boundary migration and grain rotation for nanocrystalline materials, many nanocrystalline materials including iron[124], copper [125-127], aluminum [128], gold [129] and palladium [25] was found to undergo microstructural coarsening at room temperature. Figure 2.18 shows an example of grain growth in nanocrystalline copper.

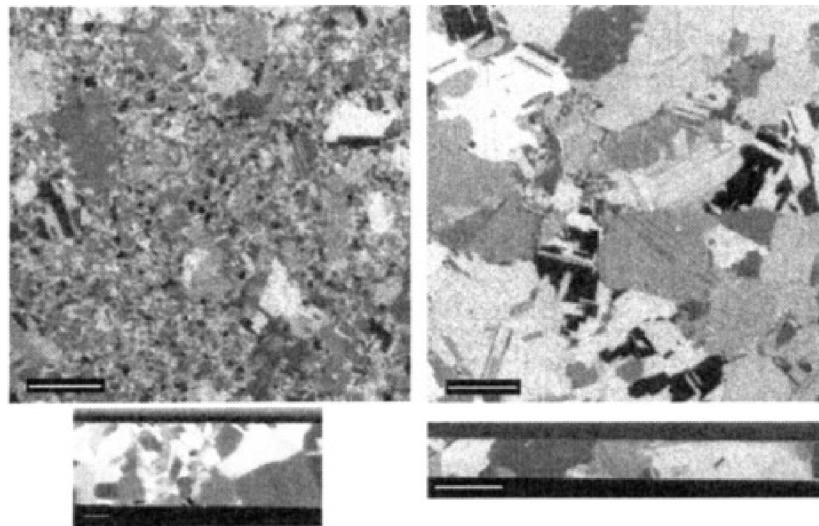

Figure 2.18: FIB images of a nanocrystalline Cu film (a) immediately after processing (b) after storage for three months at RT. The size of the marker is 1 μm.

One of the factors affecting the stability of the grain was identified to be the volume fraction of the low angle grain boundaries. A room temperature grain growth study conducted by Pantleon et al [130] revealed that electrodeposited nanocrystalline copper has greater thermal stability for thin films due to the higher fraction of low angle grain boundaries. Recent molecular dynamics simulations by Spearot et al. [131] verified that low angle grain boundaries had lower energy configurations thus they are not as susceptible to mobility and growth. However, it is also important to note that several high-angle boundaries, such as the M3 (111) symmetric tilt interface, may have very low energies as well.

Another factor affecting the stability of the grain was identified to be the activation energy of grain boundary diffusion. Thermal stability studies conducted by Bansal et al [132], on ECAE nanocrystalline copper and nickel, had shown that nickel was stable at 250°C whereas considerable grain growth was observed in copper at temperatures even as low as 100°C. In that study, the activation energy for grain growth of copper and nickel were calculated to be 33 kJ/mol and 55 kJ/mol, respectively. This apparent activation energy for grain boundary mobility in nanocrystalline copper was much lower than the activation energy of 80-100 kJ/mol for grain growth in microcrystalline copper [133, 134]. Noting that the activation energies for lattice diffusion and grain boundary diffusion for copper are 100 kJ/mol and 49 kJ/mol[135] respectively, she concluded that the underlying mechanism for grain growth in nanocrystalline copper was dominated by the grain boundary diffusion. Similar observation of the lower activation energy for grain growth in nanocrystalline materials and attributing it to the lower activation energy of diffusion of atoms along the grain boundary had been made by Natter et al [136].

The processing route has been identified as another factor that will affect grain growth in nanocrystalline materials. In the thermal stability studies on ECAE copper conducted by Molodova et al. [137], the grain growth rate and their activation energy had been found to be a function of both the grain size and number of passes during ECAE. They had observed that grain growth will occur at lower temperatures for materials with smaller grain size and higher number of ECAE passes.

Furthermore, Gertsman et al. [125] had also showed that the density of the nanocrystalline copper will have some detrimental effect on the grain growth of nanocrystalline copper at room temperature. In their thermal stability studies on ECAE copper, they had observed that grain growth will occur more readily for less dense samples as shown in Figure 2.19. The reason being that the pores in the samples increase self-diffusion in the grains and hence creating greater instability by acting as paths for surface diffusion [138].

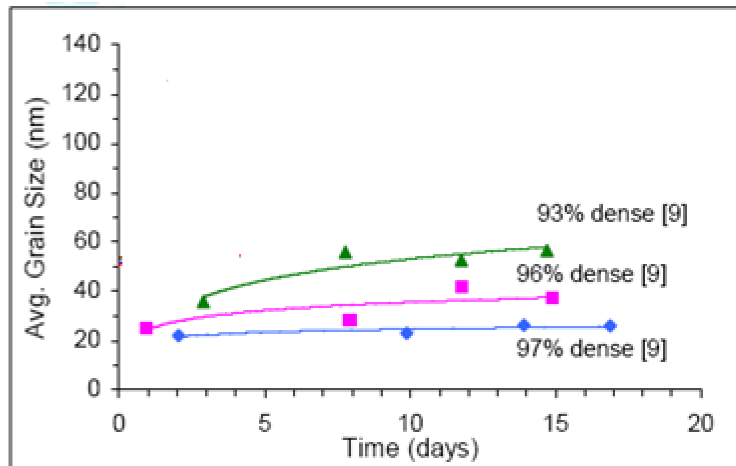

Figure 2.19: Effect of sample density [125] on grain growth of copper at room temperature

2.2.3.2 Stress Driven Grain Growth.

Recent observations on indentation creep experiment in high purity nanocrystalline copper conducted by Zhang et al [15, 139] pointed the possibility of stress induced grain coarsening in nanocrystalline copper. This is because grain growth was observed even though Zhang et al [15, 139] performed these indentations at cryogenic temperatures where thermal and diffusion effects were suppressed. Further confirmation of stress assisted grain growth was provided by the work of Zhu et al [140]. By taking into the account of the effects of the grain growth, they could accurately predict the rapid decrease in hardness during dwell time observed in Zhang et al [15, 139] experiment. Furthermore, stress assisted grain growth has also been observed in nanocrystalline materials during fatigue loading. Bansal et al [132] observed grain growth in nanocrystalline copper during low cycle fatigue tests with a strain ratio of -1. The average grain size increased from 45 nm to 58.5 nm and 72.0 nm at strains of 1.0% and 1.5%, respectively, indicating stress driven grain growth. In addition, Bansal et al [132] observed that a threshold stress was required for grains to grow at a given temperature in the creep experiments conducted using ECAE nanocrystalline copper.

Since understanding the phenomenon of stress induced grain growth is very important for the application of nanocrystalline materials in engineering applications, there is a need to understand the mechanisms for stress induced grain coarsening. Using molecular dynamics simulations, Schoitz [123] was able to simulate stress assisted grain growth of nanocrystalline copper under cyclic loading. In that study, he had identified grain rotation and coalescence as the mechanisms for stress assisted grain growth during severe plastic deformation. Furthermore, Zhang et al [15] concluded that grain rotation and coalescence were the primary grain growth mechanism given the large number of low angle grain boundaries in the vicinity of indentations.

Gai et al [141] had arrived at the same conclusion when they had observed the increased number of small angle grain boundaries as the dwell times increased.

More grain growth studies using molecular dynamics have been conducted by Haslam et al [122] on nanocrystalline palladium under the influence of stress at 1200K . In that study, they had observed grain growth under the influence of stress due to increased diffusion of atoms at the grain boundary. The underlying mechanism for the observed stress induced grain growth was then identified to be mainly due to curvature driven grain boundary migration and grain rotation-induced grain coalescence. Multi-scale simulations of nano-indentation tests conducted at a temperature of 0 K arrived at the same conclusion that grain growth mechanisms in nanocrystalline materials are primarily due to the migration of unstable grain boundaries and grain rotation and coalescence [142].

It was suggested that stress induced grain growth facilitated by grain boundary migration required the presence of extrinsic grain boundary dislocations [26] and the emission of free dislocations from the interface [32]. Hence, nanocrystalline materials with high energy non-equilibrium grain boundaries were more susceptible to stress assisted grain growth. Recent studies by Lu et al. [33] provided the experimental verification of this argument. By comparing the final micro-strain and grain size from both electrodeposited and cold-rolled nanocrystalline copper, they observed that grain growth occurred at the same temperature at which the internal micro-strain was relieved. This result confirmed the relationship between internal micro-strain and grain growth.

A full understanding of grain boundaries migration and grain rotation will require more in-depth studies and no model has been established to describe the phenomenon of stress induced

grain growth. However, for simple geometry such as a tilt boundaries, Gutkin et al [143] have developed a model to describe stress driven grain boundaries migration as a special mode of rotational plastic deformation by taking the account of declination of uncompensated ground boundary junction.

$$\tau_{cr} = \frac{Gb\omega}{2\pi d(1-v)} \ln\left(\frac{d}{b}\right) \qquad (2.10)$$

In equation (2.10), critical shear stress τ_{cr} for boundary motion, *w* is the tilt angle, *b* is the length of the declination dipole and *d* is separation of the dipole. Equation 2.10 showed that the critical shear stress of the range of only 20-300MPa will be sufficient to cause the migration of the grain boundaries for grain between 10nm to 30nm in size and with a misorientation angle of 5° to 30°. Ovid'ko et al [144] then extended this model (equation 2.11) to take into the account of formation of immobile declinations, whose strength gradually increases as a result of grain boundaries sliding and diffusion.

$$\tau_{cr} = \frac{Gb\omega}{2\pi d\,(1-v)} [\left(1 + \left(\frac{d}{b}\right)^2\right) \ln\left(1 + \left(\frac{d}{b}\right)^2\right) - 2\left(\frac{d}{b}\right)^2 ln\left(\frac{d}{b}\right)] \qquad (2.11)$$

2.2.3.1 Grain Growth Retardation

A number of factors, for example solute drag and chemical drag, can be used to influence grain boundary mobility and hence grain growth [145]. Since the grain boundary migration rate, V, depends on the driving force, P, and intrinsic mobility, it is possible to reduce grain growth through reducing the driving force, decreases grain boundaries diffusion [146].

$$V = mP = \left(\frac{a^2}{kT}\right) D_{gb} P$$

$$= \left(\frac{a^2}{kT}\right) D_o \exp\left(\frac{Q}{RT}\right) P \qquad (2.12)$$

In equation 2.12, a is the lattice constant, D_{gb} is the grain boundary diffusion, k is the Boltzmann's constant and T is the absolute temperature. The presence of dopant at the grain boundaries, which will create a solute drag effect, is one of the ways to reduce grain growth through reducing driving force of the grain boundary mobility. This is one of the reasons for observing limited grain growth in several nanocrystalline solid alloy solution when the solute atom have segregated to the grain boundaries [124, 147].

Furthermore, the presence of dopant atoms at the grain boundaries will pin the free dislocation at the grain boundaries and reduce stress induced grain growth. Li et al [121], through theoretical calculation, indicated that metastable or high energy grain boundary structure and high purity material were the two main conditions required for stress induced grain growth. Figure 2.20 showed that the number of free dislocations in the homogenous grain boundaries reduces the shear stress required for their emission. In Figure 2.20, x is the distance of free dislocation from center of grain boundary and h is the spacing between dislocations. Hence, pinning the free dislocation using dopant will reduce stress induced grain growth.

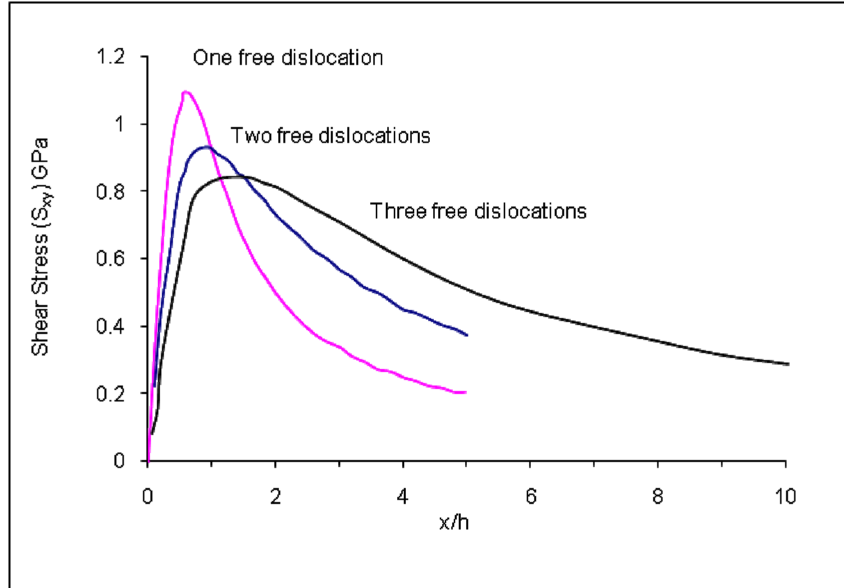

Figure 2.20: Decrease in shear stress required with increasing number of free dislocations at a tilt grain boundary. Thermal effects are not considered in this model

Nanocrystalline materials were more susceptible to grain growth as compared to their micro-crystalline counterparts due to the higher volume fraction of high energy grain boundary atoms. Hence, by introducing solute segregation at the grain boundaries [35], it may be possible to eliminate the thermodynamic driving force for grain growth by reducing the excess grain boundary energy to zero [34]

$$\gamma = \gamma_o - X_\beta \Delta H_{seg} \tag{2.13}$$

In equation 2.13, γ_o is the specific grain boundary energy of the sample; X_β is the dopant concentration at the interface. ΔH_{seg} is the enthalpy of segregation and this is the excess energy for introducing a foreign atom in the materials. Equation 2.13 showed that it was possible to

decrease the grain boundary energy γ by introducing a large ΔH_{seg}. By doing so, the total Gibbs free energy would be smaller than the Gibbs free energy of the single crystal solid solution and this will eliminate the driving force for grain growth. However, this is only true if the dopants segregate to the grain boundary and do not form precipitates. Although there is still no convincing experimental evidence to support this yet, some promising observations with doped samples of Pd_{1-x} Zr_x [147] and $Y_{1-x}Fe_x$ [124] have shown that by increasing x, grain growth was suppressed until higher temperatures. Furthermore, recent molecular dynamics simulations by Millett et al. [14, 148, 149] have shown that the driving force can be driven to zero with the presence of sufficient dopants atom content at the grain boundaries, and hence eliminating grain growth. Furthermore, Millett et al [14, 148, 149] have found that the concentration of dopants needed to prevent grain growth depends on the relative size of dopant atoms.

2.2.4 Electrical Properties

Due to the increased volume fraction of the grain boundaries in nanocrystalline materials, their electrical resistivity was found to be higher than that of their microcrystalline counterparts. This was due to increased grain boundary scattering activities. Figure 2.21 [28, 60] showed that at constant temperature, the electrical resistivity increased with a decrease in grain size whereas the electrical resistivity increases as the temperature increases at a given grain size. Since these observations are consistent with the theoretical analysis of grain boundary scattering of electrons [7], they provided strong experimental evidence for this reasoning. Lastly, Bakonyi et al [150] have shown that the electrical resistance is also a function of imperfection and residual stress introduced by synthesis process

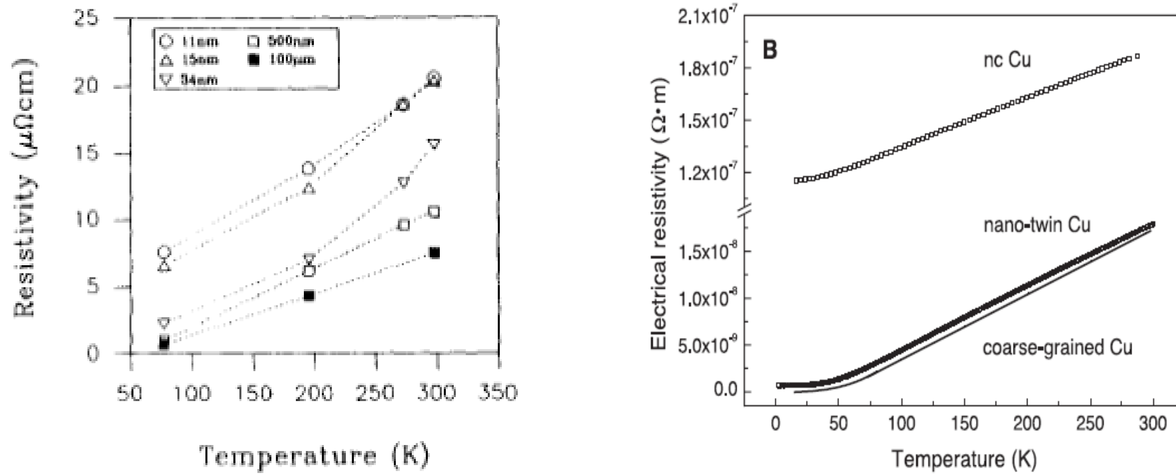

Figure 2.21: Comparisons of resistivity of nanocrystalline and micro-crystalline nickel and copper [28, 60]

2.3 Summary of Literature Survey

In summary, we have outlined the fabrication methods for chip to package interconnection. Nanostructure interconnects technology is the most promising interconnect technology to meet the high mechanical and electrical requirements of next generation devices. However, there is need for an alternate material with high strength material and superior electrical conductivity.

Furthermore, this chapter reviews the mechanical and electrical properties of nanocrystalline materials. Indeed, nanocrystalline materials have impressive mechanical properties which will enhance the reliability of the nanostructure chip to packages interconnects. They include a five to ten fold increases in strength and hardness as compared to their

microcrystalline state, relatively good ductility and enhanced fatigue endurance limit. Furthermore, the conductivity of nanocrystalline copper although lower than that of its microcrystalline counterpart, it was still much higher than the current interconnects materials that are alternative to copper.

However, more studies are still needed to fully understand the deformation and fracture and fatigue mechanisms for the nanocrystalline materials. Furthermore, the improvement in the fatigue properties is not well documented and no model has been established to predict/characterize these nano materials in interconnection application; conflicting results regarding the fatigue properties have also been reported. Hence, various studies on the fatigue properties of nanocrystalline materials are needed so as to assess the feasibility of using nanocrystalline materials as interconnects materials.   Lastly, there is also a need to fully understand and retard the grain growth phenomenon during deformation since grain growth during application may hinder the usefulness of nanocrystalline materials.

Chapter 3

Atomistic Simulation of Material Behavior

3.1 Introduction

Since nanocrystalline materials exhibit significantly superior properties as compared to their microcrystalline counterpart, the behavior of nanocrystalline materials has been the subject of extensive research in the recent past. In spite of that, as mentioned in Chapter 2, the deformation mechanisms in nanocrystalline materials are still not well understood. This is due to the difficulty in synthesizing high purity, defect free nanocrystalline material in large enough quantity to conduct mechanical characterization tests. Furthermore, studying the deformation mechanisms experimentally is difficult due to a variety of reasons. For example, accurate grain growth studies are difficult to conduct due to problems in accurately measuring the grain size; X-ray diffraction techniques tend to underestimate the grain size due to the presence of mechanical twins whereas the small thickness requirement for TEM tends to results in growing the grain size during testing. Hence, in conjunction with experimental studies, atomistic simulation, either classical or quantum mechanical, have been employed in the hope of gaining better insights into the atomistic processes and behavior of nanostructured materials. The two types of atomistic simulations used in this work are molecular dynamics and molecular statics. Molecular statics is a computational technique which utilizes numerical optimization techniques to minimize the potential energy of the system whereas molecular dynamics simulates the motion and interactions between a system of N atoms or molecules throughout time by solving a system of

equations based on the Newton's second law in an iterative manner. An overview of molecular statics, molecular dynamics, inter-atomic potentials, time integration algorithms, the isothermal-isobaric ensembles, the isothermal-isochoric ensembles and the modified isothermal-isobaric ensembles for constant strain rate, periodic boundary conditions neighbor lists as well as post processing technique will be presented in this chapter. A more comprehensive review of atomistic simulation can be found in Allen and Tildesley [151], Frenkel and Smit [152] and Haile [153].

3.2 Molecular Statics

Molecular statics is used in this research to compute the initial atomic configuration prior to deformation. It is important to describe this initial configuration accurately in order to draw relevant conclusions regarding the roles of the grain boundaries in the deformation process. This method consists of computing the minimum energy interface structures through minimization of the system's total potential energy at a 0K. Although there is no optimization method that will definitely determined the global minimum energy configuration, established methodologies such as Monte Carlo [154], Metropolis sampling [155], steepest decent and conjugate gradient methods [156] are known to work with some success. Monte Carlo [154] and Metropolis sampling [155] method rely on iterative random sampling within an acceptance criterion to search for the configuration with minimum energy where steepest decent and conjugate gradient method determine the specific configuration of atoms and follows the direction of the largest gradient on the potential energy function. In this project, nonlinear conjugate gradient is used to obtain the initial microstructural configuration. Furthermore, secant method and Polak Ribière formulation [157] was used to determine the step sizes and search direction, respectively. More

in-depth reviews of the conjugate gradient method can be found in Shewchuk [157] and Spearot et al [158].

Conjugate gradient method solves a sparse system of equations using an iterative method. Since the force on any atom is related to the interatomic potential through the gradient operator as shown in equation 3.1, the minimum potential energy can be found by setting these forces as the residual of the potential energy and solving equation 3.1.

$$F^i = \frac{\partial U(r_N)}{\partial r^i} \tag{3.1}$$

In equation 3.1, the parameter F^i is the force on a given atom, r_N is the atomic position vector for a system of N atoms and r^i is the atomic position vector for the ith atom respectively. The parameter U is the inter-atomic potential energy. The atomic position vectors is updated using an iterative process as described by equation 3.2

$$r_{m+1} = r_m + \alpha_m d_m \tag{3.2}$$

In equation 3.2, α_m is a proportional factor that minimizes the potential energy in the search direction whereas d_m is the search direction. Since the potential energy at r_{m+1} is orthogonal to the search direction, as shown in equation 3.4, a line search algorithm, such as Secant method as shown in equation 3.4, is used to approximate the second derivative of the potential energy to determine α_m

$$[U'(r_m + \alpha_m d_m)]^T d_m = 0 \tag{3.3}$$

$$\alpha_m = -\mu \frac{[U'(r_m)]^T d_m}{[U'(r_m + \mu d_m)]^T d_m - [U'(r_m)]^T d_m} \tag{3.4}$$

In equation 3.4, μ is the scalar number for the conjugate gradient method. Furthermore, the search direction in the conjugate gradient method is also determined using iterative processes as depicted in equation 3.5

$$d_{m+1} = g_{m+1} + \beta_{m+1} d_m \tag{3.5}$$

The residual g_{m+1} is computed by equation 3.6 whereas the constant β was determined using Polak Ribière formulation which forces the successive search direction to be conjugate.

$$g_{m+1} = -\frac{\partial U(r_m)}{\partial r_{m+1}} \tag{3.6}$$

$$\beta_{m+1} = max\left\{\frac{g_{m+1}^T(g_{m+1} - g_m)}{g_m^T g_m}, 0\right\} \tag{3.7}$$

3.3 Molecular dynamics

3.3.1 Governing Equation

Molecular dynamics (MD) is used in this research to simulate the deformation of nanocrystalline materials. In MD, the motion and interaction of atoms or molecules in the system is simulated by solving a system of equations based on Newton's second law [152].

$$F^i = ma^i \tag{3.8}$$

In equation 3.8, m is the atomic mass, a^i is the acceleration of the ith atom and F^i is the total resultant force on i^{th} atom and it is the sum of all the forces due to its surrounding neighboring atoms. In short, molecular dynamics uses equation 3.1, equation 3.8 and finite difference methods to discretize time into a specific time step Δt, so as to compute the subsequent time step evolution using position and velocity from the previous time step.

3.3.2 Time Integration Technique

One of the most commonly utilized time integration methods for molecular dynamics is the velocity Verlet algorithm. In addition to the avoidance of the computationally intensive iterative correction steps, this algorithm offers conservation of the total energy, Helmholtz free energy and Gibbs free energy during integration over a long period of simulation time for NVE, NVT and NPT ensemble, respectively. Hence, this technique offers much better simulation time stability and efficiency as compared to other integration techniques [159]. Since this research only utilizes the velocity Verlet algorithm with a time step of 1 fs, the readers are encouraged to read the reviews on other methods such as Verlet, leap frog algorithm elsewhere such as by Frenkel and Smit [152]. The approach in the velocity Verlet algorithm is to use the velocity for the present time step the computed velocity at half a time step forward as as described in equation 3.9 [160].

$$v^i\left(t + \frac{\Delta t}{2}\right) = v^i(t) + \frac{\Delta t}{2m} F^i(t) \tag{3.9}$$

In equation 3.9, v^i is the atom's velocity and m is the mass of the atoms. Furthermore, using equation 3.10 and the velocity computed from equation 3.9, the atomic position at the next time step is computed.

$$r^i(t + \Delta t) = r^i(t) + v^i(t + \frac{\Delta t}{2}) \tag{3.10}$$

After updating the forces with the newly computed atomic position, the velocity in the next time can then be found using equation 3.11

$$v^i(t + \Delta t) = v^i\left(t + \frac{\Delta t}{2}\right) + \frac{\Delta t}{2m} F^i(t + \Delta t) \tag{3.11}$$

3.3.3 Periodic Boundaries Condition

In order to mimic the behavior of bulk nanocrystalline materials, periodic boundary condition, which simulates an infinite system by replicating the simulation cell in all directions, is often employed in MD simulations. Figure 3.1 show a schematic of a periodic boundaries condition.

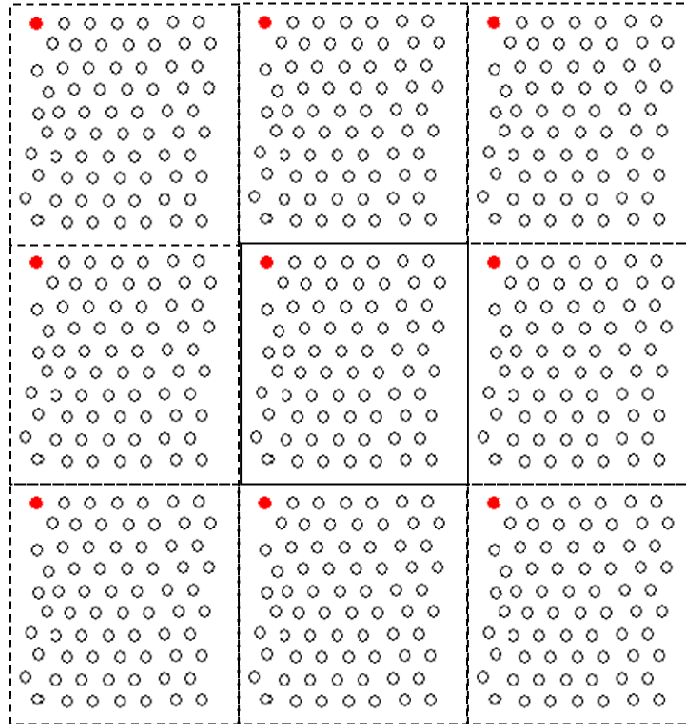

Figure 3.1: Schematic of a simulation cell with periodic boundary condition in 2d space. The cell with solid border is the primitive cell whereas the surrounding cells with dashed borders are the image cells

The original cell is known as the primitive cell whereas the image cells are the replications as shown in Figure 3.1. In a way, periodic boundary conditions work in the same configuration as some video games; in other words, the atoms reappear on the opposite side of the primitive cell with the same velocity after it has crossed the boundaries of the primitive cell. In this way, the atoms near the surface in the primitive cell interact with the atoms in the image cell thus avoiding the feeling of a free surface and hence reducing surface effects. This is especially important considering the fact that the number of atoms in the continuum sample is much larger than the model in the largest molecular dynamics simulation and hence causing the

molecular simulation model to have significantly higher number of atoms near the surface. It is also important to note that periodic boundary conditions will conserve the linear momentum of the system but not the angular momentum since the periodic boundary conditions do not rotate symmetrically.

Although periodic boundary conditions are useful for simulating bulk material behavior with no free surface, modified periodic boundary conditions known as the slab boundary condition, where the periodic boundary condition is removed in one of the directions, can be enforced to simulation a thin film or any instances where there is a need for a free surface.

3.3.4 Neighbor Lists:

At each time step in molecular simulation, computation of force on the atoms requires a calculation of a total of $\frac{N(N-1)}{2}$ pair-wise interactions for a system with N atoms and hence that is one of the most computationally expensive step. In order to speed up the computation of forces, the concept of cut off radius r_{cut} has been introduced. Since the contributions from long range interaction of atoms are negligible, all interaction of the atoms outside of r_{cut} are assumed to be negligible. Hence, by constructing the neighbor lists which stores all the atoms within r_{cut} and a buffer length r_{buffer} and only computing the interactions of these atoms for the calculation of the force on the ith atom, the computational time and effort can be significantly reduced. Furthermore, due to the motion of the atoms, it is important to update the neighbor list at every n^{th} time step. Hence, with the implementation of neighbor list, computation times will be significantly reduced, without any loss of accuracy, as the computation time now scales with an order of $N^{3/2}$ instead of N^2 initially.

However, even with this improvement, only extremely short time duration and very small specimens are possible in the molecular simulation due to the computation intensive nature of molecular dynamics. For example, using a 1.7 GHz Pentium processor, there is a need for 9.38×10^{-6}s of computation simulation time per atom per time-step for an EAM potential and a 4.5510^{-6} s simulation time per atom per time-step for Lennard Jones potential [161]. Bear in mind that the molecular dynamics models usually requires more than 100000 atoms to simulate a nano-crystalline microstructure.

3.3.5 Ensembles

The discussion in the previous section on molecular dynamics revolves only around Equation 3.1, which is actually the most basic form of molecular dynamics ensembles known as the microcanonical or NVE ensemble (which maintains constant number of atoms, volume and total energy throughout the simulation). This ensemble is also commonly known as equilibrium molecular dynamics since it simulates the material behavior in an isolated system. However, the vast majorities of the mechanics and materials systems are not in isolation and will interact with their environment. Hence, a special class of molecular dynamics that corresponds to statistical mechanics' canonical ensemble is needed. This class of molecular dynamics is known as non-equilibrium molecular dynamics and it uses use additional differential equations to accurately model the interaction between the systems and its environment.

3.3.4.1 Isothermal-Isochoric ensemble (NVT)

Instead of an isolation system as in the NVE ensemble, the NVT ensemble allows the system to interact with the environment. In NVT ensemble, the temperature of the system is allowed to fluctuate about the desired temperature while maintain the simulation cell's size and the number of atoms in the simulation cell. Hence, NVT ensemble will represent closely the displacement control in the normal experimental set up.

One of the methods used to control its temperature during simulation is through the ah-hoc velocity scaling as shown in equation 3.12 [152].

$$v_{m+1}^{i} = v_{m}^{i}\sqrt{\frac{T_D}{T_m}} \tag{3.12}$$

In equation 3.12, v_m^i is the velocity of the ith atoms at the mth time step, T_D is the desired temperature and T_m is the temperature of the system at the mth time step. This is, however, a crude method of controlling temperature as it will only reproduce the canonical distribution for the specific constraint.

A more appropriate way of controlling temperature will be the extension system method where frictional/damping coefficient ζ is incorporated into the equation of motion to couple the system's dynamics to the desire temperature. Hoover et al [162] were able to formulate the equation of motion for a NVT ensemble as given in equation 3.12 to equation 3.15

$$\dot{r}^{i} = v^{i} \tag{3.12}$$

$$\dot{v}^{i} = \frac{F^{i}}{m^{i}} - \xi v^{i} \tag{3.13}$$

$$\xi = \frac{\dot{s}}{s} = \frac{d(\ln s)}{dt} \tag{3.14}$$

$$\dot{\xi} = \frac{\left[\sum m^i (v^i)^2 - g k_B T_D\right]}{Q} \tag{3.15}$$

In equation 3.12 to equation 3.15, r^i is the position of the ith atoms, k_B is the Boltzmann's constant, T_D is the desired temperature and *s* the scaling factor. The parameter *Q* in equation 3.15 is the mass of the thermostat and it will act as a damping factor. The lower the value of Q, the higher is the temperature fluctuation about the mean desired temperature. A value of 20 is used in the present calculations.

3.3.5.2 Isothermal-Isobaric ensemble (NPT)

The main difference between the NVT and the NPT ensemble is that the NPT ensemble allows the simulation cell's to change its cell size in response to its surrounding pressure and hence simulating the load control scenarios in the conventional experimental set-up. Hence, using the same rationale for changing the simulation cell size according to the imbalance between the internal and desired pressure, a number of extended system methodologies for NPT ensemble such as by Parrinello et al [163], by Nosé et al [164] and by Hoover et al [162] have been developed: Parrinello et al [163] methodology for the extension to incorporate anisotropic response through the change in the simulation cell size and shape whereas Hoover et al [162] methodology for its ease of implementing them into molecular dynamics code.

As mentioned in the previous section, the equation of motion for NPT formulation by Hoover et al [162] is one of the more popular methodologies due to the ease of implementing them into the molecular dynamics codes. However, Melchionna et al [165], noting that Hoover et al equation of motion for NPT ensemble does not model the NPT ensemble precisely due to the volumetric scaling of the atom positions, modified the original Hoover's NPT ensemble to obtain the correct NPT equation of motion. Their equations of motion for NPT ensemble are shown in equations 3.16 to 3.20 [165]

$$\dot{r}^i = v^i + \eta(r^i - R_0) \tag{3.16}$$

$$\dot{v}^i = \frac{F^i}{m^i} - (\eta + \xi I)v^i \tag{3.17}$$

$$\dot{\xi} = \frac{\left[\sum m^i (v^i)^2 - g k_B T_D\right]}{Q} \tag{3.18}$$

$$\dot{\eta} = \frac{v_p^2}{N k_B T_D} V(\sigma - P_D) \tag{3.19}$$

$$\dot{h} = \eta h \tag{3.20}$$

In equation 3.16-3.20, η is the isobaric friction coefficient, P_D is the desire pressure, v_p is the constant pressure damping coefficient and h is a set of vectors that define the boundaries of the simulation cell.

3.3.5.3 Modified Isothermal-Isobaric Ensemble for Constant Strain Rate

One of the main disadvantages of NPT ensemble is that the external pressure must be inputand hence strain rate is not controlled. Since the equation of the motion adjusts the simulation cell size based on the imbalance between the internal and desired pressure, it is not possible for the strain rate for to remain constant. Furthermore, Yamakov et al [166]had showed that the type of deformation mechanism depends greatly on the direction of the external pressure and there is a need to modify the NPT ensemble to allow constant applied strain rate.

Hence, Spearot et al [167] modified the Melchionna et al [165] equation of motion to allow the prescription of the rate of the change of the simulation cell size. i.e a constant applied strain rate. In order to maintain a constant strain rate, he incorporated an additional damping term $\gamma\eta$ into equation 3.19 while maintaining the other equations in Melchionna's [165] equation of motion in NPT ensemble. His equations of motions are as described:

$$\dot{r}^i = v^i + \eta(r^i - R_0) \tag{3.21}$$

$$\dot{v}^i = \frac{F^i}{m^i} - (\eta + \xi I)v^i \tag{3.22}$$

$$\dot{\xi} = \frac{\left[\sum m^i (v^i)^2 - g k_B T_D\right]}{Q} \tag{3.23}$$

$$\dot{\eta} = \frac{v_D^2}{N k_B T_D} V(\sigma - P_D) - \gamma\eta \tag{3.24}$$

$$\dot{h} = \eta h \tag{3.25}$$

In equation 3.23, the additional term $\gamma\eta$ is the additional damping term needed to maintain the smooth motion of the simulation cell size. By prescribing the rate of change of $\dot{h}$ in equation 3.25

in the uniaxial loading direction and allowing the two other sides of the simulation cell to move according with the equation of motion for NPT ensemble, the applied strain rate in the loading direction can be enforced.

3.3.6 Computing Physical Quantities

In order to quantify the deformation of the nanocrystalline materials throughout the molecular simulation, computational techniques need to be developed to measure and track some of the important physical quantities. One of these physical quantities is the total energy of the system which is the sum of both the potential energy and the kinetic energy of the system. The potential energy is the sum of the contribution of all the pairwise interaction $\phi(r^{ij})$ as shown in equation 3.26 whereas the kinetic energy term in the time average of the instantaneous kinetic energies K(t)

$$U(t) = \Sigma \quad \Sigma \quad \phi(r^{ij}) \tag{3.26}$$

In equation 3.22, r^{ij} is the distance between the ith atom and j^{th} atom. i.e

$$r^{ij} = r^{i} - r^{j}. \tag{3.27}$$

The instantaneous kinetic energies K(t) can be computed as follows:

$$K(t) = \frac{1}{2} \Sigma_i m^i [v^i \ v^i] = \frac{\delta}{2} N k_B T \tag{3.28}$$

In equation 3.28, v_x^i, v_y^i, and v_z^i is the ith atom's velocity in the x , y and z direction respectively.

The most common method to compute internal pressure P and stress $\sigma_{\alpha\beta}$ is by the virial theorem as shown in equation 3.29 and 3.30 [151]

$$P = \frac{1}{3V}\left[\sum \sum U' r^{ij} + \sum m^i v^i v^i\right] \quad (3.29)$$

In equation 3.29, *U'* is the first derivative of the potential energy.

$$\sigma_{\alpha\beta} = \frac{1}{V}\left[\frac{1}{2}\sum \sum \frac{U'}{r^{ij}} r_\alpha^{ij} r_\beta^{ij} - \sum m^i v^i v^i\right] \quad (3.30)$$

In equation 3.30, $\sigma_{\alpha\beta}$ is the stress tensor and the subscript α and β denotes α and β components. Although equation 3.30 has been used commonly to compute the mechanical stress, Zhou et al [168] had shown that this virial stress formulation not only cannot account for rigid body motion, the kinetic energy calculation had also violated the conservation of momentum. Hence, virial stress is not exactly equivalent to the mechanical stress. Zhou et al [168] observed that the force term had already accounted for the kinetic energy contribution and he pointed out the system stress should be calculated without the contribution from the kinetic energy term, as shown in equation 3.31, so as to ensure the equivalency of the virial stress and the mechanical stress.

$$\sigma_{\alpha\beta} = \frac{1}{V}\left[\sum \sum F_\alpha^{ij} r_\beta^{ij}\right] \quad (3.31)$$

In equation 3.31, F_{α}^{ij} is the force between i^{th} and j^{th} atoms. However, the magnitude of the kinetic energy terms for solid materials is very small as compared to the contribution for the inter-atomic forces and since the computation of stress in this research requires the stress to be average over a relatively large volume, the fluctuation of the virial stress will be further reduced [169]. Hence, this research opts to keep the kinetic contribution in the calculation of mechanical stresses.

3.3.7 Inter-Atomic Potentials

Choosing the right inter-atomic potential function that can accurately describe the nature of the atomic bond is the one of the most important if not the most important decision in molecular simulations. Even though a wide variety of the potentials that have been developed to model the physics of different types of materials, these inter-atomic potentials can be basically divided into four major classes or combinations of these four major classes. They are the pair potentials, cluster potential, pair functional potentials and the cluster functional potentials [170]. Pair potentials are a function of only the separation distance between two atoms whereas the cluster potential depends on both the distance and the angles between the two atoms. Since the Lennard-Jones potential, which is a type of pair potential, and the embedded atom method potential, which a combination of pair potential and pair functional potential are used in this reserach, only these two potential types will be discussed in detail. More detailed information on other classes of potentials can be found in Carlsson et al [170].

3.3.7.1 Lennard-Jones Potential

Although pair potential cannot reproduce the properties of the transition metals accurately due to its inability to account for the intra-molecular forces, it can be easily implemented into molecular dynamics code due to its same simplistic nature. Hence, it has been successfully employed to model metallic glasses and inert gas behavior [171, 172] and to investigate fundamental issues such as grain growth phenomenon in nanocrystalline metals. One of the most common pair potential is the Lennard-Jones potential as shown in the following expression [173]:-

$$U(r^{ij}) = 4\varepsilon[(\frac{\sigma}{r^{ij}})^{12} - (\frac{\sigma}{r^{ij}})^{6}] \tag{3.32}$$

In equation 3.32, σ is the atomic spacing at zero potential energy and ε is the energy at equilibrium spacing. Since the r^{-12} term accounts for the repulsive forces whereas the r^{-6} term accounts for attractive forces, Lennard-Jones potential is attractive at large distance of r^{ij} but reaches a minimum and becomes strongly repulsive. Furthermore, equilibrium spacing, $r^{ij}{}_{eq}$, between two atoms, where the potential energy is at the minimum, can be computed easily as follows

$$r^{ij}{}_{eq} = 2^{1/6}\sigma \tag{3.33}$$

Using copper as an example, Figure 3.2 shows the profile of the Lennard-Jones potential and its force derivative and Table 3.1 provides a compilation of these parameters for found in the literature.

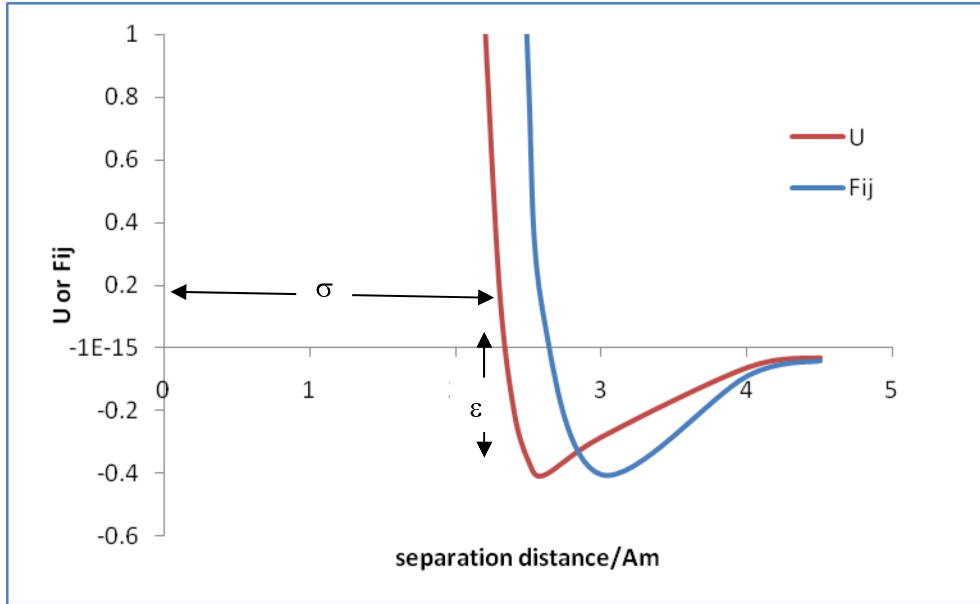

Figure 3.2: The Lennard-Jones potential and its force derivative of copper

Table 3.1: Lennard-Jones Parameters compiled from the literature [174]

Element	σ(A)	ε(j)
Aluminum	2.62	6.281E-20
Gold	2.637	7.066E-20
Lead	3.197	3.781E-20
Nickel	2.282	8.331E-20
Palladium	2.52	6.841E-20
Silver	2.644	5.528E-20

Copper	2.338	6.553E-20
Iron	2.321	8.427E-20
Tungsten	2.562	1.711E-19

According to equation 3.1, calculation of force requires taking the derivative of inter-atomic potential with respect to r^{ij}. Since the derivative of equation 3.32 produced a closed form solution as shown in equation 3.34, the force calculation using Lennard-Jones is computationally inexpensive.

$$F^{i} = \frac{24\varepsilon}{r^{ij}}\left[2\left(\frac{\sigma}{r^{ij}}\right)^{12} - \left(\frac{\sigma}{r^{ij}}\right)^{6}\right] \tag{3.34}$$

Further reduction in the computational time and effort can be achieved through reduced or non-dimensional units when modeled with Lennard-Jones potentials. Using σ and ε as the normalizing parameters and assuming unit mass, the following dimensionless parameters can be used:-

Table 3.2: Reduce Lennard Jones units [174]

Properties	Dimensionless LJ unit
Length	σ
Energy	ε
Time	$\sigma\sqrt{\frac{m}{\varepsilon}}$

Force	$\frac{\varepsilon}{\sigma}$
Pressure	$\frac{\varepsilon}{\sigma^3}$
Temperature	$\frac{\varepsilon}{k_B}$

An inspection of Table 3.1 shows the lack of Lennard-Jone parameters for antimony. Since one of the main objectives of this research is to develop an understanding of the enhancement in grain stability due to the addition of antimony in nanocrystalline copper during fatigue loading, these parameters are needed for antimony. Even though Chang et al [175] had developed a Johnson's pair potential for antimony, the heat of mixing for copper antimony interaction was found to be off by a few orders. Hence, a new antimony potential based upon the Lennard-Jones potential formulation has been developed in our group. Through the calculation of the heat of mixing and the strain field generated by a single antimony impurity in single crystal copper, as shown in Figure 3.3, Rajgarhia et al [176] were able to develop this antimony inter-atomic potential which provides a better correlation with the magnitude of the strain field around the antimony atoms. Hence, their values for antimony of σ=3.15Åm and ε=0.079 eV will be used through this research to model antimony response.

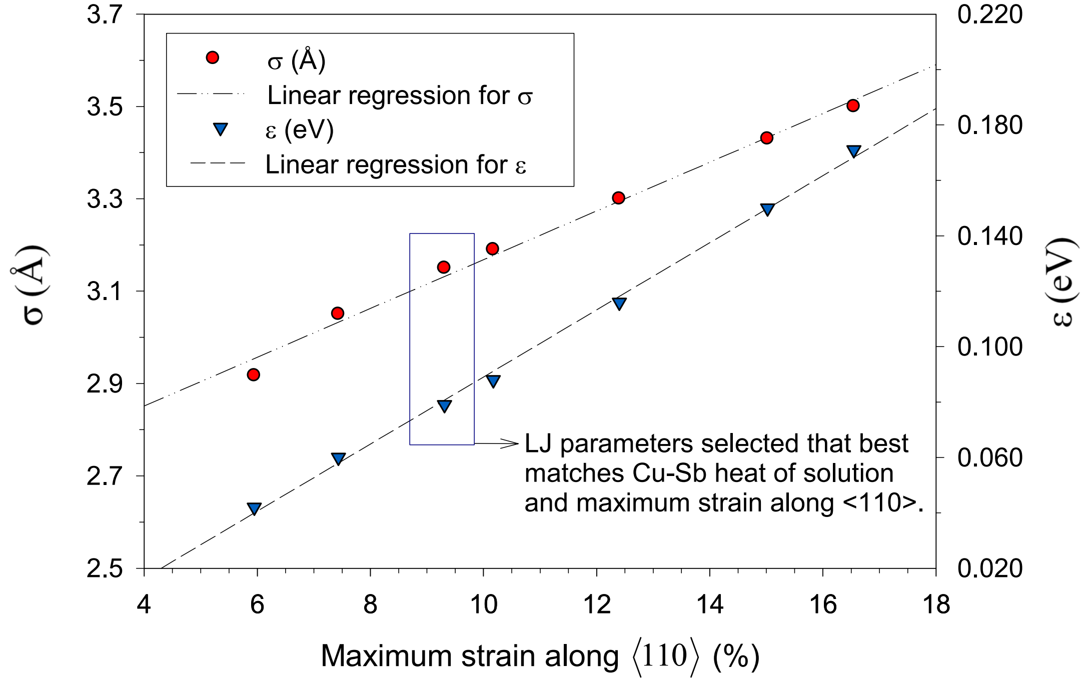

Figure 3.3: Correlation between Lennard-Jones parameters for antimony [176]

In order to model the deformation of the antimony doped copper, the interactions between the two types of materials must also be considered. However, the Lennard-Jones parameters listed in Table 3.2 and Figure 3.3 are all formulated for single component systems and it is necessary to know parameters for the interspecies interactions ($\sigma_{\alpha\beta}$ and $\varepsilon_{\alpha\beta}$) as well as Lennard's Jones parameter for each material. Hence, the interspecies interactions need to be estimated[177] using Lorentz-Berthelot combination rules, as shown in equation 3.35 and 3.36, and the parameters from Table 3.2 and Figure 3.3

$$\sigma_{\alpha\beta} = \frac{\sigma_{\alpha\alpha} + \sigma_{\beta\beta}}{2} \tag{3.35}$$

$$\varepsilon_{\alpha\beta} = \sqrt{\varepsilon_{\alpha\alpha}\varepsilon_{\beta\beta}} \qquad (3.36)$$

Here, $\sigma_{\alpha\beta}$ and $\varepsilon_{\alpha\beta}$ are the Lennard-Jones parameters for interspecies interaction whereas $\sigma_{\alpha\alpha}, \sigma_{\beta\beta}, \varepsilon_{\alpha\alpha}$ and $\varepsilon_{\beta\beta}$ denotes the parameters for atom type α and β.

3.3.7.2 Embedded Atom Method (EAM)

One of the main limitations of Lennard- Jones potentials is its inability to model transition metals accurately. Hence, Daw et al [178] developed the EAM potential from the density functional theory in the quasi-atom [179] and effective-medium theory [180] in order to accurately model the metallic bonding in FCC metals. The EAM potential computes the potential energy of a system as the sum of energy of the pair interaction in the systems as well as the energy required to embed an atom into a lattice site under the influence of the average electron density. Hence, the total energy for EAM formulation is given by equation 3.37

$$U(r^{ij}) = \frac{1}{2}\Sigma \ (\phi(r^{ij}) + F(p^{i})) \qquad (3.37)$$

In equation 3.37, $\phi(r^{ij})$ is the pair potential representing the cation-cation repulsion in the lattice whereas $F(p^{i})$ is the embedding energy required when i^{th} atom is placed in a lattice site with an a average background electron density, p^{i}. The background electron density is then the sum of all the electron density from its neighboring atoms as shown in equation 3.38

$$\rho^i = \sum \ \rho(r^{ij}) \tag{3.38}$$

In equation 3.38, the function $\rho(r^{ij})$ is a measure of the decay of the electron density and only the atom within the cut off distance is considered in the computation of average background electron density in this summation. Taking the derivation of equation 3.37 to determine the force of ith atom gives the following expression,

$$F^i = -\sum \ (\phi(r^{ij}) + [F'(\rho^i) + F'(\rho^j)]\rho(r^{ij})) \tag{3.39}$$

As shown in equation 3.39, the calculation of EAM forces is computational more intensive as compared to the calculation of Lennard-Jones forces and it requires two stages of computation. The first is to calculate the embedding functions by summing all the $\rho(r^{ij})$ term and the second is to compute the remaining term in equation 3.39.

By fitting several key parameters empirically (such as lattice constant, elastic constant, heat of solution etc) , Foiles et al [181] show that EAM potential can model several properties of pure metals such as lattice constant, formation volume and migration energy of vacancies and self-interstitials, surface energy and energy of segregation of substitutional impurities, accurately. Hence, the EAM potential by Foiles et al [181] is used to model the nanocrystalline copper throughout this research.

However, EAM potentials cannot be used for some metals, where directional bonding is important such as BCC crystal structure, HCP crystal structure and even certain FCC metals. This is due to the assumption of the spherically distributed background electron density during

its derivation. This restricts the use of EAM potentials to only certain FCC crystal structures in which the bond orientation is not important. In order to overcome this limitation, Baskes et al [182], using the same EAM formulation, had developed the modified embedded atoms method (MEAM) to account for the bond directionality and thus they could reproduce several accurate results in BCC crystal structure and non-metallic systems.

Even though EAM potential formulation requires a regression step with experimental data to give the correct physical properties, it is still critical to show that the inter-atomic potentials used in this work are appropriate and they can accurately model the deformation of FCC metals. Recent simulations have stressed the important of the chosen inter-atomic potential's ability to reproduce the entire stacking fault energy curve accurately [183]. As shown in Figure 3.4, the unstable stacking fault γ_{usf} is the magnitude of the peak of the generalized stacking fault curve where the stacking fault energy is the magnitude of the energy at its first minimum when shearing occurs between two {111} planes in the <112> direction. The stable stacking fault energy is important for molecular simulation as it will determine the dislocation disassociation width in FCC metals [184] whereas the unstable stacking fault energy will determine the characteristic of the dislocation nucleated [185]. Furthermore, recent simulation work by Van Swygenhoven et al [116] further stressed the importance of both the unstable stacking fault energy and the stable stacking fault energy in modeling grain boundary structure and dislocation nucleation. As mention in Chapter 2, they proposed that the transition from the emission of partial dislocation to the emission of full dislocation depended on the ratio of the stacking fault energy to that of the unstable stacking fault energy.

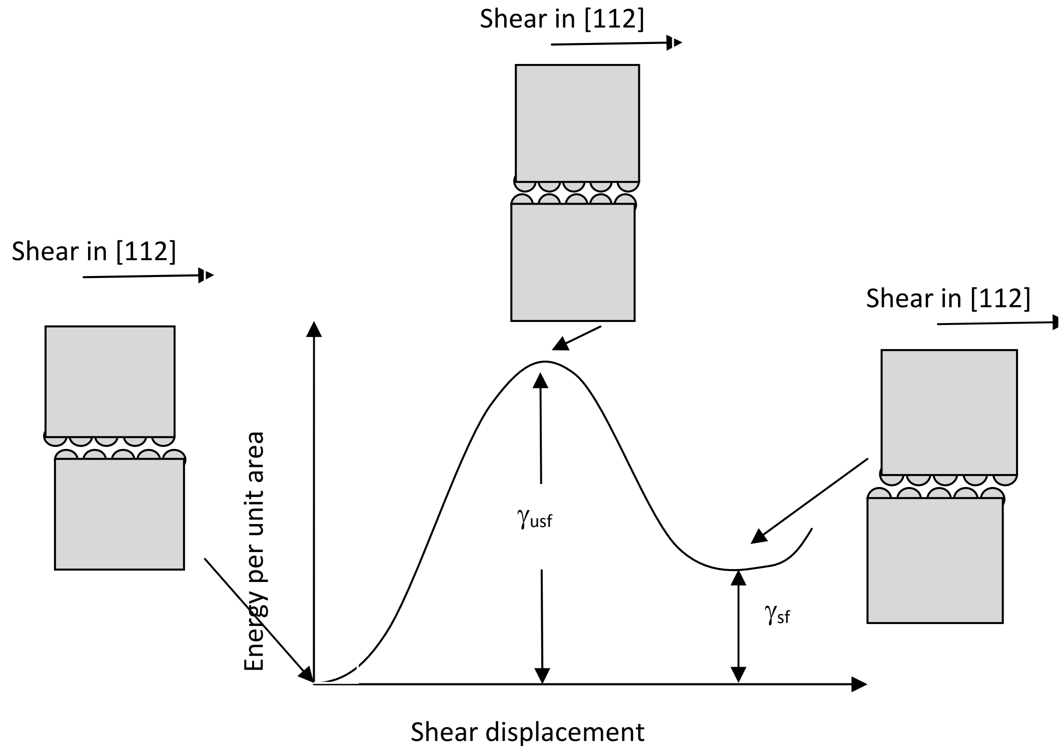

Figure 3.4: Schematic of the generalized stacking fault energy

3.3.8 Visualization of Atoms

Since the simulation cell usually consists of thousands and millions of atoms, molecular dynamics will generally generate huge amount of data. Hence, visualization technique is often needed during post post-processing to derive meaning in these data in order to have a better understanding of the dislocation activity during deformation processes. These visualization techniques include the centro-symmetry [186], energy, common neighbor analysis [187], slip vectors [188] or coordination numbers[189]. Examples of some of the visualization tools are illustrated in Figure 3.5. In this research, common neighbor analysis is used to visualize microstructure and dislocation activities for the single crystal analysis. However, due to the

computational intensive nature of the common neighbor analysis and the large number of atoms in the nanocrystalline models, centro-symmetry and energy are used instead to visualize microstructure and dislocation activity in nanocrystalline materials.

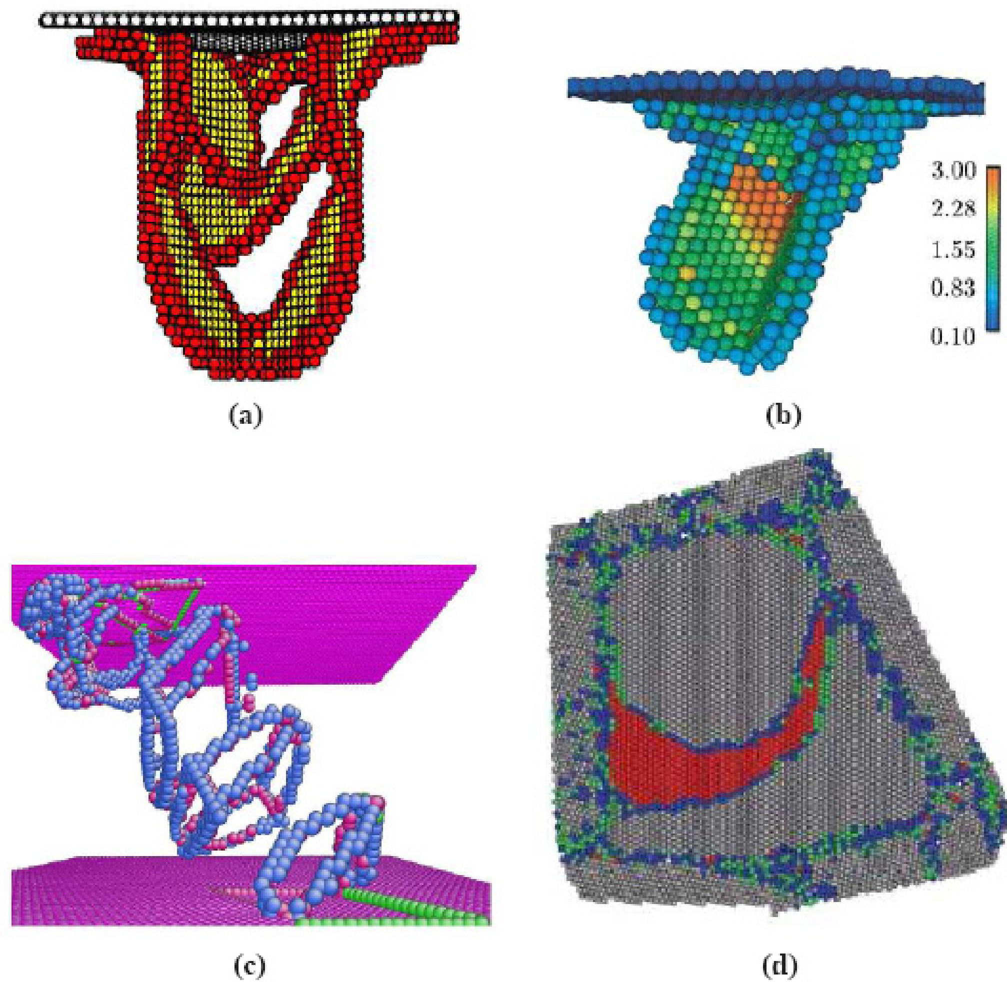

Figure 3.5: Visualization technique in molecular simulation: (a) Centro-symmetry parameters[186] (b) slip vector parameter [188] (c) coordination number [189] and common neighbor analysis[45] (reproduced from [190]

Since each atom has their own set of nearest neighbors, common neighbor analysis characterizes the type of bonding the atom had with their nearest neighbor by specifying three indexes *i*, *j* and *k* after analyzing their common share neighbors: index *i* accounts the total number of common neighbors, index *j* accounts for the total number of bonds between atoms in the common neighbor and index *k* accounts the number of bonds in the longest continuous chain between the common neighbor. For example, the common neighbor analysis index of FCC crystal structure is 421 since it has four common neighbors, two disjointed bonds among those common neighbors and the largest chain of bond is one.

Although common neighbor analysis gives more insight to the bonding between atoms, centro-symmetry and energy are used instead throughout this project for the visualization of deformation in nanocrystalline copper due to the computational intensive nature of the common neighbor analysis and the large number of atoms needed in the nanocrystalline models. The centro-symmetry parameter, which is defined as follows, characterizes the symmetric inversion of the neighbor atoms.

$$P^i = \sum \left| r^i + r^{j+6} \right|^2 \tag{3.39}$$

In equation 3.39, r^i and r^{j+6} are the displacement vectors corresponding to the six pairs of opposite neighbors nearest in the FCC lattice. The centro-symmetry parameter uses the fact that each atom in FCC crystal structure maintains an equal and opposite bonds to its surrounding neighbors even during deformation. Hence, the magnitude of centro-symmetry parameters for any atom in the regular FCC configuration will remain zero or a very low value whereas the

parameters for free surface, grain boundaries, dislocation and other lattice defects will induce a positive value.

3.4 Nanostructures

3.4.1 Nanocrystalline Structure

As mention in Chapter 2, a nanocrystalline structure produced by a severe deformation process such as ECAE usually consists of multiple randomly distributed and oriented grains bound by a network of grain boundaries. The most common technique to construct this type of nanocrystalline structure for molecular dynamics simulation is the Voronoi Tessellation method[191]. In this technique, the simulation cell is subdivided into arbitrary numbers of nearly uniform sub-volumes or Voronoi regions. Given a set of N grain center and orientation, which is determined by the grain size, each Voronoi region is defined as all points that is closer to its grain center than any particular grain centers [10]. Figure 3.6 shows a schematic of Voronoi decomposition and the nanocrystalline copper constructed using Voronoi Tessellation methodology.

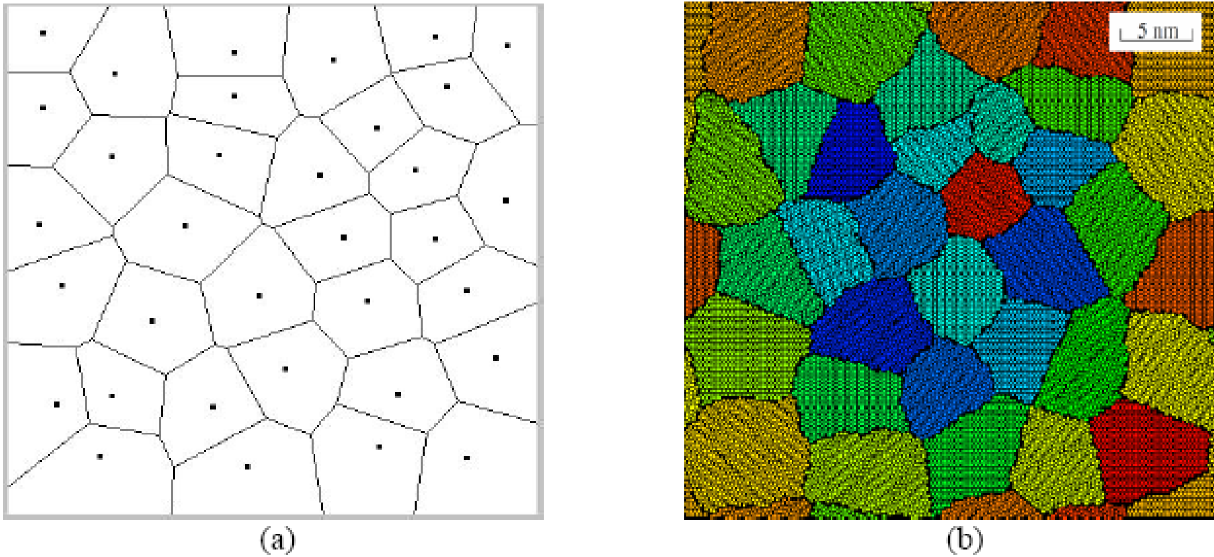

Figure 3.6: Schematic of Voronoi decomposition and the resulting nanocrystalline copper constructed using Voronoi Tessellation methodology [174]

In Figure 3.4a, each dot represents a grain center, which is almost randomly distributed in the simulation cell. It is not exactly random because one of the grain centers will be removed and re-generated again randomly if two centers are found to be too close to each other. This step is to generate a realistic nanocrystalline structure. Then a FCC lattice with the correct orientations is placed in each grain centers within the simulation cell and a check is performed under periodic boundaries conditions in which the atoms will be discarded if it is closer to other grain center. Molecular statics is the performed to relax all locally high potential configurations. Lastly, 20 to 200ps of NPT ensemble is performed to locally equilibrate the microstructure to obtained a stress free nanocrystalline materials.

CHAPTER 4
CRACK GROWTH ANALYSIS

In this chapter, numerical analysis using the stress intensity parameter ,K, and the J-integral, in conjunction with known experimental fatigue crack growth data has been employed to study the semi-elliptical crack growth and shape evolution in nanostructured interconnects subject to uniaxial fatigue loading. Closed form solutions for the computation of J integral developed in this research will also be discussed. 3D-nonlinear finite element analysis has been used to verify the Newman and Raju solutions for the computation of the elastic portion of J-integral. Molecular dynamics in conjunction to phase mixture model has been employed to determine the elastic modulus of nanocrystalline copper needed to conduct the crack growth analysis. This method establishes (a) the validity of the fracture mechanics approach in estimating the crack growth life of interconnects and (b) the relative contribution of the crack growth life to the overall fatigue life of nanostructured copper interconnects.

4.1 Proposed Methodology for Crack Growth Analysis

Finite element analysis is one of the most common methods used to computing stress intensity factors ΔK. However, implementing it to study crack evolution during fatigue cycle is a very time consuming process since a new model and analysis is needed for each fatigue cycle which could run up to thousands of cycles before failure. Hence, in order to avoid the vast number of finite element experiments needed to simulate the observed crack growth and shape

evolution in experiments; close form solutions for stress intensity factor have been developed in this research.

Due to the large strain experienced by the copper interconnects, the remaining ligament around the semi-elliptical cracks undergoes elastic plastic deformation for microcrystalline copper interconnects and may be the same for nanostructured interconnects. Hence, in this chapter we develop the capability to estimate crack growth fatigue life in small interconnects. Under the circumstances, it is more appropriate to use J integral, as shown in equation 4.1 instead of limiting oneself to the stress intensity factor ΔK.

$$J = \frac{K_{eqv}^2}{E} = J_e + J_p \tag{4.1}$$

In equation 4.1, the parameter K_{eqv} is the equivalent stress intensive factor corrected for plastic deformation in the ligament around the cracked section. The parameter, J_e is the elastic potion of J-integral whereas J_p is the plastic potion of J-integral. The elastic portion J_e can be calculated using equation 4.2 [192]

$$J_e = 4\varepsilon_0 \sigma_o \mathrm{a} \left(\frac{\mathrm{P}}{\mathrm{P_0}}\right)^2 \mathrm{F_e} \tag{4.2}$$

In equation 4.2, σ_o and ε_o is the yield stress and yield strain respectively. F_e is the linear elastic geometry correction, a is the crack depth whereas P and P_0 are the applied load and limit load respectively.

Furthermore, the elastic portion J_e can also be estimated using Newman and Raju's geometric function [193]. In fact, this function is one of the most frequently used closed form solution to calculate linear elastic stress intensity factors of semi-elliptical surface cracks Their formula, as shown in equation 4.3, is appropriate for tensile and bending components but only tensile component will be considered in this research. Figure 4.1 is a schematic of the parameters for the semi-elliptical cracks.

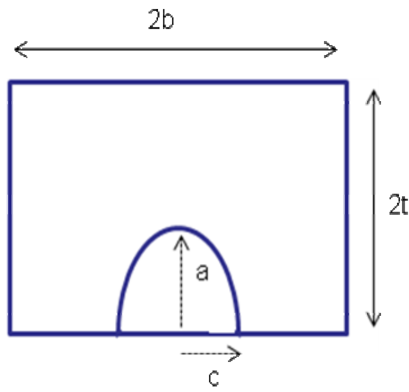

Figure 4.1: Parameters for the semi elliptical cracks

$$K_e = \sqrt{J_e E} = E\varepsilon\sqrt{\frac{\pi a}{Q}}F_e \tag{4.3}$$

In equation 4.3, K is the stress intensity factor, σ is the remote applied stress, ε is the applied strain, E is the modulus, Q is the shape factor given by equation 4.4 and F is as given by equation 4.5, is the parameter that accounts for the effect of the depth, width and aspect ratio.

$$Q = 1 + 1.464\left(\frac{a}{c}\right)^{1.65} \qquad for\ \frac{a}{c} \leq 1 \tag{4.4}$$

$$F = \left[M_1 + M_2\left(\frac{a}{t}\right)^2 + M_3\left(\frac{a}{t}\right)^2\right] f_\phi g f_w \tag{4.5}$$

In equation 4.2, M_1, M_2, M_3 and g are the fitting constant and they are described by equation 4.6 to equation 4.9 respectively. The angular function f_ϕ and finite width correction f_w in equation 4.5 can be described by equation 4.10 and 4.11 respectively.

$$M_1 = 1.13 - 0.09\left(\frac{a}{c}\right) \tag{4.6}$$

$$M_2 = -0.54 + \frac{0.89}{0.2+\left(\frac{a}{c}\right)} \tag{4.7}$$

$$M_3 = 0.5 - \frac{1.0}{0.65+\left(\frac{a}{c}\right)} + 14\left(1.0 - \frac{a}{c}\right)^{24} \tag{4.8}$$

$$g = 1 + \left[0.1 + 0.35\left(\frac{a}{t}\right)^2\right]\left(1 - sin\phi\right)^2 \tag{4.9}$$

$$f_\phi = \left[\left(\frac{a}{c}\right)^2 cos^2\phi + sin^2\phi\right]^{0.25} \tag{4.10}$$

$$f_w = \left[\sec\left(\frac{\pi c}{2b}\sqrt{\frac{a}{t}}\right)\right]^{0.5} \tag{4.10}$$

Since Equation 4.2 and 4.3 are equivalent, combining both equations will produce the following relationship for computation for F_e.

$$F_e = \frac{4F^2}{\pi Q} \tag{4.11}$$

Similarly, the plastic component, J_p, can be computed using the reference stress approach [194],

$$J_p = \Delta\varepsilon_p \Delta\sigma a \left(\frac{\pi D^2}{4A_{lig}}\right)^{m+1} \frac{\sigma_0}{\alpha' E} F_1 F_e \tag{4.12}$$

In equation 4.12, $\Delta\varepsilon_p$ is the plastic strain rate, *a* is the crack size, *D* is the diameter of the rod, *E* is the elastic modulus and α' and *m* is the hardening parameters. F_1 is the geometric correction factors which can be describe by Figure 4.2 [193]

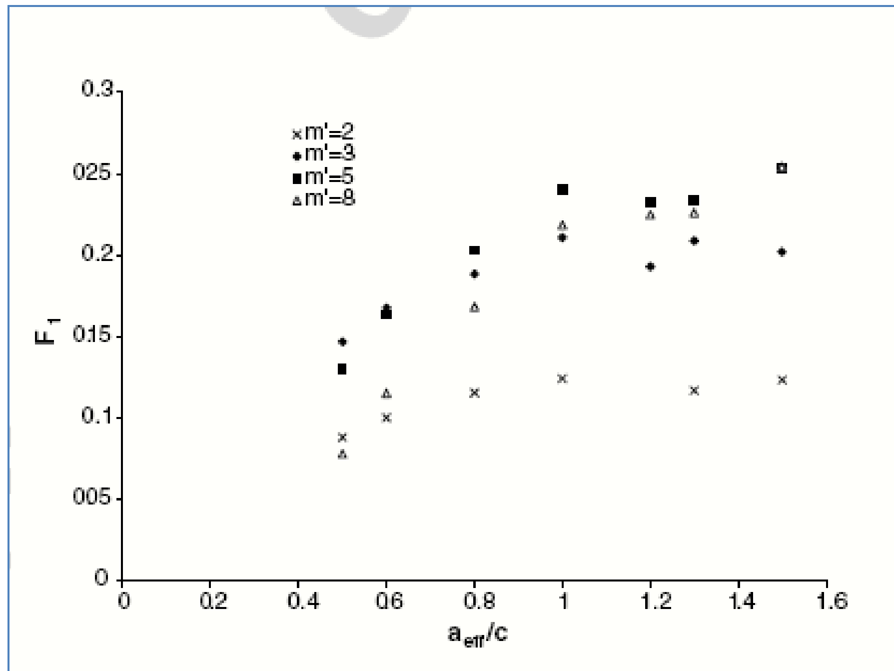

Figure 4.2: Plot of the correction factor, F1, versus a/c [193]

Hence, by using equation 4.1 to equation 4.12 in addition to the known crack growth data, the crack evolution analysis can be performed using the following methodology.

1. The grain size dependent material properties for the particular grain size are computed using molecular dynamics
2. The equivalent stress intensity factor K_{eqv} is computed using equation 4.1 to 4.12
3. The crack sizes and shapes at the end of each cycle is computed using the experimental result from Bansal et al[8],
4. Step 2 and step 3 are repeated until the crack growth becomes unstable.

4.2 Model Verification

As shown in Figure 4.1, Newman and Raju solution [193] was formulated for an elliptical crack inside a rectangular plate, whereas copper interconnect is in the form of a cylindrical bar as shown in Figure 4.3. There is a need for finite element analysis validation on the applicability of this equation for our analysis. Furthermore, Nickel Based super-alloy RENE88, instead of copper, is used in this verification since fatigue striations mark can be easily observed in RENE88.

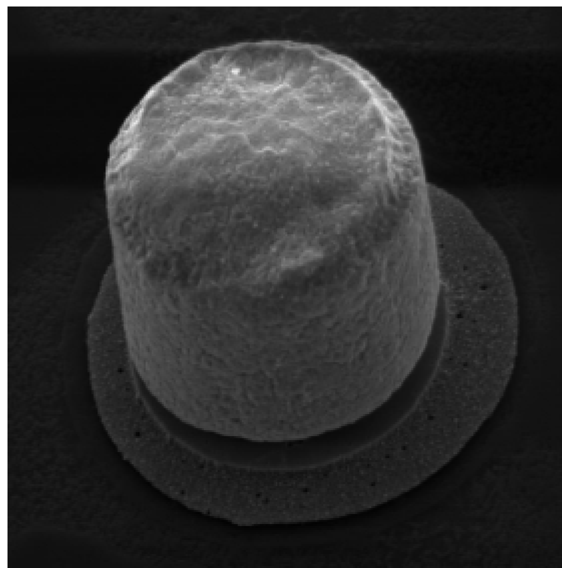

Figure 4.3: Copper interconnects measuring 25 μm wide and 20 μm tall [195]

For this verification run, finite element models simulating the experimental low cycle fatigue conditions were developed using ABAQUS, commercial finite element software. This is to measure the stress intensity values around the crack front needed for predicting crack growth and shape evolution. Due to the symmetry in a round bar in the fatigue specimens, only half of the 6.35 mm diameter round bar is modeled in this research using 20 nodes quadratic and isoparametric elements as shown in Figure 4.4. Linear elastic material constants are input into ABAQUS as material properties. Furthermore, in order to simulate the experimental condition, this model is subjected to a tension load of 1240MPa.

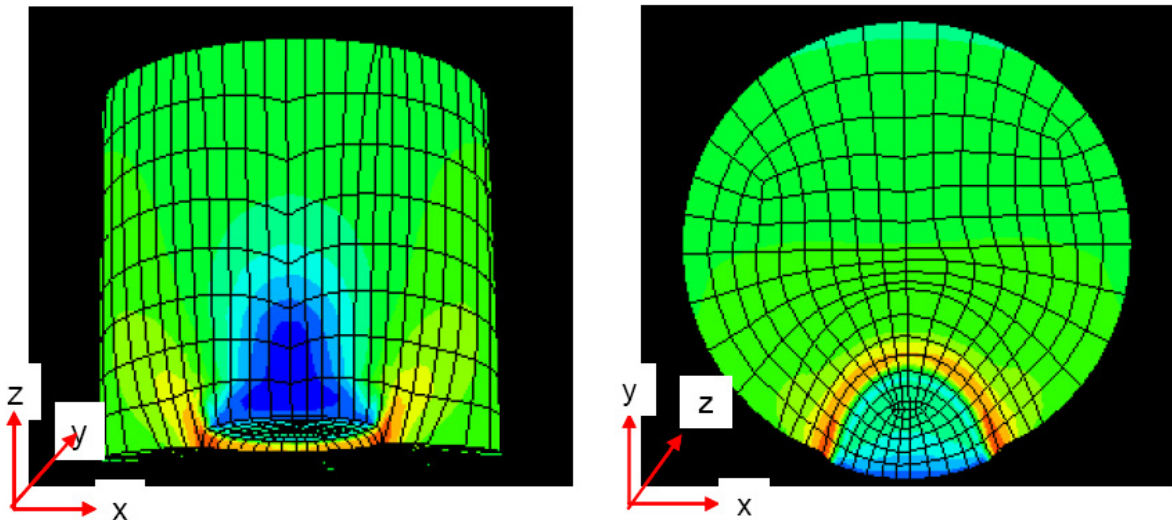

Figure 4.4: Finite element model of a semi-elliptical crack in a round bar used in this analysis

The value of the J-integral is then computed around the crack tips using only the loading portion of the fatigue cycle, where total stress range, $\Delta\sigma$, is a monotonic function of only the total strain range, $\Delta\varepsilon$ [196]. Furthermore, since the value of J is calculated from the energy within a remote boundaries consisting of the crack tip, it is not necessary to account for the stress singularly at the cracks tip through the use of the quarter node element. A matrix of finite element simulations with different crack geometry is conducted in order to obtain J as a function of its geometry.

Figure 4.5 shows the comparison between the values of *J* obtained from Newman and Raju solution, and linear elastic finite element analyses conducted in this research. Only values of J at crack angle ϕ=0° and ϕ=60° is computed.

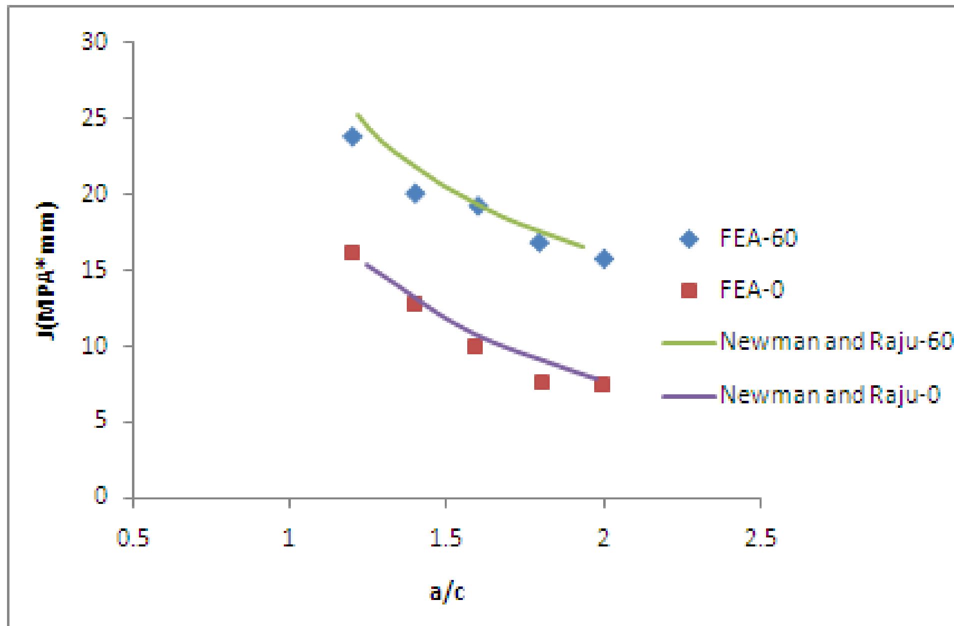

Figure 4.5: Comparison between the J-integral results obtained from Newman and Raju, and finite element analyses in this research [197]

Figure 4.5 shows that Newman and Raju solution can predict the finite element results very well even though the solution is for a semi-elliptical crack in a rectangular bar. Hence Newman and Raju solutions can be used to computed the value of F_e in this research.

There is also a need to investigate the accuracy of finite element/Newman-Raju results. Since fatigue striation marks track the evolution of the crack on the fatigue specimen, it is the best methods for validation of the crack evolution calculation in finite element analysis. Hence, it is advantage to use RENE88 as the benchmark material for validation, instead of copper, since fatigue crack striations can be observed easily on RENE88 as shown in Figure 4.6. These striation marks will provide a few valuable experimental verification data points.

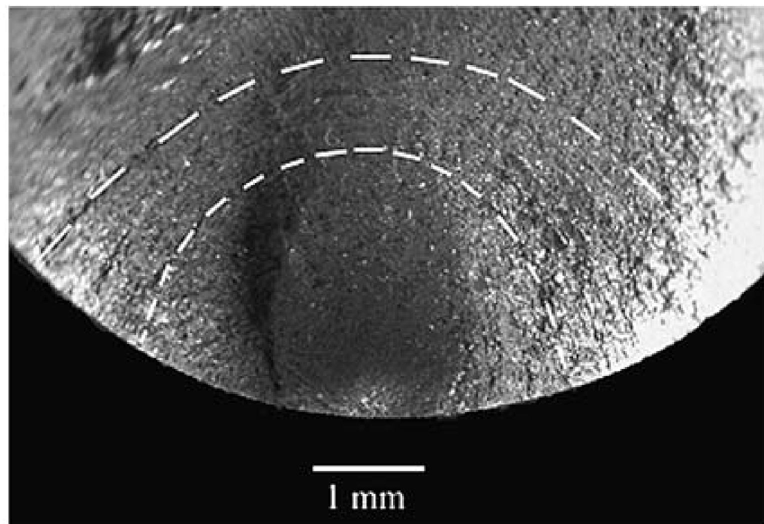

Figure 4.6: Fatigue crack striations marking on RENE88 [197]

Again, the commercial finite element software ABAQUS will be used in this verification exercise. In order to accurately describe the material response, Ramberg–Osgood plastic hardening relationship [198] as shown in equation 4.13 are input into the finite element software.

The Ramberg-Osgood constants in Equation 4.13 can be computed by regressing with $\Delta\sigma$ versus $\Delta\varepsilon$ curve obtained from the loading potion of low cycle fatigue experiments.

$$\Delta\varepsilon = \frac{\Delta\sigma}{E} + 2\alpha'\left(\frac{\Delta\sigma}{\sigma_0^c}\right)^m \quad (4.13)$$

In equation 4.13, *α'* and *m* are Ramberg–Osgood plastic hardening constants for fatigue loading, σ_0^c is the cyclic yield stress and *E* is the elastic modulus.

The hardening constant for RENE88 are calculated to be as follows [194]

$\alpha' = 0.00049$

$m' = 8$

$\sigma_o^c = 815 MPa$

Finite element analysis in addition to the crack growth data found in Findley[197] is used to perform the crack growth evolution analysis. Figure 4.7 shows the comparison of both the experimental results and the finite element results. Although Figure 4.7 shows that finite element predicted a slightly higher crack evolution rate, both results were comparable. [197]

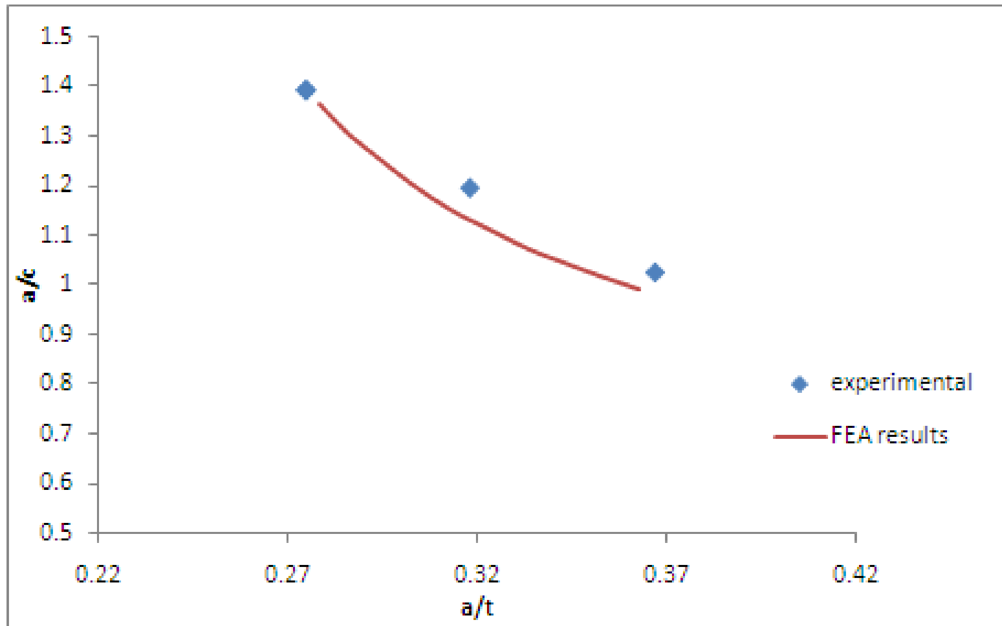

Figure 4.7: Comparison of experimental measured aspect ratio evolution with respect to the finite element solution

Since Figure 4.5 shows close agreement between finite element analysis and Newman and Raju formulation whereas Figure 4.7 shows closed agreement between experimental and finite element results, Newman and Raju formulation is assumed to accurately compute the value of F_e for an elliptical crack in a cylindrical bar.

4.3 Material Properties for Crack Growth Analysis of Interconnects

The finite element analysis calculation by Bansal et al [8] had showed that a 50 µm pitch microcrystalline copper interconnects would experience a cyclic stress range of 200MPa and a cyclic plastic strain range of 0.0635 during operation. At this stress level, the microcrystalline

copper interconnect will experience plastic deformation whereas the nanocrystalline copper interconnect will only experience largely elastic deformation due to its enhanced strength. In any case, in order to model the correct material response, elastic modulus and Ramberg–Osgood plastic hardening relationships are needed to fully account for elastic and plastic contributions to the crack driving force in the analysis of nanocrystalline copper and microcrystalline copper.

4.3.1 Nanocrystalline Material

As discussed above, there is a need to accurately characterize the elastic modulus of nanocrystalline copper. However, due to the difficulty in controlling the grain size of nanocrystalline copper during material processing as compared to the ease of controlling grain size in simulation, molecular simulation is used to characterize the elastic modulus for different grain sizes in this research.

LaMMPS [199], a molecular dynamics code developed by Plimpton and his coworkers at Sandia National Laboratories, is used. Furthermore, domain decomposition technique using MPI message passing libraries to perform parallel calculation is also implemented in this code. The material response in this research will be modeled using the EAM potential formulated by Folies et al [181]. The verification of this potential will be discussed in Chapter 5.

In order to investigate the effect of the grain size on the evolution of the crack, Voronoi tessellation methodology [191] is used to construct bulk nanocrystalline copper with a grain size of 5nm, 10nm and 15nm respectively. Figure 4.8 shows a typical nanocrystalline microstructure used in this project. The verification of the nanocrystalline microstructure simulated using this method will be discussed later in Chapter 5. In order to minimize the computational effort while

still maintaining a realistic microstructure model, a 20nm by 20nm by 20nm simulation cell size consisting of about 70,000 atoms is constructed. 3D periodic boundary conditions are also enforced throughout this work so as to minimize the surface effect.

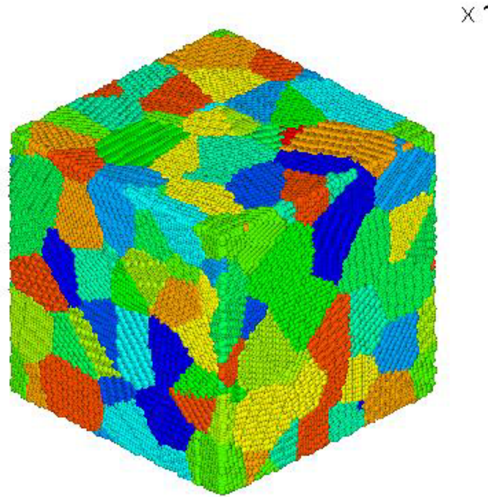

Figure 4.8: A typical nanocrystalline microstructure constructed using Voronoi method

Figure 4.8 shows one of the nanocrystalline microstructure used in this project. For this model, the average grain size is about 5nm and this value of average grain size is estimated through computing the volume of each unit cell and keeping track of the number of atoms in each grain. The whole simulation cells consist of 123 individual grains with random orientation. In order to generate a realistic initial microstructure with no residual stresses; the microstructure is subjected to molecular statics and NPT equilibration at ambient condition (300K at atmospheric pressure) for 50ps. The parameter centro-symmetry is also used during post-processing to distinguish the atoms at the grain boundaries from the atoms in the crystal interior.

Using a value of less than 0.1 for atoms at the grain boundaries, the volume fraction of grain boundaries as a function of grain size is computed as shown in Figure 4.9.

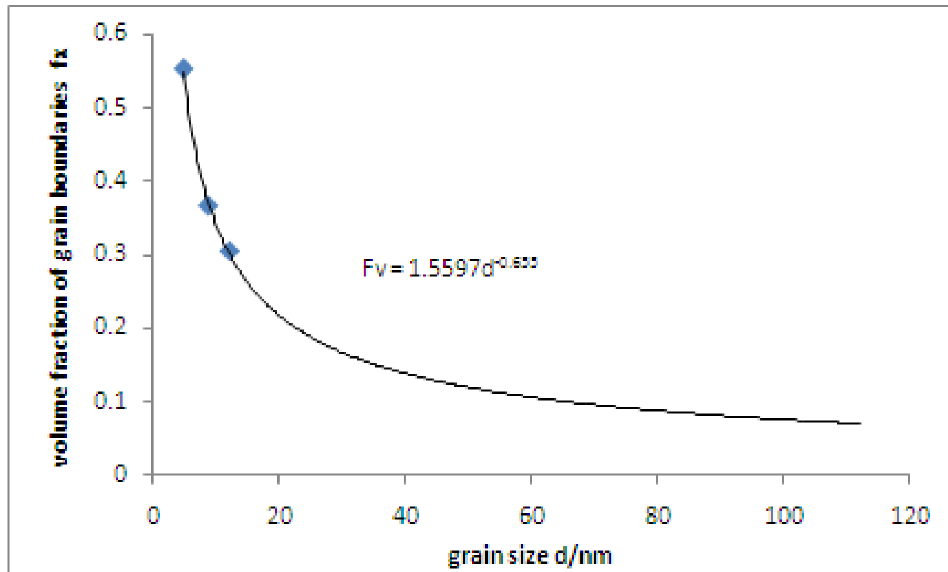

Figure 4.9: Computed grain boundaries volume fraction as a function of grain size

As shown in Figure 4.9, the expression for volume fraction as a function of grain size is given by

$$f_v = 1.5597D^{-0.655} \quad (4.11)$$

In equation 4.11, f_v is the volume fraction of the grain boundary atoms whereas D is the average grain size of nanocrystalline copper. Figure 4.9 also shows that the volume fraction of grain boundaries increases significantly for grain size is smaller than 100nm (100nm length scale is often used to formally define nanocrystalline materials). It also emphasizes the importance of grain boundary effects in nanocrystalline copper.

After characterizing the volume fraction of grain boundaries with respect to the grain size, deformation of nanocrystalline materials is then performed at a constant strain rate of 1ps^{-1} in the y-direction for each simulation using the equations of motion for the NEPT ensemble. Mechanical stress is computed by the virial theorem as was shown earlier in equation 3.30 whereas the normal strain will be computed as follows:-

$$\varepsilon = \ln(\frac{L}{L_0}) \tag{4.12}$$

In equation 4.12, L is the instantaneous length in the y-direction and L_0 is its initial length in the y-direction. Hence, the stress–strain curve can be computed using equations (3.30) and (4.12) and the elastic modulus is determined from the linear regression analysis of the stress-strain points obtained from the initial portion of the stress-strain curve. Since the rule of mixtures is elected to explain the dependency of the grain size, the modulus will be regressed with a linear relationship as shown in Figure 4.10.

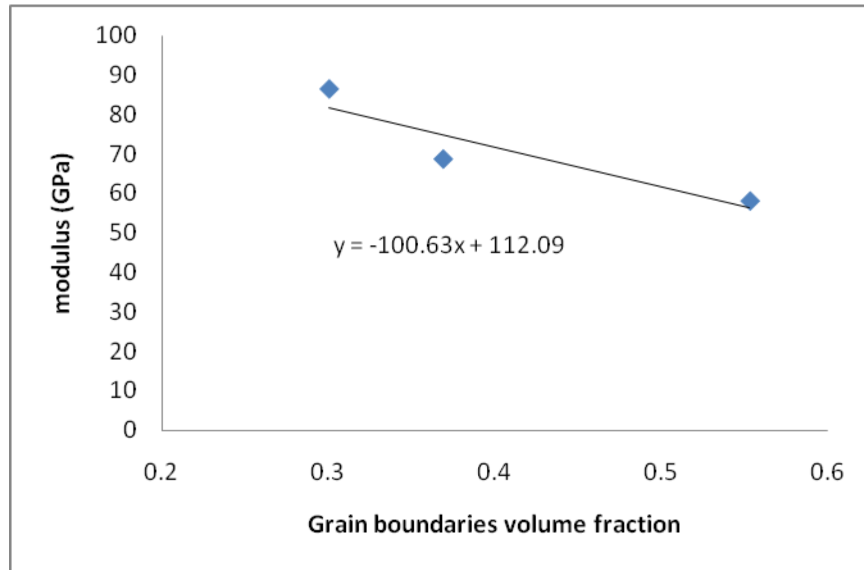

Figure 4.10: The function of elastic modulus as a function of grain boundaries volume fraction

As shown in Figure 4.10, the expression for volume fraction as a function of grain size is given by

$$E = 112.09 + 100.63 f_v \tag{4.13}$$

Using the rule of mixtures, the elastic modulus for grain boundary free copper is computed to be 112GPa whereas the modulus of grain boundary modulus is computed to be 12GPa. The modulus of 112GPa is consistent with 110GPa [11] commonly used for microcrystalline copper where the volume fraction of grain boundaries is negligible. Furthermore, the elastic modulus for a 50nm nanocrystalline copper, computed using equation 4.10 and equation 4.1, is found to be 100.4 MPa whereas the elastic modulus of a 50nm ECAE copper is characterized experimentally to be 100MPa. This will again validate the accuracy of equation 4.10 and 4.11. Hence, the modulus of the nanocrystalline materials has been accurately characterized for this analysis.

4.3.2 Microcrystalline Copper

As mentioned in section 4.3, Ramberg–Osgood plastic hardening parameter in addition to the elastic modulus needs to be characterized in order to model the correct material response for microcrystalline copper. The Ramberg-Osgood constants is obtained from the regression analysis of stress strain data in Bansal et al [8] in conjunction with the modulus of 112GPa computed in section 4.3.1, as shown in Figure 4.11.

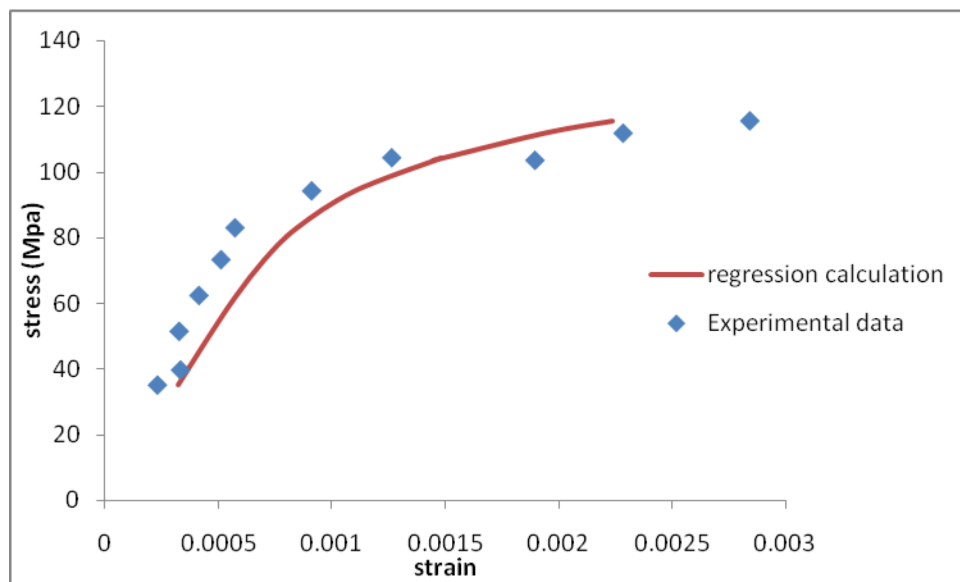

Figure 4.11: Regression of experimental data with Ramberg–Osgood relationship for microcrystalline copper

The hardening parameters are as follows

$$\alpha' = 0.000817$$

$m' = 7.8$

$\sigma_o^c = 100MPa$

Hence, the material properties needed for the crack evolution analysis had been characterized.

4.4 Crack Growth Analysis

As discussed earlier, finite element analysis calculation by Bansal [8] showed that the 50 μm pitch microcrystalline copper interconnects experienced a cyclic stress range of 200MPa and a cyclic plastic strain range of 0.0635 during operation. Hence, this loading condition will be used in this research. Since nanocrystalline copper will experience only linear elastic response under these conditions, only linear elastic portion of J-integral will be needed for the analysis of crack growth in nanocrystalline copper interconnects.

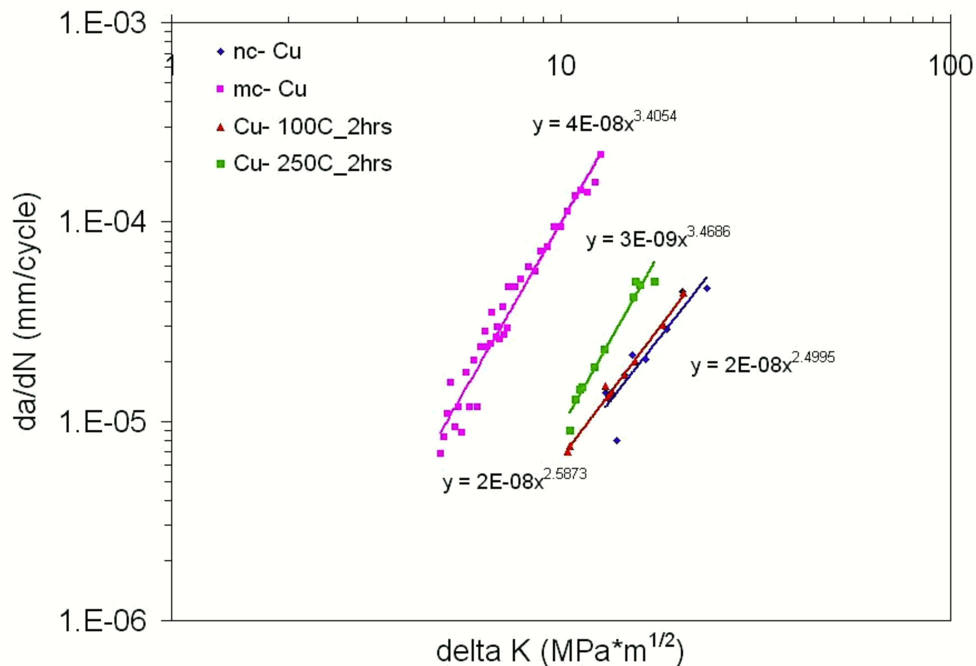

Figure 4.12: da/dN- ΔK behavior for nanocrystalline and microcrystalline copper [8]

Since the failure morphology of nanocrystalline materials usually consists of dimples several times larger than their grain size [13], the initial crack length is assumed to be 4 times the average grain size in this research. Using the diameter of copper interconnects to be 25 µm and the crack growth data, as shown in Figure 4.12, found in the literature, the crack evolution of microcrystalline copper interconnect and nanocrystalline copper interconnect subjected to fatigue loading is computed as shown in Figure 4.12. Even though Figure 4.12 shows that nanocrystalline copper has a much lower da/dN- ΔK rate, this is not true at lower ΔK as shown in Figure 4.13 with the change over at ΔK value of 0.463 MPa*m$^{0.5}$.

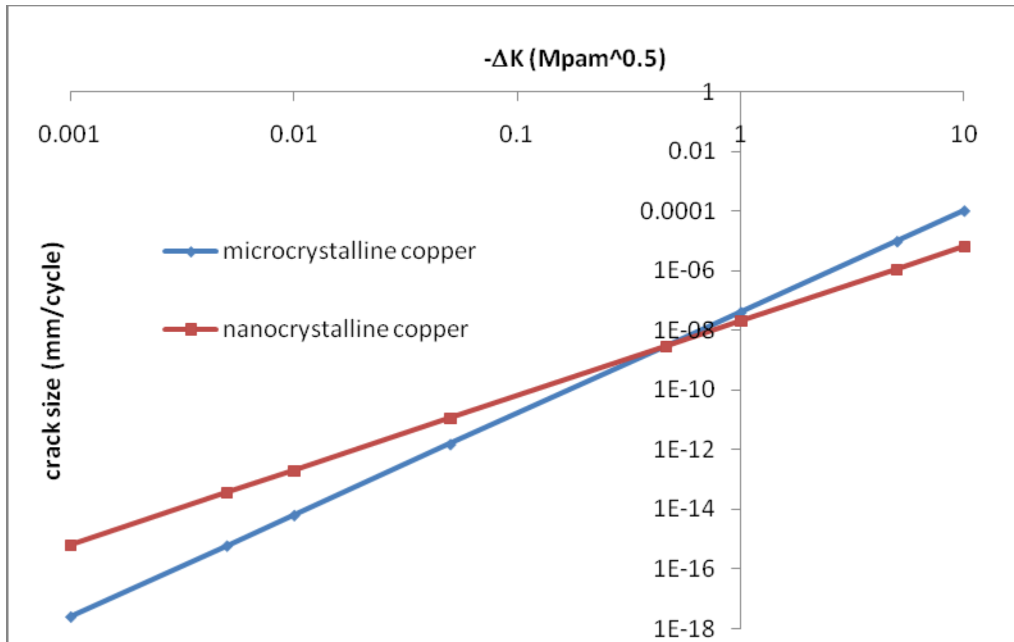

Figure 4.13: da/dN- ΔK behavior for nanocrystalline and microcrystalline copper at lower ΔK values

Even though Figure 4.13 shows that nanocrystalline copper has a much lower da/dN- ΔK rate, the crack evolution analysis in Figure 4.14 shows that the unstable crack growth for microcrystalline copper is found to have occurred at a much earlier stage as compared to the nanocrystalline copper. Unstable crack growth occurs at around 3000 cycles for microcrystalline copper whereas it is expected to occur at around 4000 cycles in nanocrystalline copper for this particular loading condition. This is a 33.3% increase in the crack growth life for nanocrystalline copper. The reason for this enhanced fatigue life of nanocrystalline copper is due to its enhanced strength and fatigue crack growth resistance. Since nanocrystalline copper is still in the elastic regime for this loading condition, less damage will be induced during each cycle. Thus, nanocrystalline copper is a much better candidate for the application of interconnects for high pitch applications.

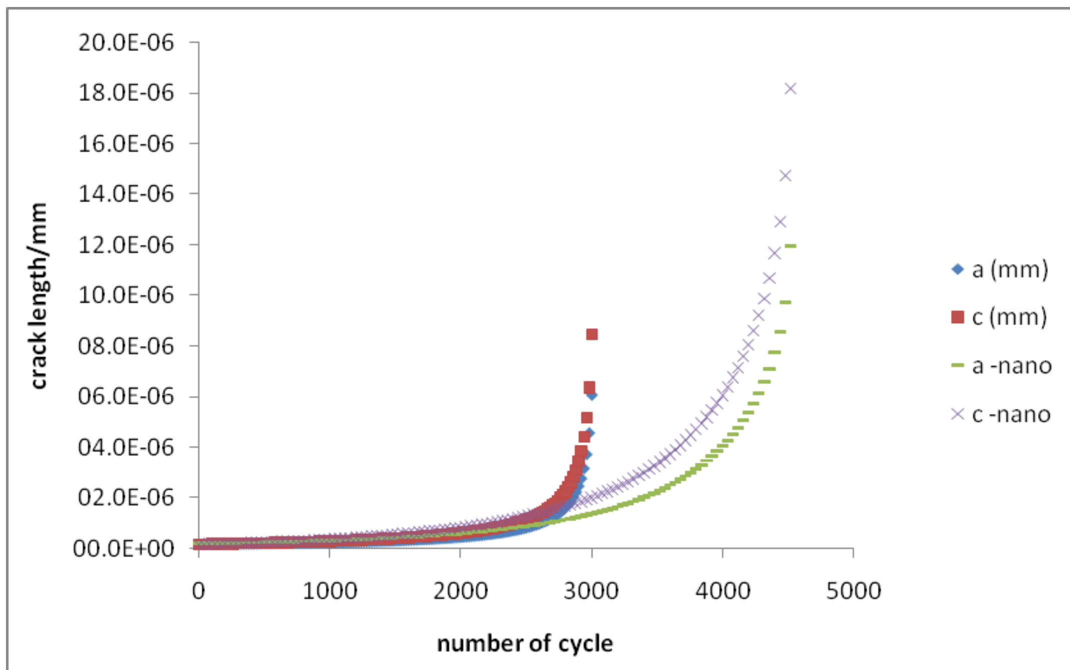

Figure 4.14: Crack evolution of nanocrystalline copper and microcrystalline copper.

Furthermore, Bansal et al [8] had showed that the total cycle to failure for a 50µm pitch nanostructure interconnects subjected to a loading condition of 400MPa was 2634 cycles. Hence, the same loading condition is applied to our analysis on nanocrystalline copper to determine the significance of the crack growth life as compare to total fatigue life. Microcrystalline copper is not investigated for this analysis as they will not be able to withstand such a high load. Figure 4.15 shows the computed crack growth evolution for two aspect ratio of a/c.

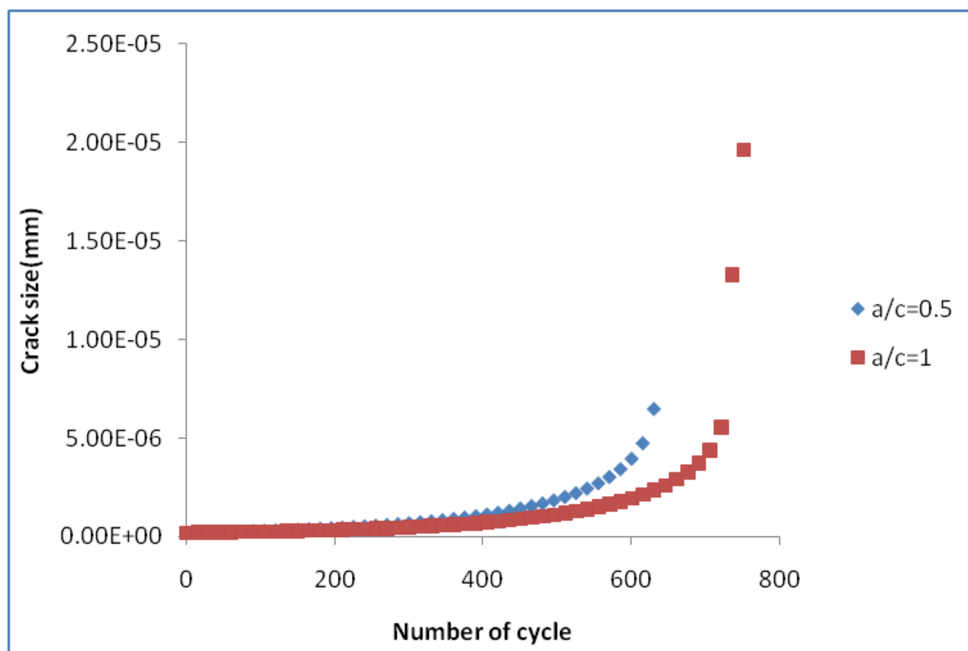

Figure 4.15: Crack growth evolution for nano-crystalline copper with different initial a/c ratio.

Figure 4.15 shows that the unstable crack growth for nanocrystalline copper occurs at around 600-700 cycles whereas Bansal et al[8] had predicted the total cycle to failure for nanostructured-interconnects to be 2634 cycles. Hence, the crack propagation is only one fifth of the total life. This leads to the conclusion that the long crack growth accounts for a relatively

small portion of the total fatigue life of the material for the experimental LCF conditions. Hence, initiation of the cracks in the interconnection is the main criterion used to predict its fatigue life.

4.5 Conclusions from Crack Growth Analysis

In conclusion, an accurate closed form solution, for studying 3-D semi-elliptical crack growth in round bars subject to uniaxial fatigue loading in both linear-elastic and elastic–plastic low cycle fatigue (LCF) condition, has been developed in this research. Furthermore, finite element analysis using the stress intensity parameter, J-integral, was used to validate the Newman and Raju solution for the computation of the value of F_e. The applicability of these solutions was also validated by experimental data on Rene' 88 Nickel base alloy in a separate study very pertinent to our work here. Furthermore, molecular dynamics was employed in conjunction to the rule of mixtures to characterize the modulus for nanocrystalline materials as a function of grain size that is needed for the crack growth analysis.

The results indicate that nanocrystalline copper is in fact a suitable candidate for ultra-fine pitch interconnects applications. . This study also predicts that crack growth is a relatively small portion of the total fatigue life of interconnects under LCF conditions. Hence, crack initiation life is the main factor in determining the fatigue life of interconnects.

CHAPTER 5

MOLECULAR SIMULATION OF MECHANICAL BEHAVIOR OF SINGLE CRYSTAL AND NANOCRYSTALLINE COPPER

5.1 Introduction

As discussed in Chapter 2 and Chapter 4, one of the potential solutions to dramatically increase the density of electrical interconnections is to use nanocrystalline copper as the interconnection material because of its superior strength and fatigue properties and its electrical conductivity. However, more studies are still needed to fully understand the deformation, fracture and fatigue mechanisms for the nanocrystalline materials. Molecular dynamics simulations are an effective substitute for conducting difficult experimental measurements of properties to enhance our understanding of phenomena at the nanometer length scales. However, as discussed in Chapter 2, it will be critical to first validate the inter-atomic potential and the techniques for generating the correct nanostructures used in these computations. The nanostructures must be representative of the interconnect whose behavior we are attempting to simulate. Hence, in this chapter, verification studies on the inter-atomic potential and initial microstructure used in this research will be discussed first. Subsequently, this chapter will also present the results of the atomistic simulations of the behavior of single crystalline copper nano-rods and bulk nanocrystalline copper subjected to monotonic and cyclic loading. Their ability to withstand the high mechanical requirements for interconnects will be assessed.

5.2 Single Crystal Analysis

This section describes the atomistic simulation results on the behavior of single crystalline copper nano-rods subjected to monotonic and cyclic loading. Since pair- potential is known for its inability to accurately reproduce the material properties of some of the metals, a verification study on the Lennard-Jones potential used in this single crystal study will be conducted by calculating the elastic modulus in the [100] and [110] crystallographic directions and comparing them with experimental values. Furthermore, systematic atomistic simulations have been conducted on the crystallographic effect on the deformation mechanisms for single crystals with crystallographic orientation <100> and <110>. The strain rate sensitivity and temperature dependency on the nucleation stress on single crystal copper nano-rod has also been investigated. Hence, this study on single crystals will be an effort to establish some base line behavior.

For this study, a molecular dynamics code, using only single processor, developed as part of this study will be used. Furthermore, the atomistic interactions will be described by the widely used Lennard-Jones potentials. The Lennard-Jones parameters σ and ε in in these simulations are chosen to be 2.3377Åm and 0.4093eV respectively [174].

5.2.1 Verification of the Model Used.

For the validation run, perfect single crystal copper nano-rod with a cubic simulation size of 4 x 4 x 15 lattice unit as shown in Figure 5.1 was used as a model for computational efficiency. Furthermore, in order to achieve a stress free initial microstructure, this nano-rod is subjected to NPT equilibration at 300K and atmospheric pressure for 20ps. Furthermore, the common

neighbor analysis is used during post-processing to determine the type of bonding between each atom.

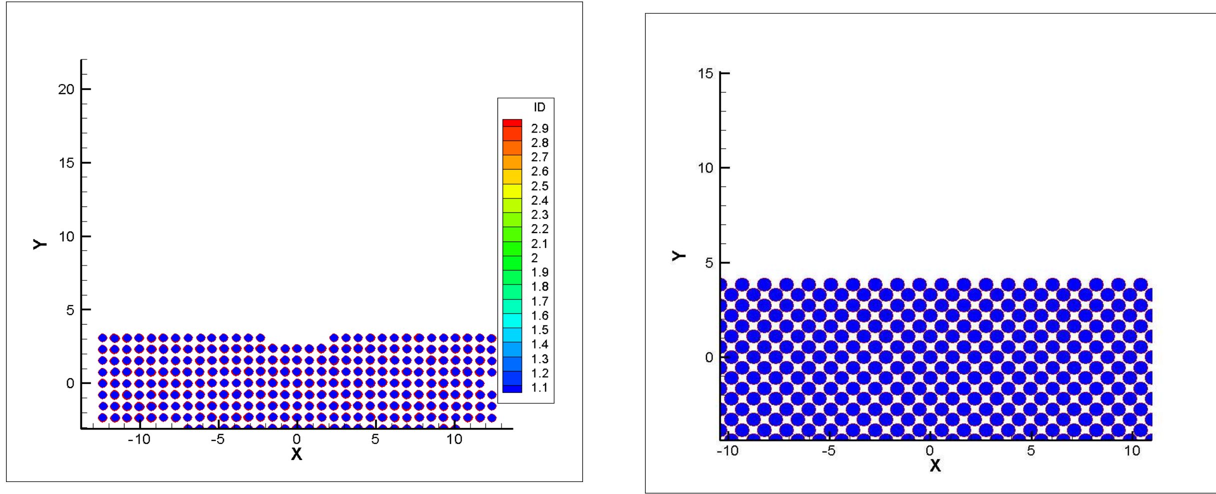

Figure 5.1: Initial microstructure with <100> and <110> crystal orientation.

The equation of motion for NVT ensemble with enforced 3D periodic boundary conditions is used extensively to simulate the deformation of the single crystal study. The loads on this model are applied by changing the size of the simulation according to the displacement given by linear elasticity. The stress–strain curve can be computed using equations (3.30) and (4.12) and the elastic modulus is determined from the linear regression analysis of the stress-strain points obtained from the initial portion of the stress-strain curve.

The elastic moduli for single crystal copper deformed at 300K along the crystallographic orientation <100> and <110> is computed to be 110GPa and 150GPa respectively. These computed moduli are comparable in the value, as shown in Table 5.1, obtained experimentally using bulge test from the work of Xiang et al [200]. The largest deviation between simulation and experimental values of the Young's modulus is in the [110] orientation and it is

approximately 5%. Hence, Lennard-Jones potential used in this research can model the material properties of single crystal copper quite accurately.

Table 5.1: Summary of the elastic modulus values from experiments[200]

Crystal orientation	<111>	<110>	<100>	<112>	<023>
Elastic modulus (GPa)	158.2	143.9	106.2	135.2	114.5

5.2.2 Microstructural Evolution

Figure 5.2 shows the evolution of the microstructure of single crystal nano-rod as it is subjected to uniaxial tensile loading. Homogenous nucleation of dislocation occurs at the onset of yielding as shown in Figure 5.2b. Furthermore, distortion from the regular FCC structure is observed around the nucleation site suggesting the need for cooperative atomic shuffling of atoms in order for nucleation of partial dislocations. The magnitude of the tensile stress required for the nucleation of the first partial dislocation is calculated to be 8.0GPa for <100> and 4.0GPa for <110>. This is slightly higher than or equal to the result for 0.2% yield strength result which is 5GPa and 4GPa respectively. Furthermore, the ab initio calculations of Ogata et al [201] had shown that stress components acting normal to the slip plane can affect the critical resolved shear stress in copper for dislocation nucleation. This is consistent to the molecular dynamics results from this study in which the computed critical resolved shear stress (CRSS) is 2.4GPa and 1.836GPa for crystallographic direction of <100> and <110> , respectively [202]. this is within 15% of the CRSS calculated in the molecular dynamics study conducted by Tschopp et al [202].

The difference is due to the inability for Lennard-Jones potential to accurately simulate the nucleation of dislocations in certain metals.

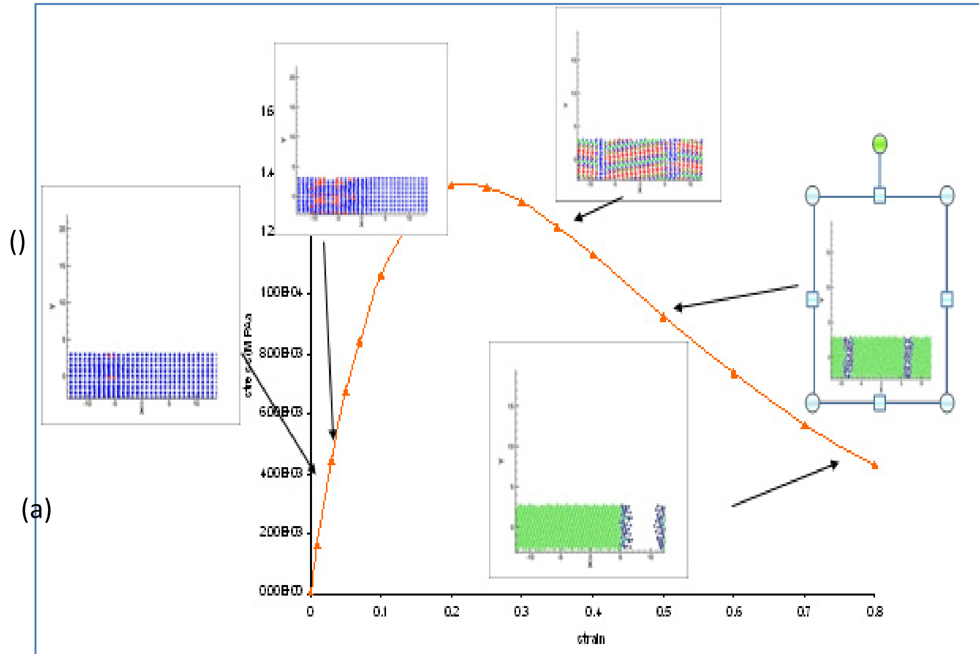

Figure 5.2: Evolution of the microstructure during tensile loading

Figure 5.2c shows the propagation of these partial dislocations as the straining increases. Further straining of the nano-rod causes more dislocations to be nucleated until the formation of alternate intrinsic stacking fault as shown in Figure 5.2d. This is consistent with the experimental observation at some region of necking. Further straining causes the grain to rotate to a more favorable orientation and formation of vein like wall-structure as shown in Figure 5.2e. Lastly, fracture occurs at these veins as shown in Figure 5.2f.

5.2.3 Temperature and Strain Rate Effects

In order to investigate the relationship between temperature and strain rate and the nucleation of dislocations in a single crystal nano-rod, a matrix of conditions for the atomistic simulations consisting of 3 different strain rates and 4 different temperatures was selected. The strain rates chosen were $1.4x10^8 s^{-1}$, $2.3x10^8 s^{-1}$ and $4.5 x10^8 s^{-1}$ and temperatures selected were 30K, 157K, 300K and 500K respectively.

Figure 5.3 shows the influence of temperature on the stress required for dislocation nucleation in single crystal copper nano-rod. Since thermal energy aids the dislocation nucleation process, the peak stress decreases with increasing temperature as expected. Similar thermally activated dislocation process appears to be dominant at all three strain rates as seen Figure 5.3. The exponential constants are approximately 30J /mol.K for all the three strain rates.

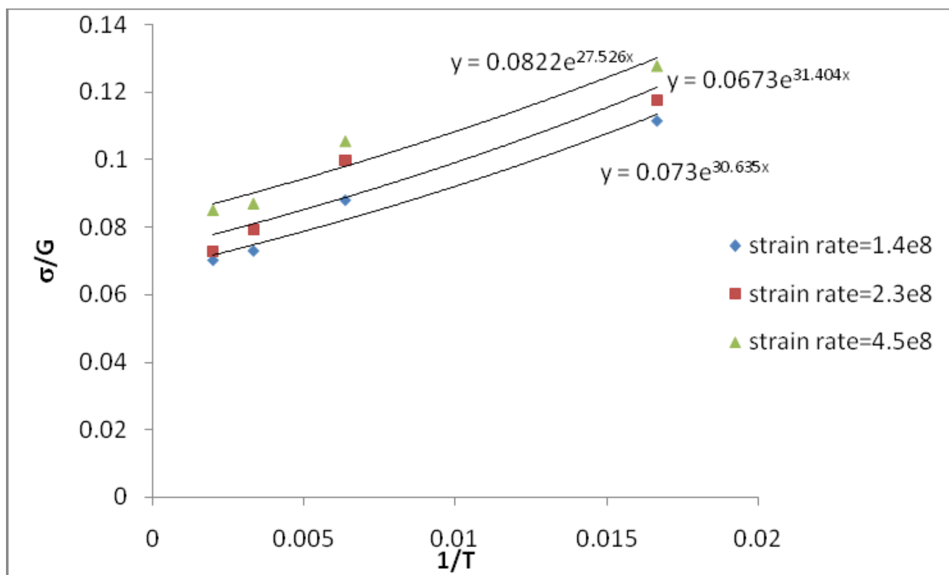

Figure 5.3: Influence of the temperature with different loading rate

Similarly, Figure 5.4 explores the influence of strain rate on the stress required for dislocation nucleation in single crystal copper at various temperatures..

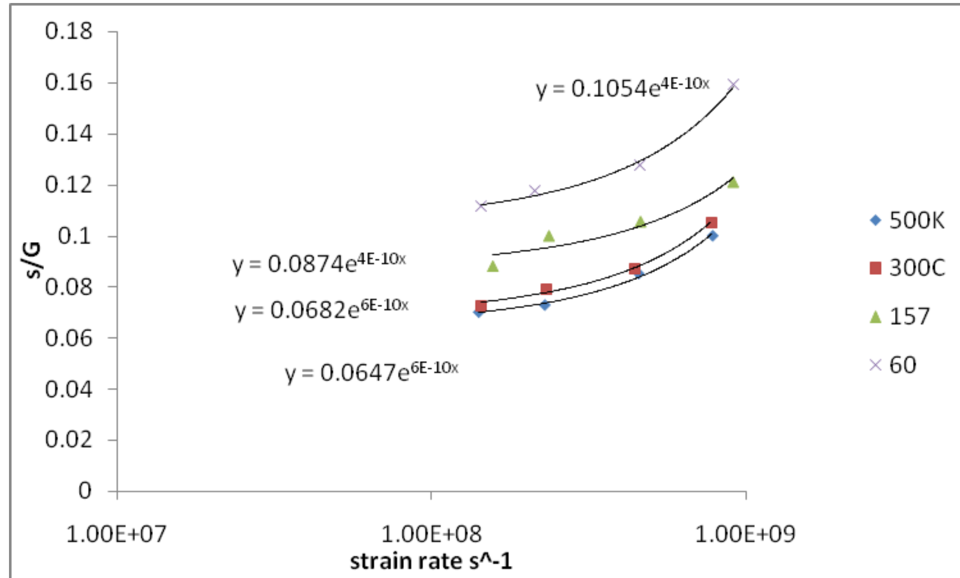

Figure 5.4: Relationship of the influence of the strain rate on nucleation stress

Extrapolating the data shown in Figure 5.4 to the experimental loading rate predicts the insensitiveness of the stress required to nucleate dislocations to the applied strain rate which agrees with the experimentally observed behavior.. This observation can be reinforced by the comparison of the computed strain rate sensitive *m* with the experimental results [203].

$$m = \frac{\partial(\ln(\sigma))}{\partial(\ln(\dot{\gamma}))} \tag{5.1}$$

Figure 5.5 shows that the computed strain rate sensitivity is comparable to that of coarse grain copper where the volume fraction of atoms that lie on the grain boundaries is negligible. This is

important to note that the slightly higher value of strain rate sensitivity predicted by the numerical model is due to the smaller activation volume resulting from the 3D boundary condition and the relatively small number of atoms considered in the model..

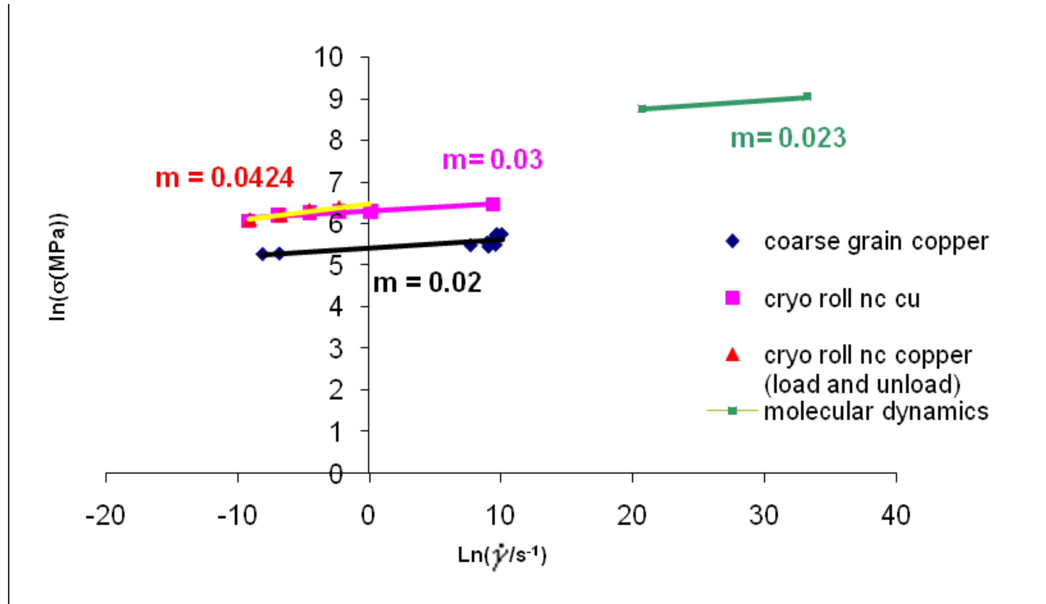

Figure 5.5: Comparison of computed m with experimental result obtained from Wang et al. [203]

As discussed above, the nucleation stress is dependent on both the strain rate and the temperature at which the deformation occurs. Noting the trend in Figure 5.3 and Figure 5.4 and performing regression of these data, the nucleation stress can be computed from equation 5.2.

$$\frac{\sigma_0}{G} = 6.31 * 10^{-2} e^{\left(\frac{229}{RT} + 6.2*10^{-10}\,\dot{\varepsilon}\right)}$$

$$\approx 6.31 * 10^{-2} e^{\left(\frac{229}{RT}\right)} \qquad (5.2)$$

In equation 5.2, σ_0 is the nucleation stress, *G* is the shear modulus, *R* is the molar gas constant, $\dot{\varepsilon}$ is the strain rate and *T* is the temperature in Kelvin. Figure 5.6 shows the close agreement between regressed value and the molecular dynamics experiment values

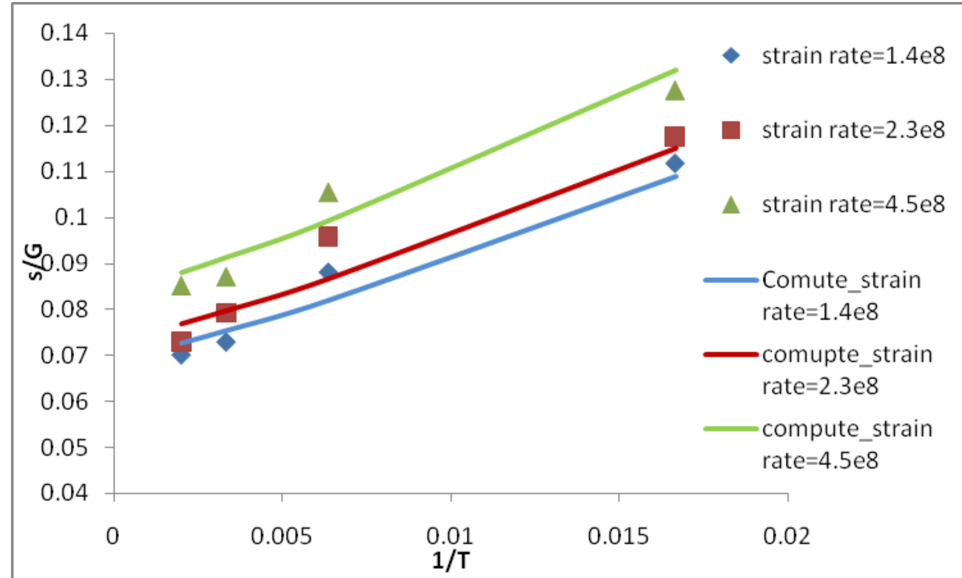

Figure 5.6: Close agreement between the regressed values and the molecular dynamics values

In order to identify the dominant controlling mechanism in single crystal nano-rods, the activation volume *V* as a function of the temperature is computed and is shown in Figure 5.7. The activation volume is obtained from the following equation [113]

$$V = \sqrt{3}kT\frac{\ln\left(\frac{\dot{\varepsilon}_1}{\dot{\varepsilon}_2}\right)}{\Delta\sigma_0} \tag{5.3}$$

In equation 5.3, *k* is the Boltzmann's constant, σ_0 is the yield stress and $\varepsilon^{\cdot}$ is the strain rate

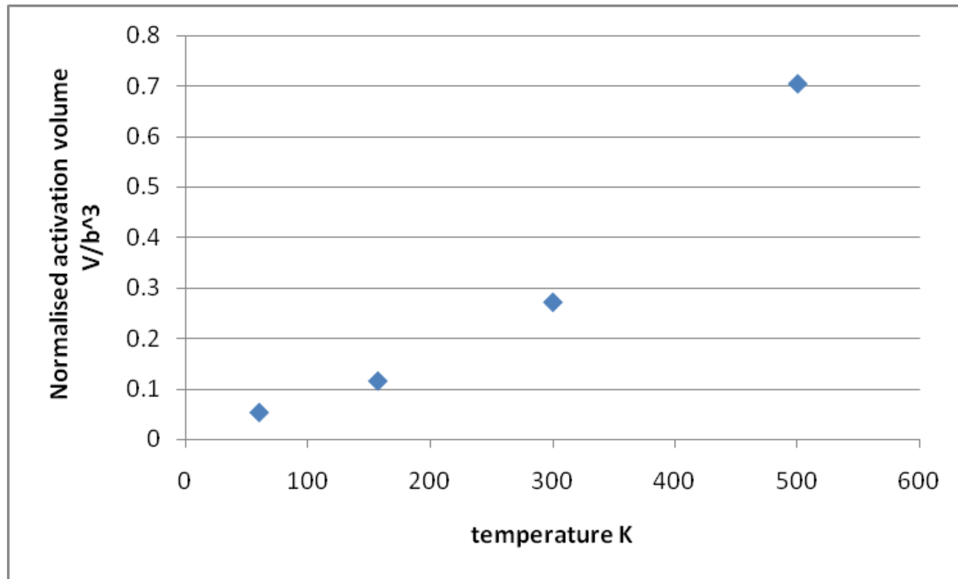

Figure 5.7: The relationship of activation volume as a function of temperature

The magnitude of the activation volume for cutting through the forest dislocations in the lattice is of the order of several hundred to a thousand times of the cube of burgers vector i.e. ~100-1000b^3 whereas the magnitude of the activation for nucleation of partial dislocation is of the order of ~3-10b^3 [204]. Since the activation volume as shown in Figure 5.7 is in the orders ~b^3, the controlling mechanism in this single crystal nano-rod must be the nucleation of dislocation. This discrepancy between the computed value and the experimental values is due to the small length scale of the model used in this research (on the order of only nanometers) in addition to the 3D boundary condition enforced in the model: due to the 3D periodic boundary condition and the small length scale of this model, any dislocation nucleated will induce 8 other image dislocations nucleated within the length of 3nm inclusive of the image cells. Although this will underestimate the magnitude of the activation volume, the conclusion for the controlling mechanism in the deformation in this nano-rod will be unaffected and must be the nucleation of dislocation.

5.2.4 Cyclic loading

Since the main objective of this research is to investigate and understand the fatigue resistance of nanocrystalline-materials, there is a need for a base line study on the fatigue behavior of microcrystalline copper. However, it will be computational too expensive to model microcrystalline copper so the fatigue behavior of single crystals will be used instead to establish some base line behavior. For this study, the same single crystal nano-rod copper model as used in the monotonic loading is employed. Furthermore, R-ratio equal of zero will be applied through updating the size of the simulation according to the dislocation given by linear elasticity. The single crystal nano-rod will be considered to have failed if it has lost 50% of its peak load carrying capability. Because cyclic loading is so computationally intensive, only room temperature simulations will be performed.

Figure 5.8 compares the fatigue life of single crystal copper to the fatigue life of coarse grain copper where grain boundaries are negligible. It has been observed that the fatigue of the single crystal nano-rod is slightly shorter than that of microcrystalline copper. Again, the slightly shorter life in the single crystal nano-rod is due to the small length scale of the model and the prescribed 3D boundary conditions which tend to over-estimate the deterioration of the sample.

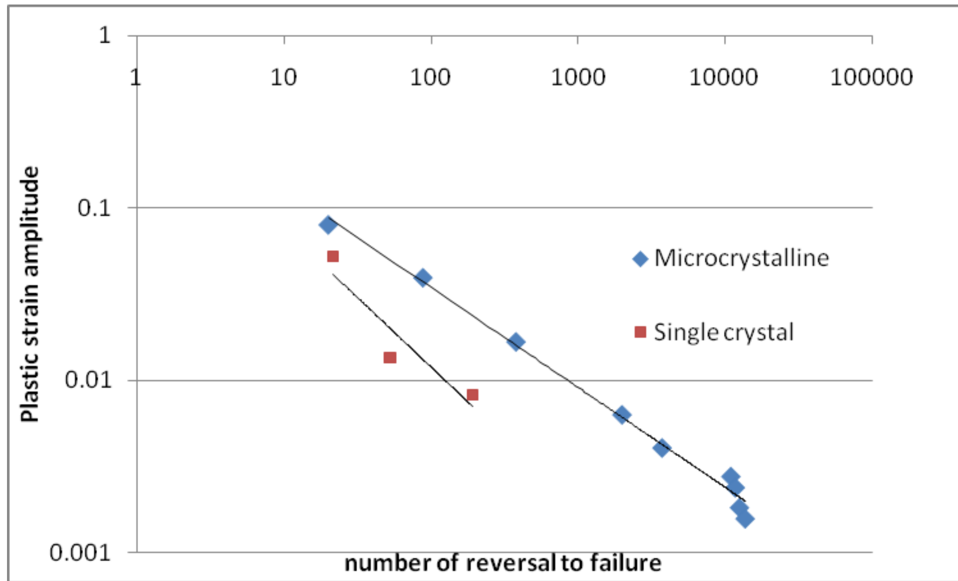

Figure 5.8: Comparison of the computed fatigue life of single crystal and experimental fatigue life of microcrystalline copper

5.3 Nanocrystalline Copper

As discussed in Chapter 2, it will be critical to first verify the ability of the inter-atomic potential used in this work to accurately model the deformation of copper. Hence, a verification study on the EAM potential used in this research is conducted by calculating the stacking fault energy and comparing with established results. Then, since grain boundary structure at the atomic level of the grain boundary plays a major role in the deformation process, it is critical to model the grain boundaries and the grains as realistically as possible in order reasonable conclusions from this study. As discussed in Chapter 2, the grains of ECAE copper are more equi-axial and randomly orientated as the number of passes increases [37]. Therefore, there is need to verify that the grains in the model used in this research are also equi-axial and randomly orientated.

After the discussion of the verification results on both the inter-atomic potential and the microstructure used in this research, the mechanical properties and the behavior of nanocrystalline materials will be discussed. This includes the Young modulus, yield strength and the deformation mechanism followed by the results on the fatigue behavior.

Due to the large number of atoms necessary to describe a realistic grain structure, there is a need for an efficient and massively parallel implementation of the dynamics which places a high demand on computing hardware stability during the simulations. LaMMPS [199], a molecular dynamics code developed by Plimpton and his coworkers at Sandia National Laboratories, is used for the study of the nanocrystalline copper. One of the main advantages of LaMMPS is its ability to perform parallel calculations through the implementation of domain decomposition technique using MPI message passing libraries. Furthermore, copper EAM potential formulated by Folies et al [181] will be used to model the material response in this study on the nanocrystalline copper. Due to the large simulation cell in the nanocrystalline copper, centro-symmetry, instead of common neighbor analysis, will be used during post-processing to distinguish the atoms at the grain boundaries from the atoms in the crystal interior.

5.3.1 Stacking Fault Energy

As discusses earlier, it is critical to demonstrate the accuracy of inter-atomic potential in modeling the deformation of FCC metals. This research repeats the calculation of the generalized stacking fault energy outlined by the work of Zimmerman et al [183] with the copper EAM interatomic potential. The computed result is then compared with the results for stacking fault energies reported by other researchers to validate the accuracy of the potential used.

A simulation cell with orientation [1 $\bar{1}$ 2], [1 1 1] and [1 $\bar{1}$ 0] in the x, y and z direction respectively has been constructed for this run. The size of the simulation cell is 10x40x10 lattice units on each side. Furthermore, the simulation cell is then sectioned into two blocks by cutting along the {1 1 1} plane as shown in Figure 5.9.

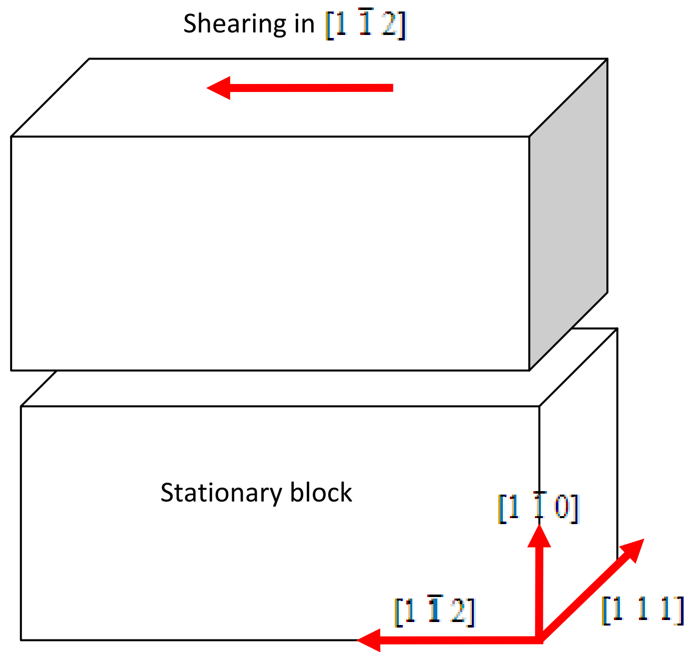

Figure 5.9: Schematic of the model used to reproduced the generalized stacking fault curve

In order to eliminate the influence of the free surface in the calculation of the stacking fault energy, periodic boundary conditions are enforced in the x and y direction. A uniform shear motion is applied to the top block in the simulation whereas the bottom block is kept stationary. The equation of motion for NVE ensemble is then used to perform the shear calculation at 0 K. The generalized stacking fault energy is then computed by monitoring the energy of each atom near the area where the fault is created. The value of unstable stacking fault energy γ_{usf} and the

stacking fault energy γ_{sf} is calculated as the energy difference between the deformed and undeformed state at the critical point along the generalized stacking fault curve.

Figure 5.10 shows the generalized stacking fault curve of copper from three EAM potential from the literature.

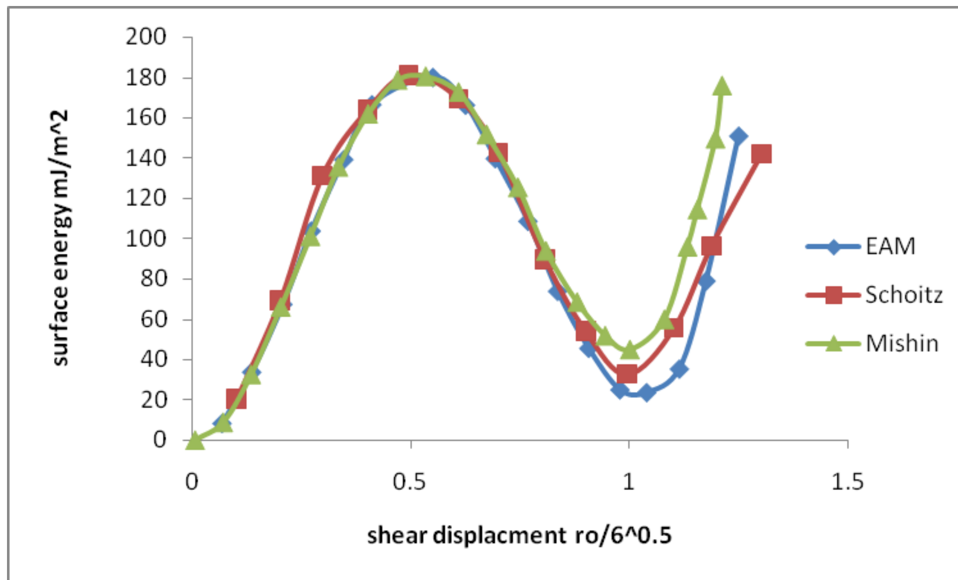

Figure 5.10: Generalized stacking fault curve of copper from three EAM potential from the literature review[116, 167]

All three inter-atomic potentials show very similar profiles for the generalized stacking fault energy. The stacking fault energy and unstable stacking fault energy computed by the copper EAM potentials used in this project are 20mJ/m^2 and 180mJ/m^2 respectively which compare very well with the data in Figure 5.9. Although the EAM potentials used in this research are not as close to the value of 45mJ/m^2 [205] predicted by both experimental result and Mishin et al [206] for copper, this EAM potential performed pretty well as compared to the other inter-atomic potentials. Furthermore, the stable and unstable stacking fault energy calculations are consistent with the tight-binding calculation of 162mJ/m^2 and 18.2mJ/m^2 respectively. Hence,

the EAM potential used in this research is adequate for accurately modeling the deformation mechanism of copper.

5.3.2 Simulation Model

Since grain boundary structure on the atomic level of the grain boundary plays a major role in the deformation process, it will be critical to model realistic grain boundaries and grain structure so as to draw realistic conclusions from these simulation experiments. Since the grains of ECAE copper become more equi-axial and randomly orientated as the number of passes increases [37], the grain in the simulation model constructed in this research should be equi-axial and randomly orientated. For this research, fully dense nanocrystalline copper is constructed using Voronoi Tessellation methodology describes in Section 3.4.1. The initial sample is shown in Figure 5.11.

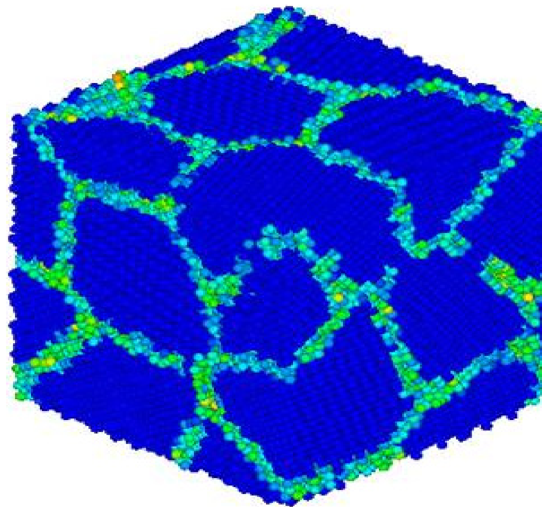

Figure 5.11: Initial nanocrystalline microstructure of copper

The size of the simulation cell for nanocrystalline copper with a 20nm grain size is measured to be 25nm x 25nm x 25nm whereas size of the simulation cells for nanocrystalline copper with a grain size of 5nm, 10nm and 15nm are 20nm x 20nm x 20nm. The larger simulation size of nanocrystalline copper with an average grain size of 20nm is needed in order to accommodate the larger grain. Again, 3D periodic boundary condition is enforced in order to model bulk nanocrystalline copper. In order to generate a realistic initial microstructure with no residual stresses, the simulation cell is first subjected to an energy minimization routine using a Polak-Ribière nonlinear conjugate gradient routine at a temperature of 0 K before it is subjected to NPT equilibration at ambient condition (300K at atmospheric pressure) for 50ps. As mentioned, centro-symmetry is used during post-processing to distinguish the atoms at the grain boundaries from the atoms in the crystal interior.

In order to validate the microstructure used in this research, the average grain size and grain size distribution is computed and compared to the characteristics of the actual microstructures described in the literature [37]. For this benchmark, the nanocrystalline copper with a grain size of 5nm grain is used. The volume of each grain can be computed by product of the number of unit cells needed to make up each grain and the volume of each unit cells. Using the computed volume, the grain size can be then computed by assuming these grains to be spherical in shape and suing the formula to compute a volume of a sphere. Table 3 summarizes the number of grains and the average grain size for each model.

Table 5.2 Summary of the number of grains and the average grain size for each model

Number of grains	Grain size Computed (nm)	Grain size (nm)
4	17.6	20.0
4	13.0	15.0
17	9.3	10.0
123	4.96	5

Even though the error increases as the number of grains in each model decrease, the largest difference is only 13% for 15nm. Hence, Voronoi methodology is able to model the average grain size accurately.

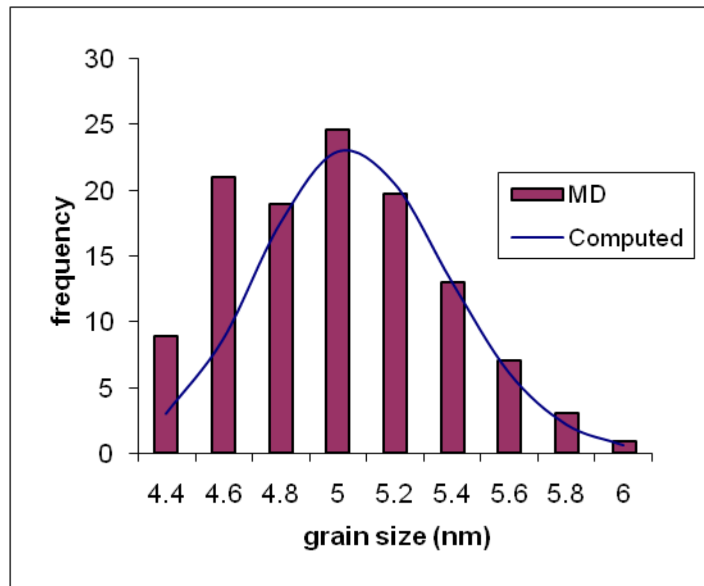

Figure 5.12: Grain size distribution for nanocrystalline copper with 5 nm grain size

Even though Figure 5.12 shows only the grain size distribution for nanocrystalline copper with a 5nm grain size constructed using the Voronoi Tessellation methodology, it is representative of the other microstructures constructed using this methods, Since the grain size distribution of copper has been shown experimentally to follows a log-normal distribution, Figure 5.12 also compared the estimated grain size distribution from this research with the theoretical log-normal distribution [207, 208]

$$f(x: \mu, \sigma) = \frac{1}{x\sigma\sqrt{2\pi}} e^{-\frac{(\ln(x)-\mu)^2}{2\sigma^2}} \tag{5.4}$$

The parameter x in equation 5.4 is the equivalent grain diameter, σ is the natural logarithm of the standard deviation and μ is natural logarithm of the mean of the log-normal distribution. Since Figure 5.12 shows that the grain size distribution follows a log-normal distribution with the value of μ and σ computed to be 3.92 and 0.065, the microstructure created in this study appears to represent a realistic grain size distribution. The expected grain size predicted by the log-normal distribution is 5.07nm. Hence, the Voronoi Tessellation methodology employed in this research can be used to produce microstructure with log-normal distribution and the required average grain size.

As discussed earlier, the texture of ECAE copper is that of a random, single-phase poly-crystal, so there is a need to ensure the randomness of the grain orientation. Unlike the one-dimensional orientations (only [001] tilt boundaries) where the grain disorientation density function is uniform, the disorientation angle of the 3D crystallography is a result of the convolution of two random three-dimensional variables where it is easiest to achieve

misorientations near some mean angles. Furthermore, by considering the cubic symmetry of the orientation space, it has been found that Mackenzie distribution function $p(\psi)$ described in equation 5.5 [209] could be used to quantify the randomness of the grain disorientation angle. Thus, grain disorientations distribution of the initial structures created in this research can now be benchmarked with the Mackenzie distribution function so as to determine the texture of our microstructure.

$$p(\psi) = \frac{2}{15}\left[\left\{3\left(\sqrt{2}-1\right)+\frac{4}{\sqrt{3}}\right\} sin\psi - 6(1-cos\psi)\right]$$

$$-\frac{8}{5\pi}\left[2\left(\sqrt{2}-1\right)cos^{-1}\left(Xcot\frac{\psi}{2}\right)+\frac{1}{\sqrt{3}}cos^{-1}\left(Ycot\frac{\psi}{2}\right)sin\psi\right.$$

$$+\frac{8}{5\pi}\left\{2cos^{-1}\left\{\frac{\left(\sqrt{2}+1\right)X}{\sqrt{2}}\right\}+cos^{-1}\left\{\frac{\left(\sqrt{2}+1\right)Y}{\sqrt{2}}\right\}\right\}(1-cos\psi) \qquad (5.5)$$

In equation 5.5, ψ is the disorientation function and the parameter X and Y are given by equation 5.6 and equation 5.7.

$$X = \frac{\left(\sqrt{2}-1\right)}{\left[1-\left(\sqrt{2}-1\right)^2 cot^2\frac{\psi}{2}\right]^2} \qquad (5.6)$$

$$Y = \frac{\left(\sqrt{2}-1\right)^2}{\left[3-cot^2\frac{\psi}{2}\right]^{1.5}} \qquad (5.7)$$

Figure 5.13 compares grain disorientation distribution of the initial structures created in this study with the Mackenzie distribution function. The Mackenzie distribution will only

describe a randomly distributed texture if the mean $\bar{\psi}$, the standard deviation σ and the mean ψ_{med} has the following values:-

$\bar{\psi} = 40.736°$

$\sigma = 11.315°$

$\psi_{med} = 42.341°$

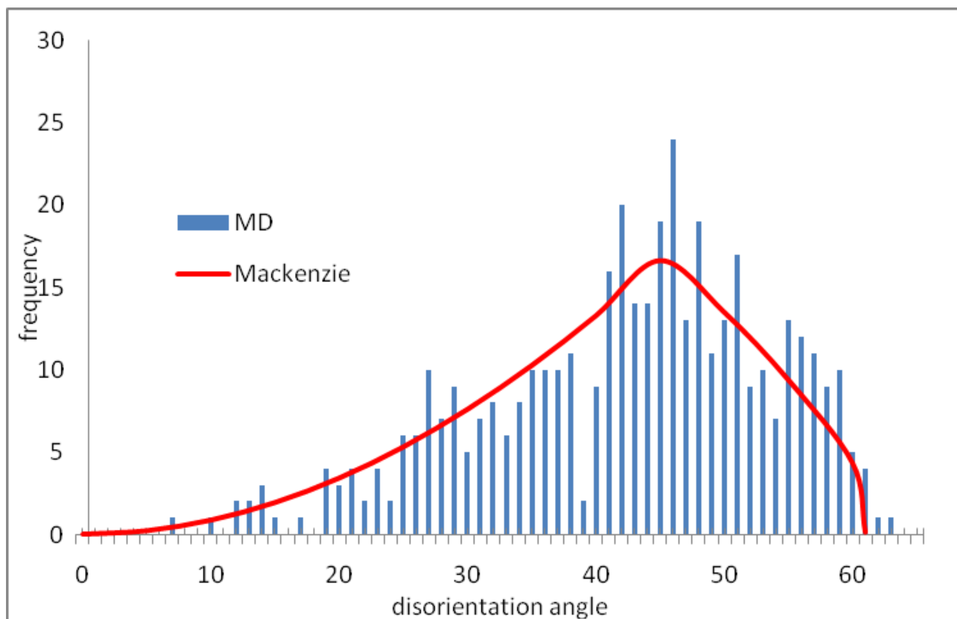

Figure 5.13: Comparison of the grain disorientation density function of the microstructure created in this research with the Mackenzie distribution function.

Figure 5.13 shows that the computed values of the mean $\bar{\psi}$, the standard deviation σ and the mean ψ_{med} for our microstructure is as following

$$\bar{\psi} = 40.32^{\circ}$$

$$\sigma = 10.93^{\circ}$$

$$\psi_{med} = 42^{\circ}$$

Hence, the Voronoi Tessellation methodology employed in this study can be used to model randomly textured, single-phase poly-crystalline copper.

5.3.3 Monotonic Loading

5.3.3.1 Mechanical Properties and Deformation Mechanism

In order to investigate the relationship between grain size and the room temperature stress-strain constitutive behavior, a matrix of atomistic simulations were performed on nanocrystalline copper with grain sizes of 5nm, 10nm, 15nm and 20nm grain size. After the construction of the nanocrystalline structure using the model discussed earlier, samples were uniaxially strained at a constant strain rate of 10^9/s at 300 K using the equation of motion for NEPT ensemble. During deformation, stress-strain are calculated using equation 3.30 and equation 4.12, respectively. The resulting stress-strain curves from these simulations are shown in Figure 5.14.

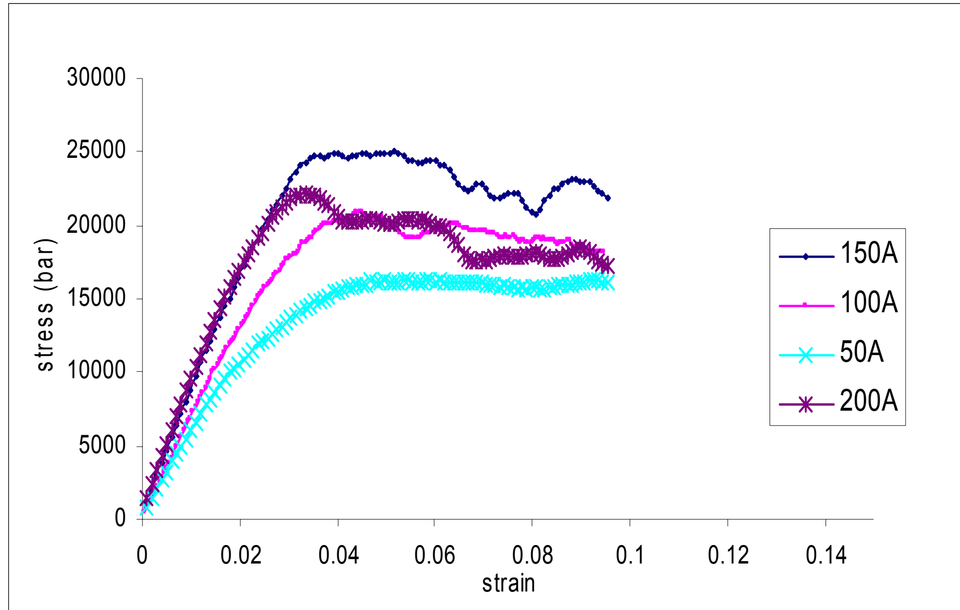

Figure 5.14: Stress strain constitutive relationship as a function of grain size

5.3.3.1.1 Young's Modulus

Although the relationship of the Young's modulus with respect to the grain size have been discussed in section 4.3.1, important observation on the effect of grain size on the modulus will be repeated here for completeness.

Due to the higher volume fraction of grain boundary atoms for smaller grain size, Young's modulus dependency on the grain size can be explained using and the rules of mixture as previously shown in Figures 4.9 and 4.10.

5.3.3.1.2 Yield Strength

Up to certain critical grain size, experimental and computational results have consistently shown that the strength of nanocrystalline metals and alloys increases with decreasing grain size.

However, the actual mechanisms responsible for the observed behavior of nanocrystalline materials were not well understood.

In order to fully understand the relationship between grain size and yield strength, the yield strength of each grain size is computed and plotted in Figure 5.15. The experimental value of Bansal et al is also plotted in Figure 5.15 so as to benchmark against the simulation results.

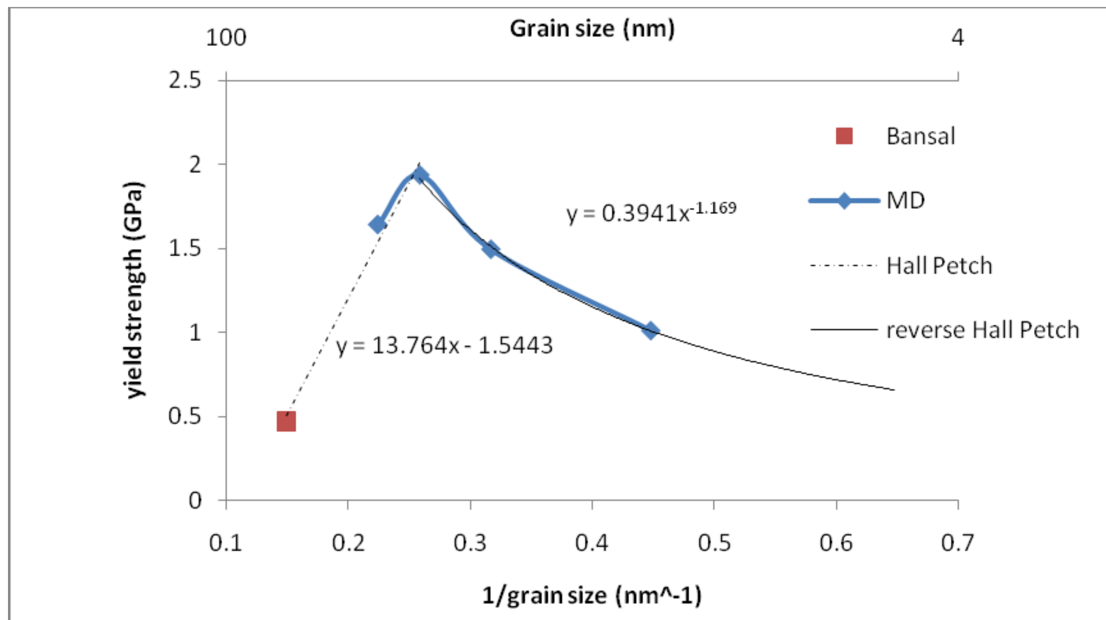

Figure 5.15: The relationship between grain size and yield strength.

Figure 5.15 shows that the computed yield stress is higher than the yield stress obtained by Bansal et al [1] experimentally. This is firstly due to the short time scale in molecular dynamics simulations where there is a need to deform the specimen at a very high strain rate. Furthermore, mirco-voids and porosity normally found in experimental specimens are known to decrease the strength of materials. Since the nanocrystalline copper in molecular simulation is free of these defects, it is expected for the computed yield stress to be higher than the one obtained

experimentally. It should be noted though, that the experimental results cited above were obtained on ECAE processed material that is known to be defect-free. Another reason for the discrepancy could be related to the presence of small angle grain boundaries in real materials that are not as effective in enhancing strength. The simulations do not include such boundaries. A yet another reason can be the structure of the actual grain boundaries that can vary between the simulations from those actually present in the real materials. Nevertheless, Figure 5.15 shows that for grain size larger than 15nm, including Bansal et al experimental data, the strength of nanocrystalline copper follows the Hall-Petch relationship where the yield strength is an inverse function of the square root of its grain size. However, the yield strength reaches a maximum value of about 1.93GPa at a grain size of 15nm and then on the yield stress decreases for grain sizes below 15 nm. This deviation from Hall-Petch effect is known as the reverse Hall-Petch effect, and has also been observed in experiments. Unlike most of the experimental observations of a reverse Hall-Petch effect in nanocrystalline metals where the decreases in strength have been found to be a result of poor sample quality, the simulation model in this research is free from defects and hence the observed reverse Hall Petch effect in this research is solely due to the reduction of the grain size. Thus, there is indeed an existence of a 'strongest grain size' at about 15nm where nanocrystalline copper has the highest resistance to plastic deformation. Further, the reverse Hall- Petch relationship for nanocrystalline copper is characterized by the following equation:

$$\sigma_y = 0.39d^{0.68} \tag{5.8}$$

In equation 5.8, σ_y is the yield strength and *d* is the grain size in nanometers. Lastly, by extrapolating Figure 5.15 to a grain size of 0nm, this figure shows that the yield strength of amorphous copper has been found to be about 0.8GPa.

5.3.3.1.3 Deformation Mechanisms

The actual mechanisms responsible for the observed relationship between grain size and yield strength of nanocrystalline materials discussed in the previous sections are not well established. Dislocation activities were quoted as the primary deformation mode for materials up to certain critical grain size. However, below this critical grain size, the mechanism is not very well understood and many different models have been proposed to explain the reverse Hall-Petch effect such as grain boundary sliding, grain rotation and Coble creep. There is a need to investigate the deformation mechanisms in these regions. Since copper with grain sizes of 10nm, 15nm and 20nm include the regions of the inverse Hall- Petch region, the region with the strongest strength and the Hall-Petch region, the dislocation activities, grain boundary sliding and migration and the grain boundary rotations are investigated using the simulations conducted for these grain sizes.

As discussed above, the dislocation activities were quoted as one of the primary deformation modes for nanocrystalline materials. Hence, the dislocation activities in each region are investigated first. Unlike the common neighbor analysis in single crystal analysis, centro-symmetry parameters only keep track of the symmetry of the surrounding atoms in FCC materials. Hence, in order to track the evolution of dislocation activity, an approximate method of counting the number of disordered atoms is used as an indicator of dislocation density

evolution. Figure 5.16 shows the volume fraction of disordered atoms as nanocrystalline copper with different grain size is deformed.

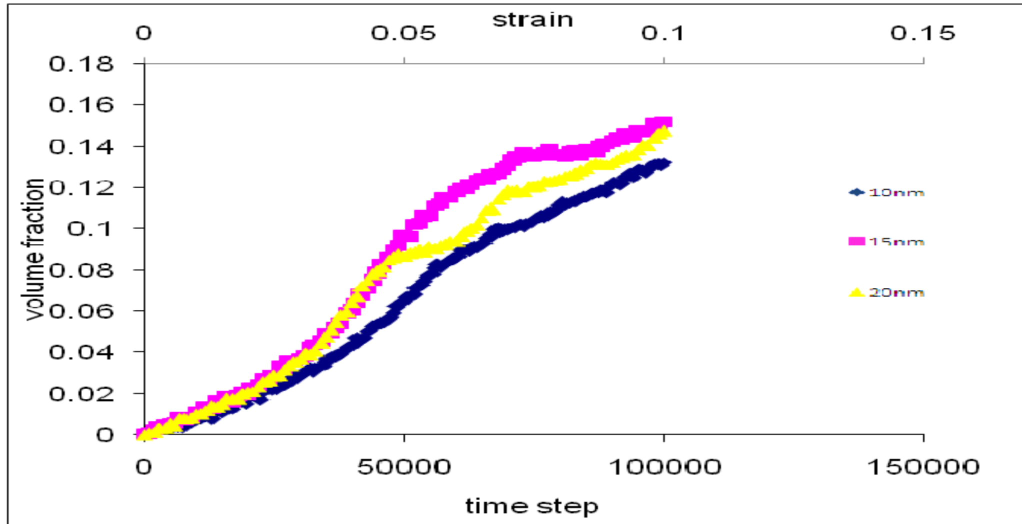

Figure 5.16: Evolution of the volume fraction of disorder atoms as nanocrystalline copper is deformed

The initial increase in the volume fraction of the disorder atoms shown in Figure 5.15 are mainly due to the distortion near the grain boundaries during straining. At about 3.0% to 3.5% strain for copper with 15nm and 20nm grain size, the nucleation of numerous dislocations is found to have occurred as indicated by the sudden increase in the volume fraction of disorder atoms. Figure 5.16 also shows that the nanocrystalline copper with a grain size of 15nm had the largest volume fraction of disorder atoms and hence dislocation activity. This is then followed by copper with 20nm grain size and 10 nm grain sizes. Since the yield strength shown in Figure 5.15 follows the same trend, this may indicate that increase in strength in nanocrystalline copper for the three regions is due to the increases in the dislocation activities.

Since grain boundary sliding and grain rotation were quoted as one of the primary deformation mode for nanocrystalline materials, the grain rotation of each region is investigated in this research as shown in Figure 5.17.

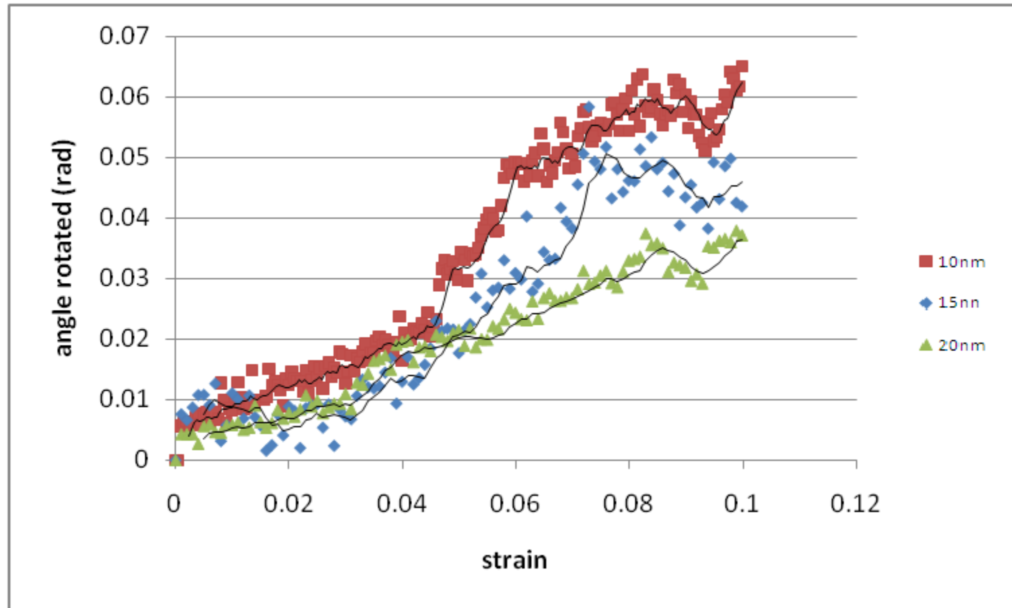

Figure 5.17: Evolution of grain rotation as nanocrystalline copper is deformed

Figure 5.17 shows that grain boundary sliding gradually sets in as the stress builds up for copper with 10nm and 15nm grain size. There is significantly less grain rotation for samples with 20nm grain size, as expected. This is mainly because as grain size increases, it becomes increasingly more difficult for the grains to rotate since grain rotation requires an accommodation mechanism [210] to ensure continuous deformability while avoiding micro-cracking.

Figure 5.17 also shows a sudden increase of the magnitude of grain rotation at a strain of about 4.5% to 5% for both 10nm and 15nm copper. Since Figure 5.15 shows that the softening of

nanocrystalline copper occurs at 4% strain, it appears that resulting stress buildup is relieved through grain rotation facilitated by sliding and dislocation activity.

Since room temperature strain rate sensitivity *m*, computed using equation 5.1, will also provide some insight into the deformation mechanism in nanocrystalline copper, the relationship between strain rate sensitivity and grain size is also investigated in this research. Figure 5.18 and Figure 5.19 show the room temperature strain rate sensitivity m as a function of grain size for nanocrystalline copper. Furthermore, the experimental results from the work of Wang et al [203]and the single crystal calculation are also included in Figure 5.18 for comparison purposes.

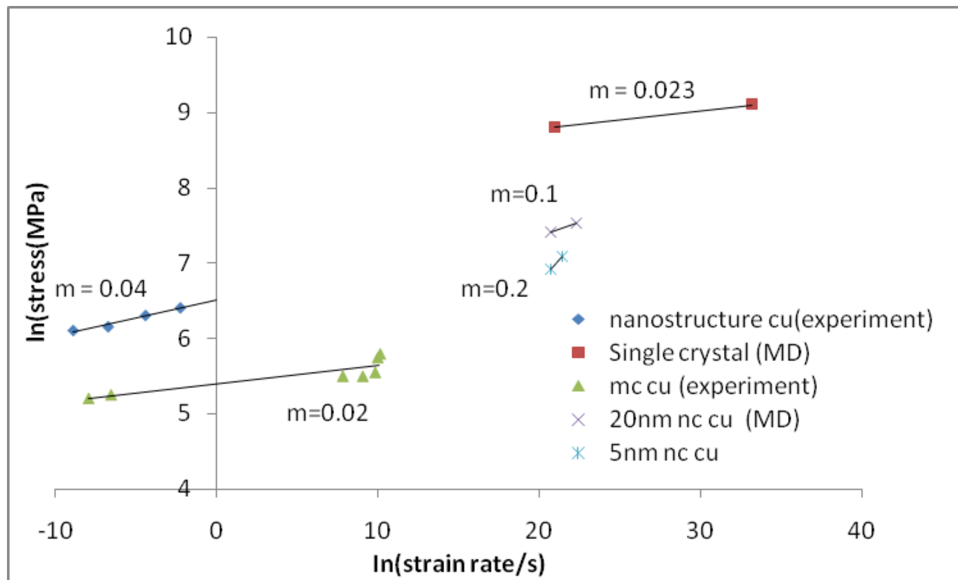

Figure 5.18: Comparison of strain rate sensitivities with experimental result and single crystal results

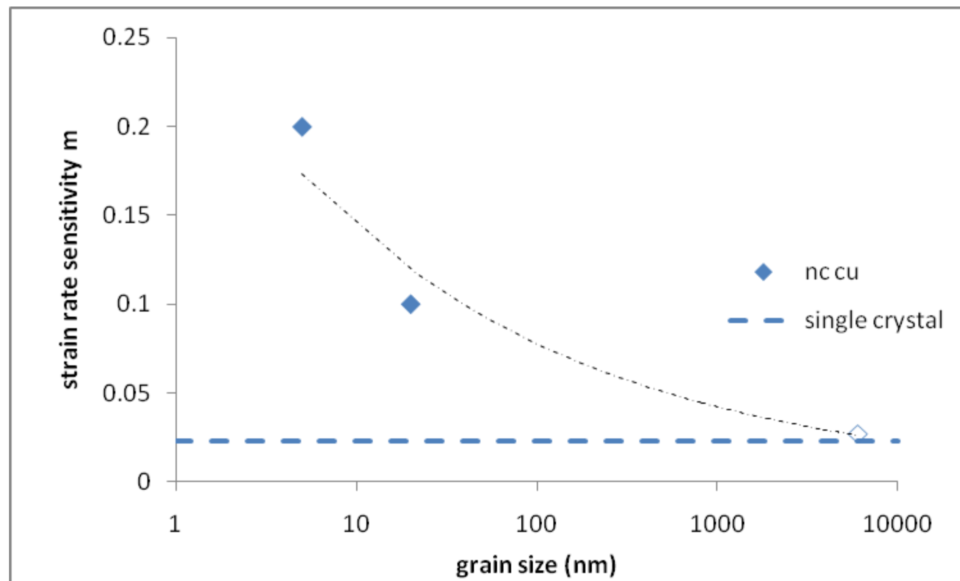

Figure 5.19: Summary of the room temperature strain rate sensitivity m as a function of grain size for nanocrystalline copper

Figures 5.18 and Figure 5.19 reveal very low strain rate sensitivities for single crystal copper with its value increasing as the grain size decrease. Furthermore, Figure 5.19 shows that the value of strain rate sensitivity finally takes-off when a grain size becomes smaller than 100nm. Since plastic deformation process controlled by grain boundary sliding has a strain rate sensitivity of 0.5 [80], this indicates that the rate controlling process shifts from the gliding dislocations cutting through forest dislocations at the larger grain size to the interaction between dislocations and the grain boundaries, and ultimately to extensive grain boundary sliding enabling rotation , as the grain size decreases further.

It can be concluded from the above discussion that the dislocation activity is the primary deformation mechanism for nanocrystalline copper in the Hall-Petch region with some or minimal grain rotation. The simulation results in this study also indicate that a higher amount of

grain rotation occurs and it becomes an increasingly important deformation mechanism with decreasing grain size and ultimately leads to the region of inverse Hall-Petch region. Hence, this shows that there is a competition between the dislocation activity and grain boundary sliding as the main deformation mode.

5.3.4 Cyclic Loading

As discussed earlier, nanocrystalline copper has a high potential of being used as the next generation interconnect for electronic packaging. However, their fatigue properties are not well documented and no model has been established to predict/characterize these nano materials in interconnection application. Since it is important to predict the performance of nanocrystalline copper during service, this section will discuss the results on this study that has attempted to model fatigue properties of the nanocrystalline copper. Since the results in Chapter 4 indicate that the crack initiation life is the main factor in determining the fatigue life of interconnects, crack growth will be not simulated in this research.

A matrix of atomistic simulation on nanocrystalline copper with a grain size of 5nm, 10nm, 15nm grain size and 20nm grain size have been constructed to investigate the fatigue behavior of nanocrystalline copper under cyclic loading. These nanocrystalline coppers are uniaxially strained with a constant strain rate of strain rate of 10^9/s at 300 K using the equation of motion for NEPT ensemble As in the study on single crystal copper, R-ratio is maintained at zero throughout cyclic loading

5.3.4.1 Failure Criterion

Figure 5.20 investigates the fatigue life of nanocrystalline copper that is subjected to 10% total strain rate. It shows that copper with 5nm grain size had the longest life before it loses about 50% of its load carrying capability. This follows by 10nm, 15nm and 20nm nanocrystalline copper. Comparing the fatigue life and the volume fraction of disorder atoms of nanocrystalline copper with average grain sizes of 10nm, 15nm and 20nm at 10% strain (Figure 5.16) shows that both results exhibited the same trends: 10nm and 15nm nanocrystalline copper having about the same volume fraction of disorder atoms and fatigue life whereas 20nm nanocrystalline copper having less dislocation activity and a shorter fatigue life. Hence, this may indicate that fatigue life is dependent on the dislocation activity that is dependent on the grain size.

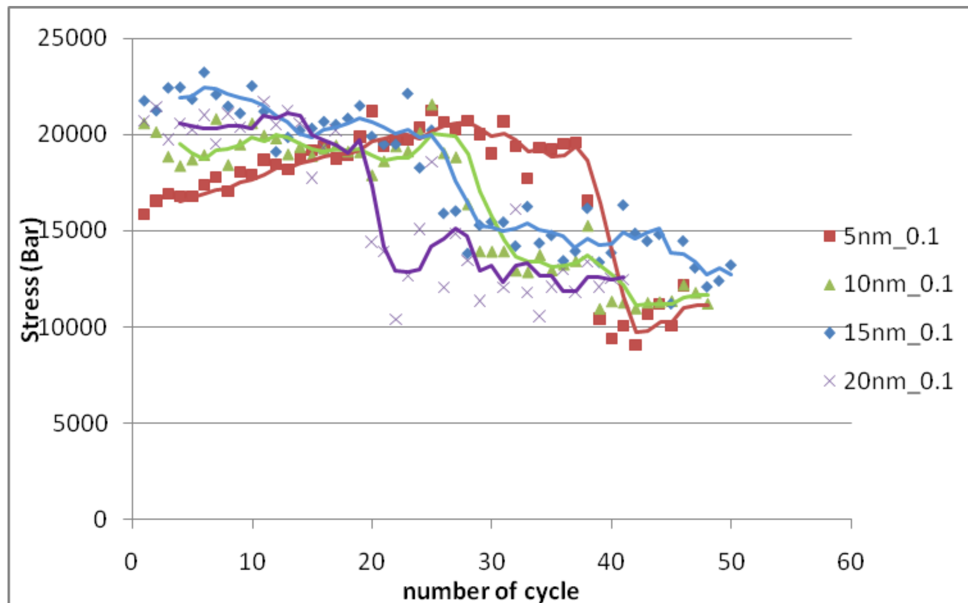

Figure 5.20: Fatigue life for different grain sizes

However, Figure 5.20 also indicates that the nanocrystalline copper loses its load carrying capability quickly at about 20-40 cycles depending on the grain size. The degradation of the nanocrystalline copper stops almost as quickly. This indicates that the loss in load carrying capability of these nanocrystalline copper is not due to the formation of micro-voids. This type of load profile is more consistent with stress relief during annealing as shown in Figure 5.21[11]. Hence, this provides the first evidence that the loss in load could be due to grain growth. Comparing the microstructure of the copper nanocrystalline copper at the 5th and 30th cycles in Figure 5.22 confirms that grains have indeed grown.

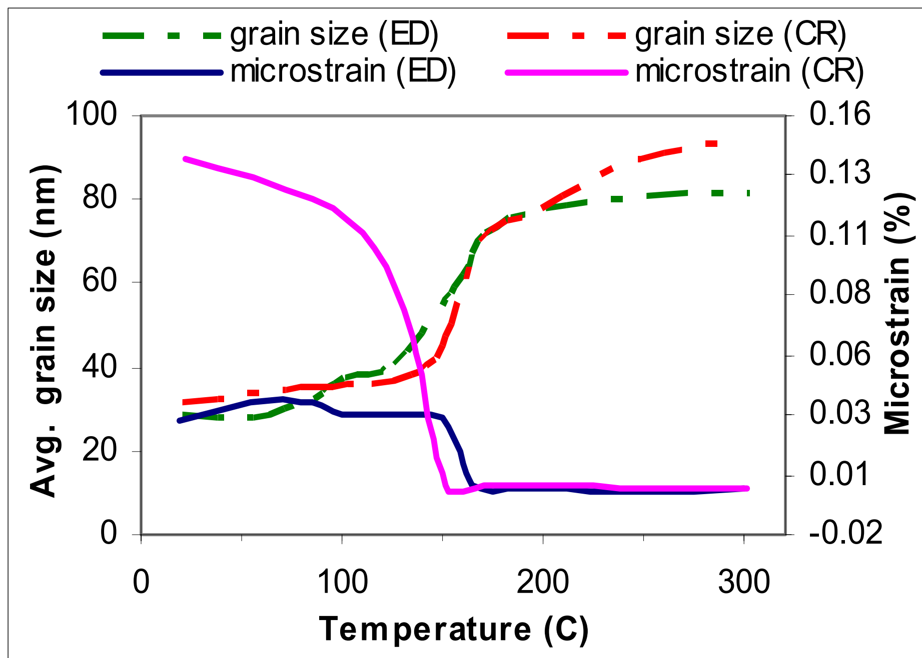

Figure 5.21: Evolution of the microstructure during stress relief

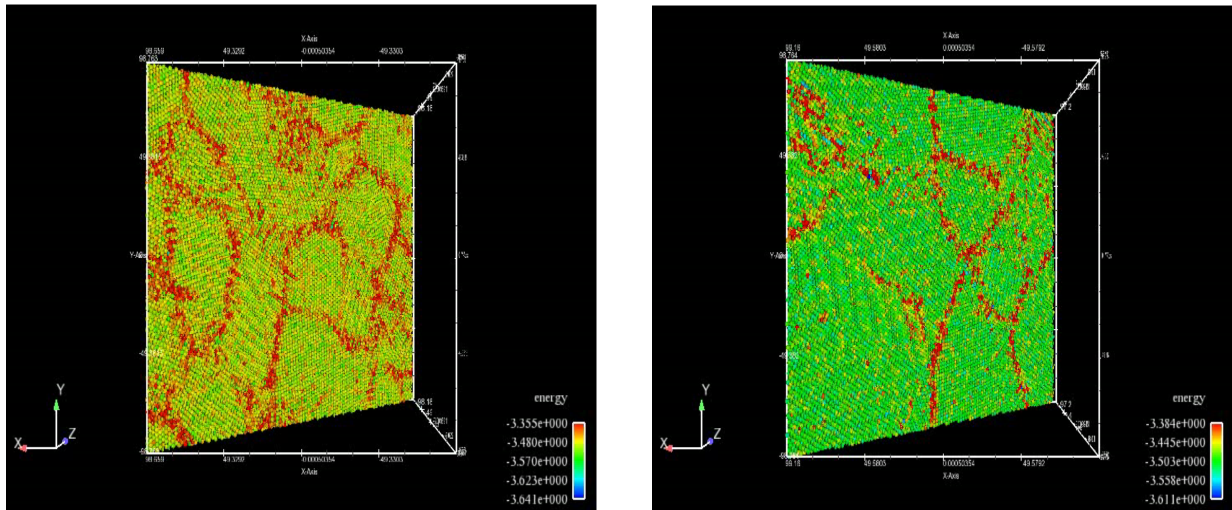

Figure 5.22: Evolution of the microstructure at the 5th cycles and 30th cycle

In order to investigate whether the observed grain growth in Figure 5.21 and Figure 5.22 is the main cause for the loss in the load in nanocrystalline copper, this research compares the evolution of the peak stress and the evolution of microstructure for copper during fatigue cycling with a total strain rate of 10% and 1% as shown in Figure 5.23 and Figure 5.24 respectively. Since it will be important to identify the mechanism for observed grain growth, Figure 5.23 and Figure 5.24 also include the cyclic results for 20nm nanocrystalline copper deformed at a temperature of 4K and 300K. The temperature of 4K is chosen as there will be minimal or almost zero temperature driven grain growth at this temperature. Furthermore, the evolution of microstructure for undeformed nanocrystalline copper is also included in these two figures to ensure that there is insignificant grain growth in the absence of any loads.

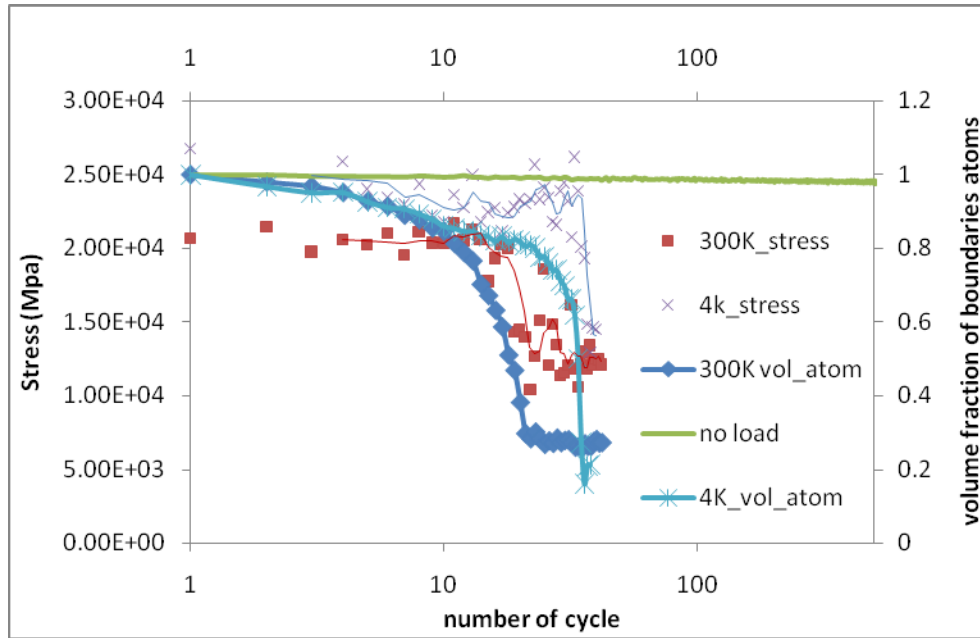

Figure 5.23: Comparisons of the degradation of peak stress with the evolution of microstructure for copper with 20nm grain size under 10% strain range.

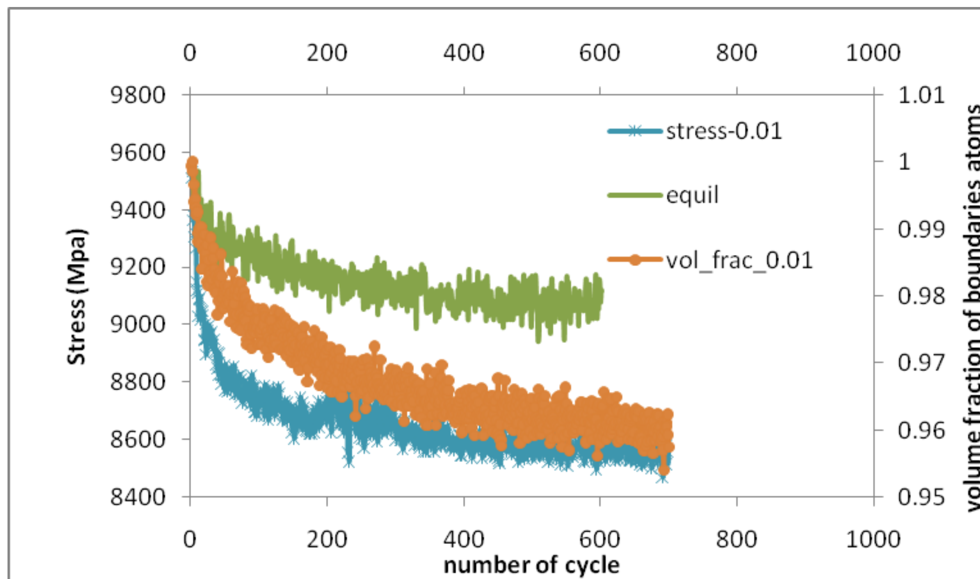

Figure 5.24: Comparisons of the degradation of peak stress with the evolution of microstructure for copper with 20nm grain size under 1% strain range.

Figure 5.23 and Figure 5.24 show that the degradation of load and the decrease in the volume fraction of grain boundary atoms have similar trends. Furthermore, the degradation of load occurs at about the same cycle as the rapid decreases in the volume fraction of grain boundary atoms, Hence, Figure 5.23 and Figure 5.24 shows that the loss in the load carrying capability is indeed due to grain growth. Furthermore, since no grain growth is detected for undeformed nanocrystalline copper whereas significant grain growth is detected for nanocrystalline copper at 4K, the observed grain growth and hence the degradation of the nanocrystalline copper is identified to be due to stress assisted grain coarsening.

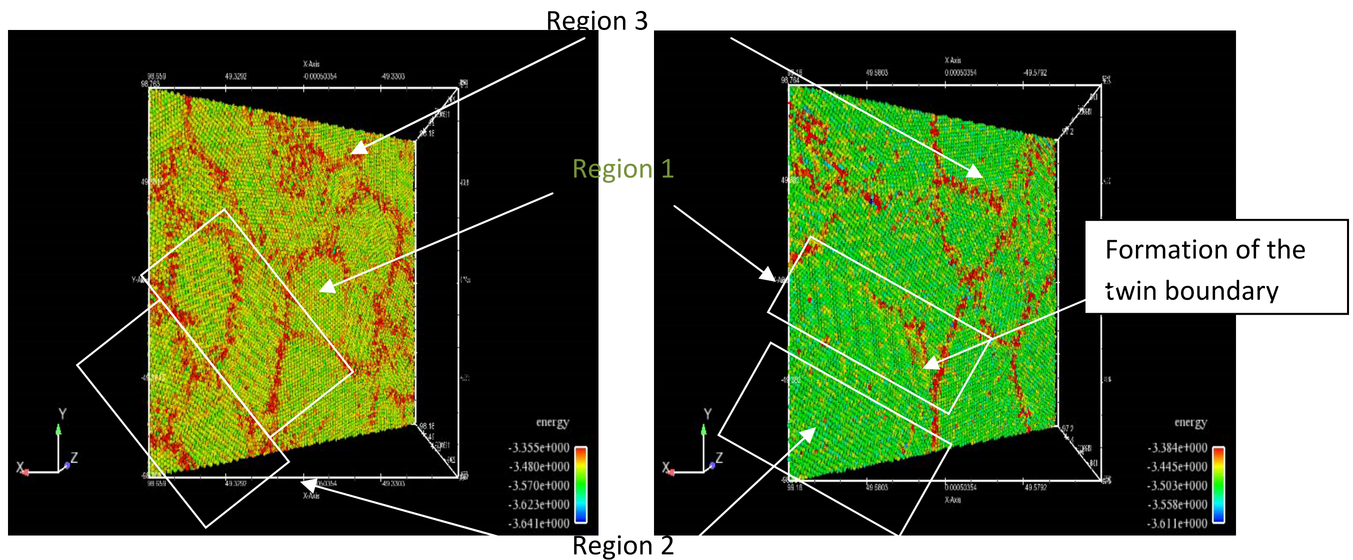

Figure 5.25: Evolution of the microstructure at the 5th cycles and 30th cycle

The mechanisms for the stress driven grain growth can be identified by comparing the microstructure at the 5th and 30th cycle. Figure 5.25 shows that the two grains in region 1 and

region 2 in the 5th cycle, that have coalescence into a single grain by the 30th cycle. Furthermore, the presence of the twin boundary in between the two regions strongly suggests the coalescence of these grains in these two regions is due to grain rotation instead of through grain boundary migration. Furthermore, the evidence for grain growth due to the migration of the grain boundaries can be observed in region 3 where the grain boundary in region 3 is seen to have shifted. Hence, the two potential mechanisms for stress driven grain growth is identified to be grain rotation and migration of the grain boundaries.

Figure 5.26 tracks the magnitude of the grain rotation in one of the grains as the simulation time increases. Even though the grain rotation decreases during unloading cycle, Figure 5.26 still clearly shows that the angle of grain rotation increases steadily with cycles and it took off at around 19th cycle. This corresponds to about the same cycle at which the significant load drop occurs as shown in Figure 5.15. Furthermore, the gradual increase in grain rotation angle ceases immediately after the grain has coalesced and this is due to the inability for the grain to rotate once it has coalesced into a much bigger grain. Hence, it may be concluded that the grain rotation is the main mechanism for the stress assisted grain growth at smaller grain sizes whereas grain migration is the main mechanisms for the growth of larger grains.

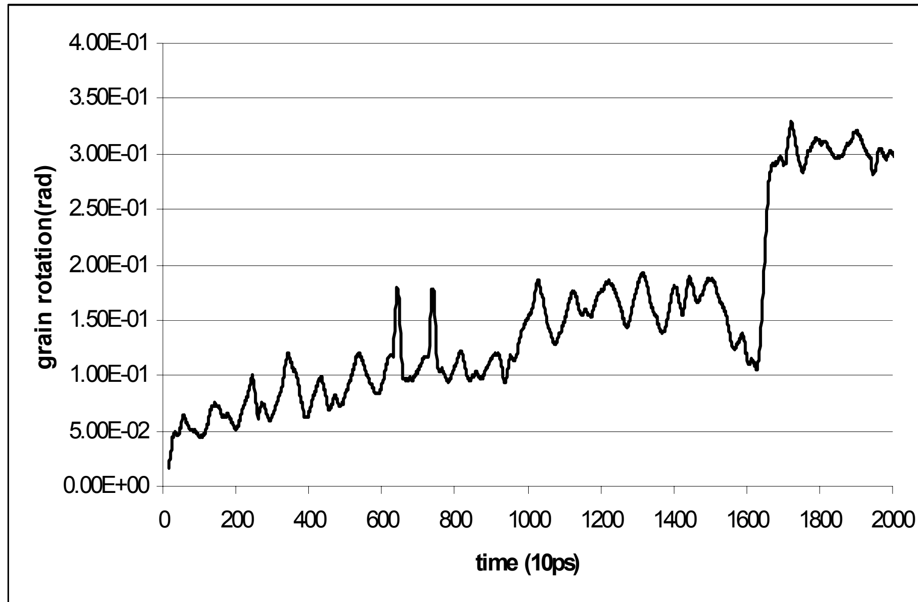

Figure 5.26: Evolution of grain rotation as the simulation times increases

In conclusion, this research has shown that stress induced grain coarsening is the main criterion for the nanocrystalline copper to lose their mechanical performance during cyclic loading for smaller grains. However, the simulation results have also shown that grain growth during fatigue loading will be assisted by other mechanisms such as dislocation activities and grain boundary migration.

5.3.4.1 Fatigue Modeling

As discussed in the earlier section, the loss in load during cyclic loading is identified to be stress assisted grain growth due to grain rotation and coalescence. Since the grain rotation is a function of both the strain range and temperature, a matrix of simulation experiments are

repeated with different temperature and strain range as shown in Figure 5.27 and Figure 5.28 in order to develop a model for predicting the fatigue life of nanostructured chip to package interconnects.

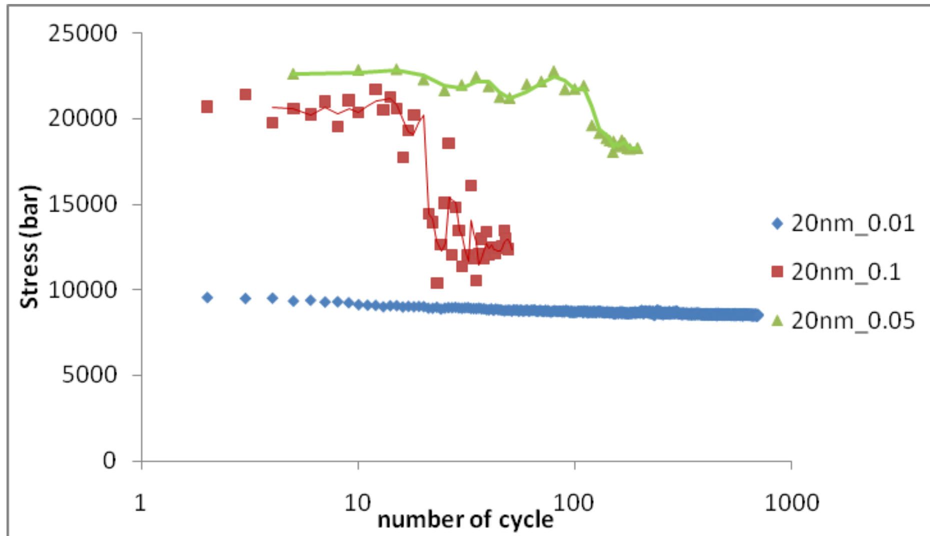

Figure 5.27: Fatigue life as a function of total strain range

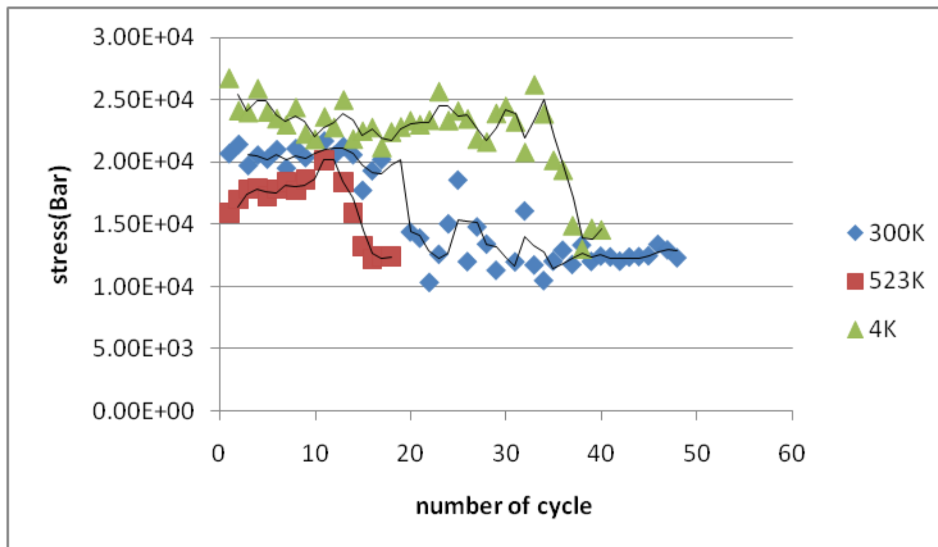

Figure 5.28: Fatigue life as a function of temperature

Using Figure 5.27 and Figure 5.28 and defining the failure of the nanocrystalline copper as the onset of rapid grain growth, the fatigue life as a function of grain size, temperature and total strain range is computed as shown in Figure 5.29 and Figure 5.30 respectively.

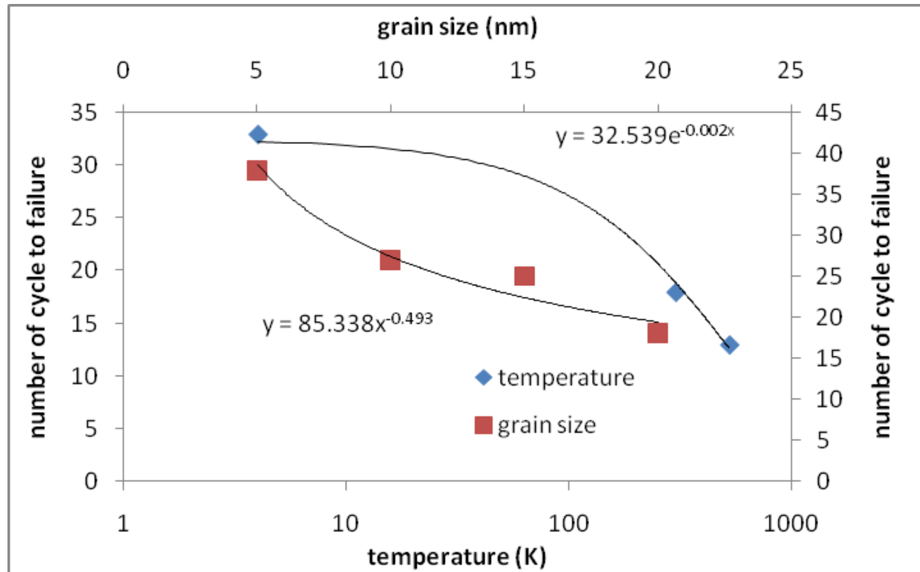

Figure 5.29: Summary of the fatigue life as a function of grain size and temperature

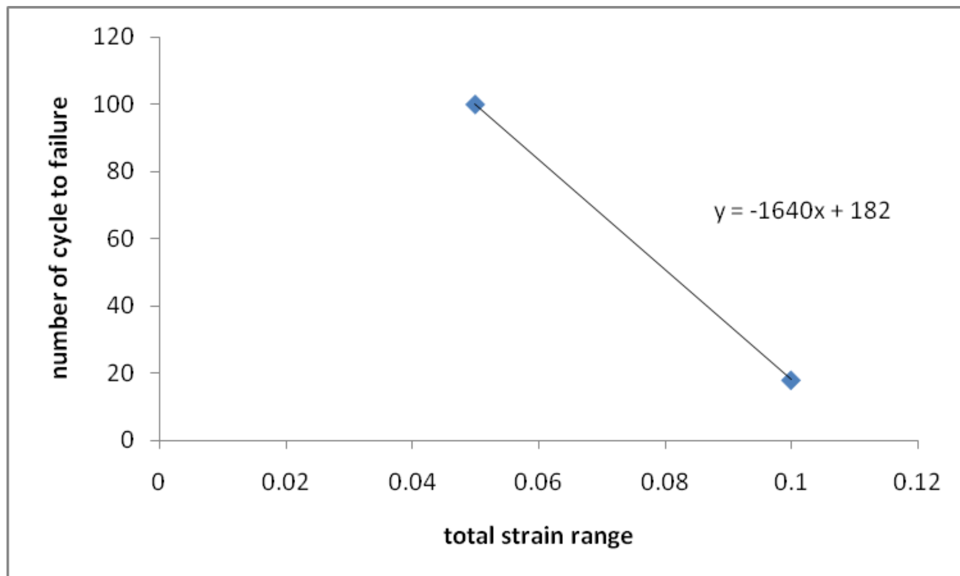

Figure 5.30: Summary of the fatigue life as a function of total strain range

As discussed in the earlier section, the loss in load carrying capability during cyclic loading is identified to be stress assisted grain growth due to grain rotation and coalescence. Since the mechanism for Coble creep is also identified to be grain rotation and grain boundary sliding, they should have the same stress dependency. Furthermore, due to the increasing difficulty for the grains to grow at low temperature, an exponential relationship is used to characterize the temperature dependency. Hence the proposed fatigue model for this research is

$$N = \frac{Ae^{BT}}{D^{C}} \Delta\varepsilon \tag{5.9}$$

In equation 5.9, *N* is the number of cycles to failure, *T* is the temperature in Kelvin, $\Delta\varepsilon$ is the total strain range and *D* is the grain size in nanometers. *A*, *B* and *C* are the fitting parameters. The value of parameters *B* and *C* is found to be 0.493 and -0.002 as shown in Figure 5.29. Using regression methods, the value of fitting parameter C is found to be 1466.75. Figure 5.31 compares the simulation results and the model results. Hence, the fatigue model proposed in this research seems to be able to predict the fatigue life quite accurately.

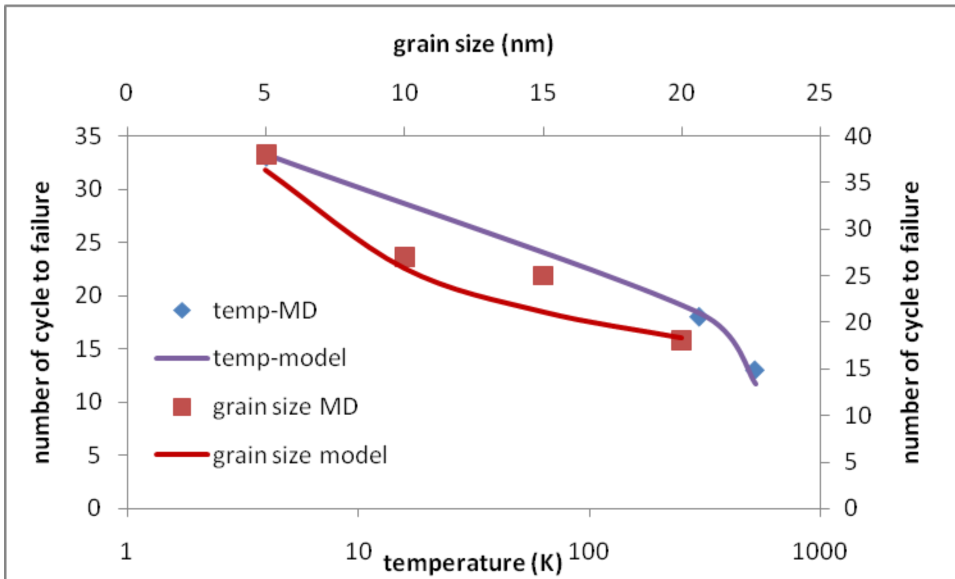

Figure 5.31: Comparison of molecular dynamics results and fatigue model results

5.4 Conclusion

In summary, this research reported in this chapter has validated the inter-atomic potential used in the study and has outlined the methodology for constructing a realistic microstructure for atomistic simulations. Furthermore, the materials response of single crystal under monotonic and cyclic loading has also been investigated: systematic atomistic simulations have been conducted on the crystallographic orientation and temperature effects on the deformation mechanisms in single crystal copper with <100> and <110> orientations. This research has also shown that the strain rate insensitivities of single crystals and proposed a solution for the dislocation nucleation stress for single crystal. Furthermore, by computing the activation volumes, the controlling mechanism for deformation in single crystal copper is identified to be the nucleation of dislocation. Similarly, the material response of single crystal under monotonic and cyclic loading has been investigated. The relationship between yield strength, grain size and the deformation

mechanisms in nanocrystalline copper during monotonic loading has been investigated. A loss in load bearing capability in fatigue loading has been identified to be due to stress assisted grain coarsening caused by grain rotation and coalescence. A fatigue model has been developed to predict the life of the nanostructured interconnects during service like conditions for interconnects.

CHAPTER 6

MOLECULAR SIMULATION OF GRAIN SIZE STABILIZATION DURING CYCLIC LOADING OF ANTIMONY DOPED NANOCRYSTALLINE COPPER

6.1 Introduction

As also mentioned earlier in Chapters 2 and 4, of all the known interconnect technologies, nanostructured interconnects such as nanocrystalline copper are the most promising for meeting the high mechanical and electrical performance requirements of next generation devices. However, the simulation results in Chapter 5 show that nanocrystalline copper will experience stress driven grain coarsening during the service life of interconnects and it causes loss in strength.

Recent molecular dynamics simulations by Millett et al. [14, 148, 149] have shown that temperature assisted grain growth can be eliminated with the presence of sufficient dopant atoms that tend to naturally segregate the grain boundary. However, there is no study yet on the retarding stress assisted grain growth and grain coarsening. Accordingly, the objective of this chapter is to develop an understanding of the stability of antimony doped nanocrystalline copper undergoing monotonic and cyclic loading.

6.2 Simulation Methodology

6.2.1 Inter-Atomic Potential

In this research, the copper EAM potential formulated by Folies et al [181] will be used to model nanocrystalline copper. As discussed in Chapter 5, this potential is able to model the generalized stacking fault curve quite accurately as compared to other copper EAM potentials. For modeling antimony, a new antimony potential based upon Lennard Jones potentials developed by Rajgarhia et al [176] has been used to model the antimony interaction. Hence, for antimony their values of σ=3.15Åm and ε=0.079 eV will be used throughout this research to model antimony deformation response. Furthermore, in order to model the interaction between anatomy and copper, the interspecies interactions is estimated [177] using Lorentz-Berthelot combination rules, as shown in equation 3.35 and 3.36

6.2.2 Simulation Model

For this research, fully dense nanocrystalline copper is first constructed using Voronoi Tessellation methodology as describes in Section 3.4.1. As discussed earlier, this methodology will produce randomly textured, single-phase poly-crystalline copper. Similar to the pure nanocrystalline copper study, the size of the simulation cell for nanocrystalline copper with a 20nm grain size is measured to be 25nm by 25nm by 25nm whereas size of the simulation cells for nanocrystalline copper with a grain size of 10nm is 20nm by 20nm by 20nm. Again, 3D periodic boundary condition is enforced in order to model bulk nanocrystalline copper.

Antimony atoms are then incorporated into the sample by randomly replacing a certain percentage of copper atoms at the grain boundaries as shown in Figure 6.1.

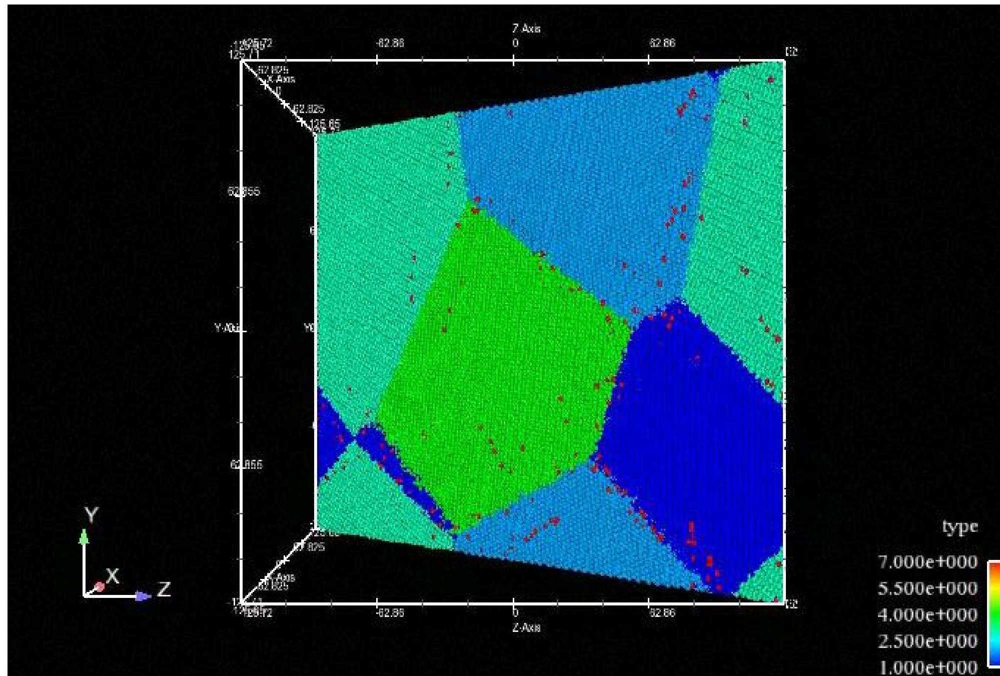

Figure 6.1: Simulation model for 1% antimony doped copper. The red dots are the antimony atoms

Similarly, these models are also subjected to an energy minimization routine at a temperature of 0 K before being subjected to NPT equilibration at 300K and atmospheric pressure for 50ps. These doped nanocrystalline copper sample is then uniaxially strained with a constant strain rate of 10^9/s using the equation of motion for NEPT ensemble. During the elongation, the stress-strain relationship is calculated using equation 3.30 and equation 4.12.

6.3 Monotonic Loading

Figure 6.2 and Figure 6.3 show the stress-strain constitutive relationship generated by molecular simulation of uniaxial tensile deformation of antimony doped copper with different average grain size of 10nm and 20nm, respectively. Firstly, Figure 6.2 shows a higher elastic limit for antimony doped copper as compared to the pure nanocrystalline copper. Furthermore, Figure 6.2 and Figure 6.3 clearly show that the strength of the nanocrystalline increases as the volume fraction of antimony increases from 0.5 atomic percentages to 1.0 atomic percentage whereas the elastic modulus remains independent to the volume fraction of antimony. This is consistent with the experimental work conducted by Yin et al [211, 212] in which it was shown that the strength of nanocrystalline nickel increases after it has been doped with either sulfur or boron.

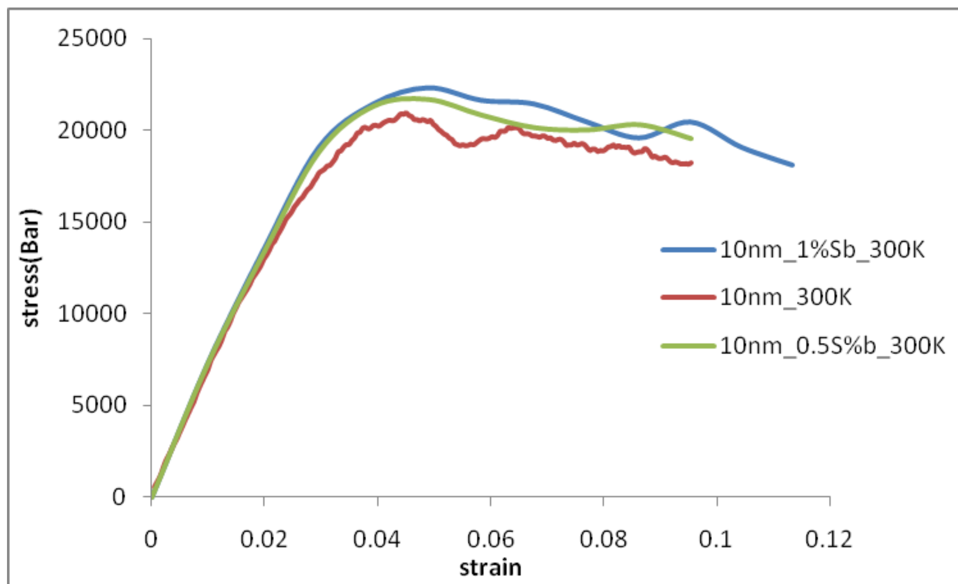

Figure 6.2: Stress strain constitutive relationship for antimony doped copper with a grain size of 10nm

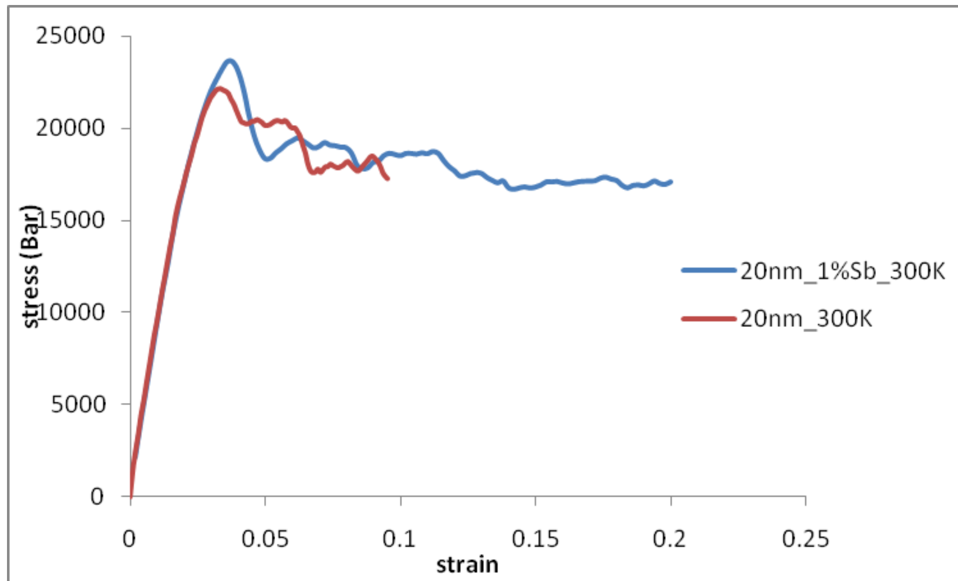

Figure 6.3: Stress strain constitutive relationship for antimony doped copper with a grain size of 20nm

In order to investigate the optimum volume fraction of antimony to be doped in nanocrystalline copper to achieve the highest strength, the relationship of the volume fraction of antimony and the maximum strength of the doped copper is plotted in Figure 6.4. Extrapolating the curve in Figure 6.4 shows that the maximum strength for doped copper with a grain size of 10nm increases gradually as the volume fraction of antimony increases until the strength is about 2.24GPa at a volume fraction of 1.2%. Furthermore, the simulation's result in Chapter 5 show that the rate controlling process for nanocrystalline copper shifts from the gliding dislocation to interaction of dislocation and the grain boundaries, such as grain boundary sliding, as the grain size decreases. This increase in strength in doped nanocrystalline copper is primarily due to increased resistance to grain boundary sliding created by the antimony at the grain boundary as shown in Figure 6.5.

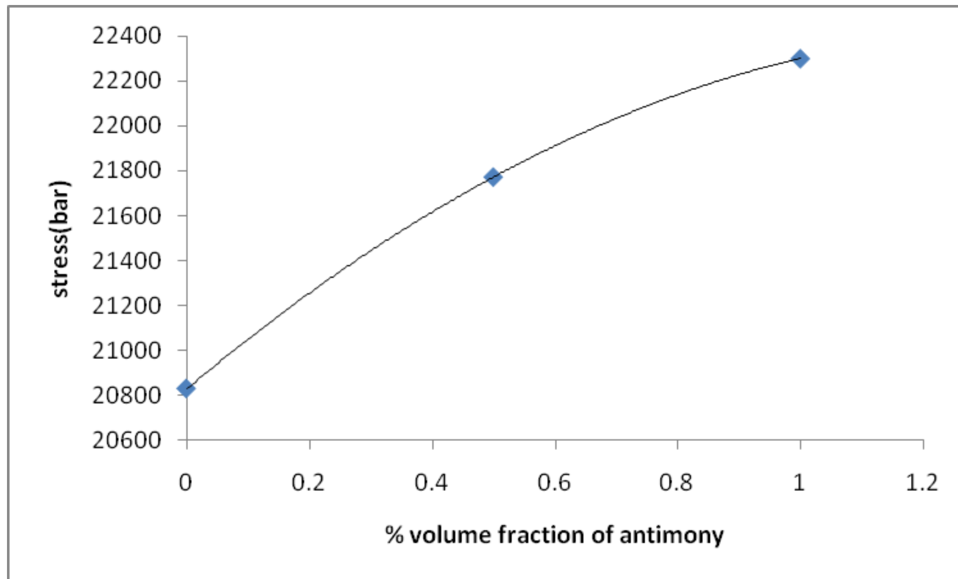

Figure 6.4: The relationship of the ultimate tensile strength copper with a grain size of 10nm

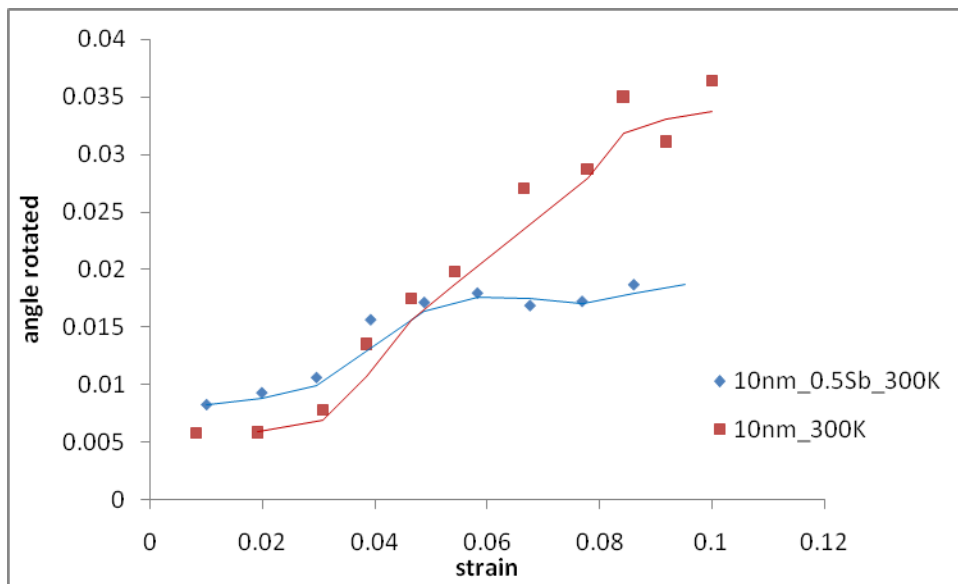

Figure 6.5: Comparison magnitude of grain rotation between pure nanocrystalline copper and nanocrystalline copper doped with 0.5% antimony

6.4 Cyclic loading

The simulation results in Chapter 5 show that nanocrystalline copper will experience stress driven grain coarsening during the interconnect's service life and this will cause the loss in strength in the interconnects. The mechanism for grain coarsening is identified in Chapter 5 as grain rotation and coalescence.

In Section 6.2 we showed that doped antimony at the grain boundary in nanocrystalline copper increases the resistance to grain boundary sliding during monotonic loading. Grain coarsening during cyclic loading may also slowed down by the presence of antimony at the grain boundaries. Although there is no published literature on microstructure stabilization during cyclic loading, recent molecular dynamics simulations by Millett et al. [14, 148, 149] have shown that temperature assisted grain growth can be eliminated by the presence of sufficient dopant atom content at the grain boundary.

In order to investigate the effectiveness of grain stabilization through the addition of dopants, this research compares the evolution of microstructure of both doped and pure nanocrystalline copper with an average grain size of 20nm subject to fatigue cycling. The total strain range used in this simulation is 1%. Furthermore, the evolution of microstructure for undeformed nanocrystalline copper is also included in Figure 6.6 as reference.

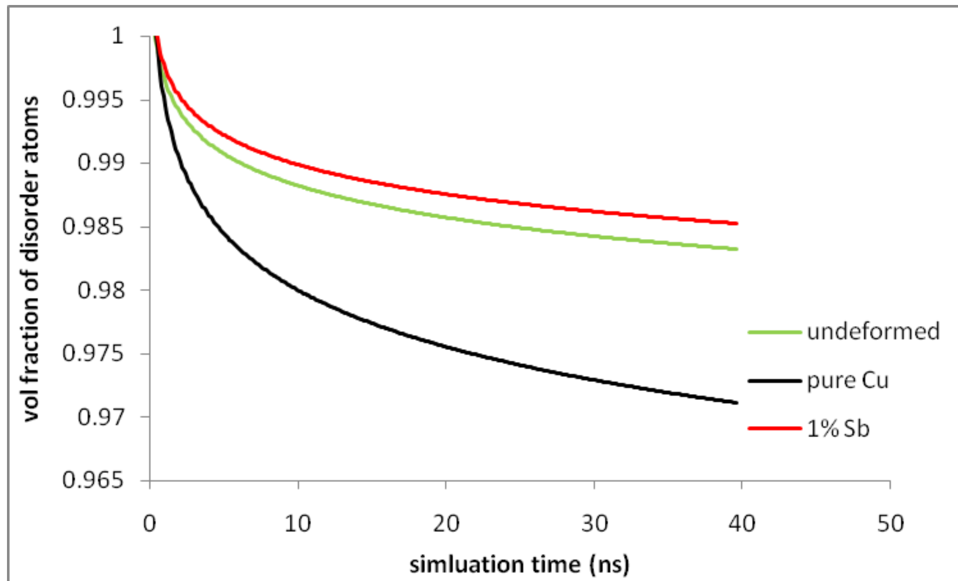

Figure 6.6: Comparisons of the evolution of microstructure for pure copper and doped copper under a cyclic loading of 1% total strain range

By comparing the evolution of the volume fraction of grain boundary atoms as the number of cycles increase, Figure 6.6 shows that grain growth for doped nanocrystalline copper decreases to a much lower rate as compared to pure copper under the same fatigue conditions. In fact, grain growth in doped nanocrystalline copper is even lower than the undeformed nanocrystalline copper. This is possible since Millett et al [14, 148, 149] had shown that temperature assisted grain growth can be eliminated with the presence of sufficient dopants atom contained at the grain boundary. Hence, minimum or no grain growth is detected in doped nanocrystalline copper. This observation can be confirmed by comparing the microstructure of the doped and pure copper after they had experience 100 fatigue cycle as shown in Figure 6.7. It can be clearly seen from Figure 6.7 that one of the grain had disappeared and the adjacent grain

have growth for pure nanocrystalline copper but the grain remained intact for doped nanocrystalline copper

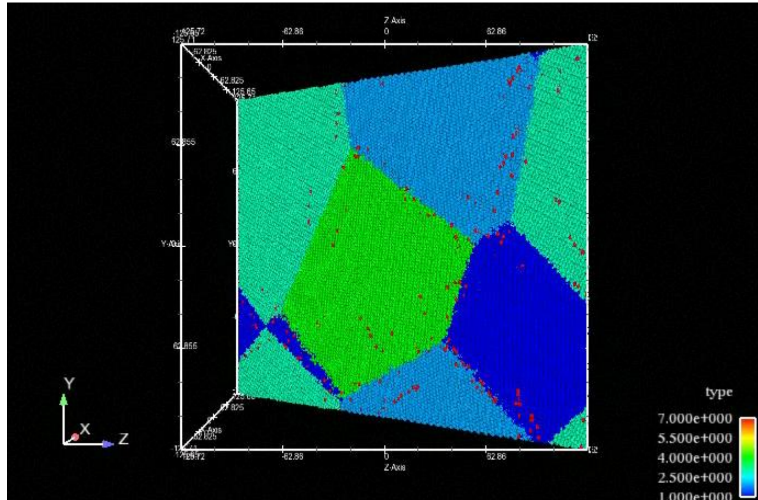

Grain growth detected

Grain remain

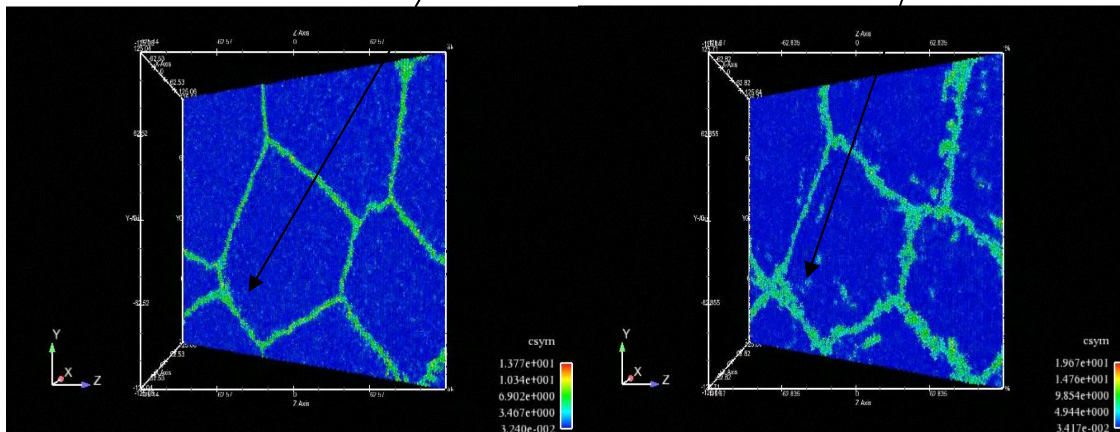

Figure 6.7: Comparison of the microstructures before and after fatigue cycling (a) the initial microstructure just before loading and (b) pure and (c) doped nanocrystalline copper after 100 cycles.

6.4 Conclusions

In conclusion, simulations results in this research have shown that addition of the antimony into nanocrystalline copper not only increases the microstructure stability during cyclic loading, it will also increase the strength of the nanocrystalline copper. It has been found in this work that the strength in nanocrystalline copper can be increased by as much as 8% by adding 1.2% volume fraction of antimony in nanocrystalline copper. This increase in strength has been identified as being due to the increase resistance to grain boundary sliding by having antimony at the grain boundary. Furthermore, this research also demonstrates that the stabilization of grain size in nanocrystalline copper during cyclic loading can be achieved through the addition of antimony in the grain boundary. In fact, simulations in this research show that additions of antimony in the copper grain boundary not only reduce the stress driven grain coarsening, it will also reduce the temperature driven grain coarsening. This enhanced stability has again been attributed to the increased resistance to grain boundary sliding by antimony at the grain boundary. This research has demonstrated the potential for improving the existing nanostructured interconnects technology through addition of small percentage of antimony into nanocrystalline copper.

Chapter 7

Conclusions and Recommendations

Of all the known interconnect technologies, nanostructured interconnects such as nanocrystalline copper are the most promising for meeting the high mechanical and electrical performance requirements of next generation devices. However, there is need to understand their material properties, their deformation mechanisms and their microstructural stability. Hence, the mechanical and fatigue behavior of nanocrystalline copper are studied using atomistic simulations with the objective of understanding and evaluating their performance as nanostructured interconnects materials. The conclusions of this research are listed below:

1. The results from the crack growth analysis indicate that nanocrystalline copper is in fact a suitable candidate for ultra-fine pitch interconnects applications. This study also predicts that crack growth is a relatively small portion of the total fatigue life of interconnects under LCF conditions. Hence, crack initiation life is the main factor in determining the fatigue life of interconnects.

2. The material properties of single crystal nano rods of copper have been computationally determined and their relationships with strain rate and temperature have been explored.

3. The nucleation stress for single crystal copper nano rod has been found to be a function of temperature but insensitive to strain rate. A close form solution for nucleation stress has been developed in this research as shown in equation 5.2. Furthermore, the controlling deformation mechanism in single crystal nano-rod has also been identified as the nucleation of dislocation.

4. Due to the large volume fraction of grain boundaries, the material properties of nanocrystalline copper such as modulus and yield strength have been found to be dependent on their grain size. Their modulus with respect to their average grain size had been characterized in this research as shown in equation 4.11 and equation 4.13.

5. The Hall-Petch and reverse Hall- Petch relationships have been investigated in this research and the grain size that produces the highest strength in copper has been found to be 15nm. The highest strength has been shown to be 1.93GPa.

6. Dislocation activities have been found to be the primary deformation mechanism for nanocrystalline copper in the Hall-Petch region with some or minimal grain rotation. Furthermore, the simulations performed in this research indicate that a higher amount of grain rotation is observed as a deformation mechanism in the reverse Hall-Petch region. Hence, this shows that there is a competition between the dislocation activity and grain boundary sliding to be the main deformation mode.

7. It is shown that stress induced grain coarsening is the main criterion for the nanocrystalline copper to lose its mechanical performance during cyclic loading. However, the simulation results have also shown that grain growth during fatigue

loading will be assisted by other mechanism such as dislocation activity and grain boundary migration. Hence, a fatigue model for nanostructured interconnects has been developed in this research using the above observation.

8. Simulation results have showed that addition of the antimony into nanocrystalline copper will not only increase the microstructure stability during cyclic loading, it will also increase the strength of the nanocrystalline copper. In this work, the strength in nanocrystalline copper can be increase by as much as 8% by adding 1.2% volume fraction of antimony in nanocrystalline copper.

In conclusion, this research has provided some basic understanding of the monotonic and fatigue behavior of single crystal copper nano rods and nanocrystalline copper. A fatigue model has been developed in this research and it has also been demonstrated that a methodology to improve the existing nanostructured interconnects technology through addition of small percentage of antimony into nanocrystalline copper. New avenues for research have been opened such as:-

1. Even though this research has demonstrated the feasibility of using nanocrystalline copper as the nanostructured interconnects, the fabrication of nanostructured interconnect using nanocrystalline copper still remains as an issue. There is a need to explored different techniques to fabricate these interconnects.
2. The crack growth analysis presented does not consider local microstructure effects on the crack; the starting crack length should be large relative to its microstructure length scale for these predictions to be accurate. Due to the small feature size of the nano-interconnects, there is some concern about the accuracy of the crack growth

calculations. Hence, in order to model the crack evolution more accurately, molecular dynamics should be employed instead of the continuum mechanics approach used previously in the estimation of crack growth life. Due to computational limitations, models involving only a few grains could be employed in our simulations There is a need to repeat these simulations with a larger number of atoms and grains to capture the corrects Physics of the problem.

3. Since stress driven grain coarsening in nanocrystalline copper is detrimental to the life of interconnects, a more systematic and in-depth computational study must be conducted on stabilizing grain growth during cyclic loading.

REFERENCES

1 Aggarwal, A.O., Raj, P.M., and Tummala, R.R.: 'High aspect ratio metal-polymer composite structures for nano interconnects', in Editor (Ed.)^(Eds.): 'Book High aspect ratio metal-polymer composite structures for nano interconnects' (IEEE, 2004, edn.), pp. 182-186

2 http://www.itrs.net/Links/2003ITRS/Home2003.htm. Accessed Dec 2003

3 Aggarwal, A.O., Markondeya Raj, P., Pratap, R.J., Saxena, A., and Tummala, R.R.: 'Design and fabrication of high aspect ratio fine pitch interconnects for wafer level packaging', in Editor (Ed.)^(Eds.): 'Book Design and fabrication of high aspect ratio fine pitch interconnects for wafer level packaging' (IEEE, 2002, edn.), pp. 229-234

4 Chng, A.C., Tay, A.A.O., Lim, K.M., and Wong, E.H.: 'Fatigue life estimation of a Stretched-Solder-Column ultra-fine-pitch wafer level package using the macro-micro modelling approach', in Editor (Ed.)^(Eds.): 'Book Fatigue life estimation of a Stretched-Solder-Column ultra-fine-pitch wafer level package using the macro-micro modelling approach' (Institute of Electrical and Electronics Engineers Inc., Piscataway, NJ 08855-1331, United States, 2004, edn.), pp. 1586-1591

5 Tummala, R.R.: 'SOP: What Is It And Why? A New Microsystem-Integration Technology Paradigm-Moore's Law For System Integration Of Miniaturized Convergent Systems Of The Next Decade', IEEE Transactions On advanced Packaging, 2004, 27, pp. 241-249

6 Gao, H., Ji, B., Jager, I.L., Arzt, E., and Fratzl, P.: 'Materials become insensitive to flaws at nanoscale: Lessons from nature', Proceedings of the National Academy of Sciences, 2003, 100, (10), pp. 5597-5600

7 Suryanarayana, C., and Koch, C.C.: 'Nanocrystalline materials-Current research and future directions', Hyperfine Interactions, 2000, 130, (1-4), pp. 5-44

8 Bansal, S.: 'Characterization Of Nanostructured Metals And Metal Nanowires For Chip-To-Package Interconnections ', Georgia Institute of Technology, 2006

9 Van Swygenhoven, H., Derlet, P.M., and Hasnaoui, A.: ‘Atomistic modeling of strength of nanocrystalline metals’, Advanced Engineering Materials, 2003, 5, (5), pp. 345-350

10 Weertman, J.R.: ‘Hall-Petch strengthening in nanocrystalline metals’, Material Science & Engineering A: Structural Materials: Properties, Microstructure and Processing, 1993, A166, (1-2), pp. 161-167

11 Lu, L., Sui, M.L., and Lu, K.: ‘Superplastic extensibility of nanocrystalline copper at room temperature’, Science, 2000, 287, (5457), pp. 1463-1466

12 Aggarwal, A.: ‘Chip-Package Nano-Structured Copper and Nickel Interconnections with Metallic and Polymeric Bonding Interfaces’

13 Kumar, K.S., Van Swygenhoven, H., and Suresh, S.: ‘Mechanical behavior of nanocrystalline metals and alloys’, Acta Materialia, 2003, 51, (19), pp. 5743-5774

14 Millett, P.C., Selvam, R.P., and Saxena, A.: ‘Molecular dynamics simulations of grain size stabilization in nanocrystalline materials by addition of dopants’, Acta Materialia, 2006, 54, (2), pp. 297-303

15 Zhang, K., Weertman, J.R., and Eastman, J.A.: ‘Rapid stress-driven grain coarsening in nanocrystalline Cu at ambient and cryogenic temperatures’, Applied Physics Letters, 2005, 87, (6), pp. 61921-61921

16 Tummala, R.R., and Rymaszewski, E.J.: ‘Microelectronics Packaging Handbook’ (Chapman & Hall, 1997. 1997)

17 Halbo, L., and Ohlckers, P.: ‘Electronic Components, Packaging and Production’ (University of Oslo, 1995. 1995)

18 Fjelstad, J., DiStefano, T., and Faraci, A.: ‘Wafer level packaging of compliant, chip size ICs’, Microelectronics International, 2000, 17, (2), pp. 23-27

19 Novitsky, J., and Miller, C.: ‘Wafer-level CSP, wafer-level assembly/test: integrating backend processes’, Solid State Technology, 2001, 44, (2), pp. 78-80

20 Lo, G., and Sitaraman, S.K.: ‘G-Helix: Lithography-based wafer-level compliant chip-to-substrate interconnects’, in Editor (Ed.)^(Eds.): ‘Book G-Helix: Lithography-based wafer-level compliant chip-to-substrate interconnects’ (Institute of Electrical and Electronics Engineers Inc., Piscataway, NJ 08855-1331, United States, 2004, edn.), pp. 320-325

21 Aggarwal, A., Markondeya Raj, P., Baik-Woo, L., Myung Jin, Y., Tambawala, A., Iyer, M., Swaminathan, M., Wong, C.P., and Tummala, R.: ‘Reliability of nano-structured nickel interconnections replacing flipchip solder assembly without underfill’, in Editor (Ed.)^(Eds.): ‘Book Reliability of nano-structured nickel interconnections replacing flipchip solder assembly without underfill’ (IEEE, 2007, edn.), pp. 905-913

22 Wang, Y.P., and Her, T.D.: ‘Advanced substrate technology for ball grid array in electronic packaging’, in Editor (Ed.)^(Eds.): ‘Book Advanced substrate technology for ball grid array in electronic packaging’ (IEEE, 2000, edn.), pp. 335-339

23 Gleiter, H.: ‘Nanostructured materials: basic concepts and microstructure’, Acta Materialia, 2000, 48, (1), pp. 1-29

24 Tjong, S.C., and Haydn, C.: ‘Nanocrystalline materials and coatings’, Materials Science & Engineering R: Reports, 2004, R45, (1-2), pp. 1-88

25 Sanders, P.G., Fougere, G.E., Thompson, L.J., Eastman, J.A., and Weertman, J.R.: ‘Improvements in the synthesis and compaction of nanocrystalline materials’, Nanostructured Materials, 1997, 8, (3), pp. 243-252

26 Koch, C.C.: ‘Synthesis of nanostructured materials by mechanical milling: Problems and opportunities’, Nanostructured Materials, 1997, 9, (1-8), pp. 13-22

27 Koch, C.C.: ‘Overview paper no. 2. The synthesis and structure of nanocrystalline materials produced by mechanical attrition. A review’, Nanostructured Materials, 1993, 2, (2), pp. 109

28 Erb, U.: ‘Electrodeposited nanocrystals: synthesis, properties and industrial applications’, in Editor (Ed.)^(Eds.): ‘Book Electrodeposited nanocrystals: synthesis, properties and industrial applications’ (1995, 5-8 edn.), pp. 533-538

29 Valiev, R.Z., Islamgaliev, R.K., and Alexandrov, I.V.: ‘Bulk nanostructured materials from severe plastic deformation’, Progress in Materials Science, 2000, 45, (2), pp. 103-189

30 Birringer, R., Gleiter, H., Klein, H.P., and Marquardt, P.: ‘Nanocrystalline materials-an approach to a novel solid structure with gas-like disorder?’, Physics Letters A, 1984, 102A, (8), pp. 365-369

31 Granqvist, C.G., and Buhrman, R.A.: ‘Ultrafine metal particles’, Journal of Applied Physics, 1976, 47, (5), pp. 2200-2219

32 Agnew, S.R., Elliott, B.R., Youngdahl, C.J., Hemker, K.J., and Weertman, J.R.: ‘Microstructure and mechanical behavior of nanocrystalline metals’, in Editor (Ed.)^(Eds.): ‘Book Microstructure and mechanical behavior of nanocrystalline metals’ (Elsevier, 2000, 1-2 edn.), pp. 391-396

33 Shen, Y.F., Lu, L., Lu, Q.H., Jin, Z.H., and Lu, K.: ‘Tensile properties of copper with nano-scale twins’, Scripta Materialia, 2005, 52, (10), pp. 989-994

34 Lu, L., Schwaiger, R., Shan, Z.W., Dao, M., Lu, K., and Suresh, S.: ‘Nano-sized twins induce high rate sensitivity of flow stress in pure copper’, Acta Materialia, 2005, 53, (7), pp. 2169-2179

35 Saran, M.J.: ‘Nanomaterials by severe plastic deformation: Fundamentals, modeling, and optimization’, JOM, 2004, 56, (10), pp. 57

36 Zehetbauer, M., Krystian, M., and Lacom, W.: ‘Bulk nanostructured metals by severe plastic deformation (SPD)’, in Editor (Ed.)^(Eds.): ‘Book Bulk nanostructured metals by severe plastic deformation (SPD)’ (Nano Science and Technology Institute, 2005, edn.), pp. 642-645

37 Dalla Torre, F., Lapovok, R., Sandlin, J., Thomson, P.F., Davies, C.H.J., and Pereloma, E.V.: 'Microstructures and properties of copper processed by equal channel angular extrusion for 1-16 passes', Acta Materialia, 2004, 52, (16), pp. 4819-4832

38 Sanders, P.G., Eastman, J.A., and Weertman, J.R.: 'Elastic and tensile behavior of nanocrystalline copper and palladium', Acta Materialia, 1997, 45, (10), pp. 4019-4025

39 Youssef, K.M., Scattergood, R.O., Murty, K.L., Horton, J.A., and Koch, C.C.: 'Ultrahigh strength and high ductility of bulk nanocrystalline copper', Applied Physics Letters, 2005, 87, (9), pp. 091904

40 Gai, P.L., Zhang, K., and Weertman, J.: 'Electron microscopy study of nanocrystalline copper deformed by a microhardness indenter', Scripta Materialia, 2007, 56, (1), pp. 25-28

41 Weertman, J.R.: 'Hall-Petch strengthening in nanocrystalline metals', Materials Science and Engineering A, 1993, 166, (1-2), pp. 161-167

42 Zhang, K., Chenoweth, A., Izzi, G., Lahoti, A., and Weertman, J.R.: 'Fatigue behavior of ultra-fine grain copper', JOM, 2004, 56, (11), pp. 157

43 Bansal, S., Saxena, A., Hartwig, T., and Tummala, R.R.: 'Mechanical properties of ECAE nanocrystalline copper and nickel', Journal of Metastable and Nanocrystalline Materials, 2005, 23, pp. 183-186

44 Bansal, S., Saxena, A., and Tummala, R.R.: 'Nanocrystalline copper and nickel as ultra high-density chip-to-package interconnections', in Editor (Ed.)^(Eds.): 'Book Nanocrystalline copper and nickel as ultra high-density chip-to-package interconnections' (Institute of Electrical and Electronics Engineers Inc., Piscataway, NJ 08855-1331, United States, 2004, edn.), pp. 1647-1651

45 Van Swygenhoven, H., and Weertman, J.R.: 'Deformation in nanocrystalline metals', Materials Today, 2006, 9, (5), pp. 24-31

46 Van Swygenhoven, H., Derlet, P.M., Budrovic, Z., and Hasnaoui, A.: ‘Unconventional deformation mechanism in nanocrystalline metals?’, Zeitschrift fuer Metallkunde/Materials Research and Advanced Techniques, 2003, 94, (10), pp. 1106-1110

47 Schiotz, J.: ‘Atomic-scale modeling of plastic deformation of nanocrystalline copper’, Scripta Materialia, 2004, 51, (8 SPEC. ISS.), pp. 837-841

48 Schiotz, J., and Jacobsen, K.W.: ‘A maximum in the strength of nanocrystalline copper’, Science, 2003, 301, (5638), pp. 1357-1359

49 Wolf, D., Yamakov, V., Phillpot, S.R., and Mukherjee, A.K.: ‘Deformation mechanism and inverse Hall-Petch behavior in nanocrystalline materials’, Zeitschrift fuer Metallkunde/Materials Research and Advanced Techniques, 2003, 94, (10), pp. 1091-1097

50 Yamakov, V., Wolf, D., Phillpot, S.R., Mukherjee, A.K., and Gleiter, H.: ‘Deformation mechanism crossover and mechanical behaviour in nanocrystalline materials’, Philosophical Magazine Letters, 2003, 83, (6), pp. 385-393

51 Yamakov, V., Wolf, D., Phillpot, S.R., Mukherjee, A.K., and Gleiter, H.: ‘Deformation-mechanism map for nanocrystalline metals by molecular-dynamics simulation’, Nature Materials, 2004, 3, (1), pp. 43-47

52 Chen, J., Lu, L., and Lu, K.: ‘Hardness and strain rate sensitivity of nanocrystalline Cu’, Scripta Materialia, 2006, 54, (11), pp. 1913-1918

53 Cheng, S., Ma, E., Wang, Y.M., Kecskes, L.J., Youssef, K.M., Koch, C.C., Trociewitz, U.P., and Han, K.: ‘Tensile properties of in situ consolidated nanocrystalline Cu’, Acta Materialia, 2005, 53, (5), pp. 1521-1533

54 Hall, E.O.: ‘The deformation and ageing of mild steel III. Discussion of results’, Proceedings of the Physical Society. Section B, 1951, 64, pp. 747-753

55 Petch, N.J.: ‘Cleavage strength of polycrystals’, Iron and Steel Institute -- Journal, 1953, 174, (Part 1), pp. 25-28

56 Jiang, H., Zhu, Y.T., Butt, D.P., Alexandrov, I.V., and Lowe, T.C.: ‘Microstructural evolution, microhardness and thermal stability of HPT-processed Cu’, Materials Science & Engineering A (Structural Materials: Properties, Microstructure and Processing), 2000, A290, (1-2), pp. 128-138

57 Nieman, G.W., Weertman, J.R., and Siegel, R.W.: ‘Mechanical behavior of nanocrystalline metals’, Nanostructured Materials, 1992, 1, (2), pp. 185-190

58 Sanders, P.G., Eastman, J.A., and Weertman, J.R.: ‘Tensile behavior of nanocrystalline copper’, in Editor (Ed.)^(Eds.): ‘Book Tensile behavior of nanocrystalline copper’ (Minerals, Metals & Materials Soc (TMS), 1996, edn.), pp. 379-386

59 Suryanarayanan Iyer, R., Frey, C.A., Sastry, S.M.L., Waller, B.E., and Buhro, W.E.: ‘Plastic deformation of nanocrystalline Cu and Cu-0.2 wt.% B’, Materials Science and Engineering A: Structural Materials: Properties, Microstructure and Processing, 1999, 264, (1), pp. 210-214

60 Lu, L., Shen, Y., Chen, X., Qian, L., and Lu, K.: ‘Ultrahigh Strength and High Electrical Conductivity in Copper’, Science, 2004, 304, (5669), pp. 422-426

61 Valiev, R.Z., Alexandrov, I.V., Zhu, Y.T., and Lowe, T.C.: ‘Paradox of strength and ductility in metals processed by severe plastic deformation’, Journal of Materials Research, 2002, 17, (1), pp. 5-8

62 Youssef, K.M., Scattergood, R.O., Murty, K.L., and Koch, C.C.: ‘Ultratough nanocrystalline copper with a narrow grain size distribution’, Applied Physics Letters, 2004, 85, (6), pp. 929-931

63 Hayashi, K., and Etoh, H.: ‘Pressure sintering of iron, cobalt, nickel and copper ultrafine powders and the crystal grain size and hardness of the compacts’, Transactions of the Japan Institute of Metals, 1989, 30, (11), pp. 925-931

64 Haouaoui, M., Karaman, I., Maier, H.J., and Hartwig, K.T.: ‘Microstructure evolution and mechanical behavior of bulk copper obtained by consolidation of micro- and nanopowders using equal-channel angular extrusion’, Metallurgical and Materials Transactions A (Physical Metallurgy and Materials Science), 2004, 35A, (9), pp. 2935-2949

65 Qing, X., and Xingming, G.: ‘The scale effect on the yield strength of nanocrystalline materials’, International Journal of Solids and Structures, 2006, 43, (25-26), pp. 7793-7799

66 Conrad, H., and Narayan, J.: ‘On the grain size softening in nanocrystalline materials’, Scripta Materialia, 2000, 42, (11), pp. 1025-1030

67 Van Swygenhoven, H., Caro, A., and Farkas, D.: ‘Grain boundary structure and its influence on plastic deformation of polycrystalline FCC metals at the nanoscale: A molecular dynamics study’, Scripta Materialia, 2001, 44, (8-9), pp. 1513-1516

68 Conrad, H.: ‘Grain size dependence of the plastic deformation kinetics in Cu’, Materials Science & Engineering A (Structural Materials: Properties, Microstructure and Processing), 2003, A341, (1-2), pp. 216-228

69 Carreker, J.R.P., and Hibbard, J.W.R.: ‘Tensile deformation of high purity as function of temperature, strain rate, and grain size’, Acta Metallurgica, 1953, 1, (6), pp. 654-663

70 Elmustafa, A.A., Tambwe, M.F., and Stone, D.S.: ‘Activation volume analysis of plastic deformation in fcc materials using nanoindentation’, in Editor (Ed.)^(Eds.): ‘Book Activation volume analysis of plastic deformation in fcc materials using nanoindentation’ (Materials Research Society, 2002, edn.), pp. 77-82

71 Lu, L., Li, S.X., and Lu, K.: ‘An abnormal strain rate effect on tensile behavior in nanocrystalline copper’, Scripta Materialia, 2001, 45, (10), pp. 1163-1169

72 Taylor, G., and Saka, H.: 'Some observations on slip in niobium and Nb-Ti alloy deformed in situ in a HVEM', Philosophical Magazine A (Physics of Condensed Matter, Defects and Mechanical Properties), 1991, 64, (6), pp. 1345-1354

73 Cahn, J.W., and Nabarro, F.R.N.: 'Thermal activation under shear', Philosophical Magazine A (Physics of Condensed Matter: Structure, Defects and Mechanical Properties), 2001, 81, (5), pp. 1409-1426

74 Wang, Y.M., and Ma, E.: 'Temperature and strain rate effects on the strength and ductility of nanostructured copper', Applied Physics Letters, 2003, 83, (15), pp. 3165-3167

75 Huang, Z., Gu, L.Y., and Weertman, J.R.: 'Temperature dependence of hardness of nanocrystalline copper in low-temperature range', Scripta Materialia, 1997, 37, (7), pp. 1071-1075

76 Hertzberg, R.W.: 'Deformation and Fracture Mechanics of Engineering Materials' (Wiley, 1996. 1996)

77 Ma, E.: 'Instabilities and ductility of nanocrystalline and ultrafine-grained metals', Scripta Materialia, 2003, 49, (7), pp. 663-668

78 Youssef, K.M., Scattergood, R.O., Murty, K.L., Horton, J.A., and Koch, C.C.: 'Ultrahigh strength and high ductility of bulk nanocrystalline copper', Applied Physics Letters, 2005, 87, (9), pp. 91904-91901

79 Kumar, K.S., Suresh, S., Chisholm, M.F., Horton, J.A., and Wang, P.: 'Deformation of electrodeposited nanocrystalline nickel', Acta Materialia, 2003, 51, (2), pp. 387-405

80 Dao, M., Lu, L., Asaro, R.J., De Hosson, J.T.M., and Ma, E.: 'Toward a quantitative understanding of mechanical behavior of nanocrystalline metals', Acta Materialia, 2007, 55, (12), pp. 4041-4065

81 Hasnaoui, A., Van Swygenhoven, H., and Derlet, P.M.: 'Dimples on nanocrystalline fracture surfaces as evidence for shear plane formation', Science, 2003, 300, (5625), pp. 1550-1552

82 Gleiter, H.: ‘Nanocrystalline materials’, Progress in Materials Science, 1989, 33, (4), pp. 223-315

83 Mukherjee, A.K., Bird, J.E., and Dorn, J.E.: ‘Experimental correlations for high-temperature creep’, ASM (American Society for Metals) Transactions, 1969, 62, (1), pp. 155-179

84 Cai, B., Kong, Q.P., Lu, L., and Lu, K.: ‘Low temperature creep of nanocrystalline pure copper’, Materials Science and Engineering A: Structural Materials: Properties, Microstructure and Processing, 2000, 286, (1), pp. 188-192

85 Sanders, P.G., Rittner, M., Kiedaisch, E., Weertman, J.A., Kung, H., and Lu, Y.C.: ‘Creep of nanocrystalline Cu, Pd, and Al-Zr’, Nanostructured Materials, 1997, 9, (1-8), pp. 433-440

86 Nieman, G.W., Weertman, J.R., and Siegel, R.W.: ‘Mechanical behavior of nanocrystalline Cu and Pd’, Journal of Materials Research, 1991, 6, (5), pp. 1012-1027

87 Grabovetskaya, G.P., Ivanov, K.V., and Kolobov, Y.R.: ‘Creep features of nanostructured materials produced by severe plastic deformation’, Annales de Chimie (Science des Materiaux), 2002, 27, (3), pp. 89-98

88 Valiev, R.Z., Kozlov, E.V., Ivanov, Y.F., Lian, J., Nazarov, A.A., and Baudelet, B.: ‘Deformation behaviour of ultra-fine-grained copper’, Acta Metallurgica et Materialia, 1994, 42, (7), pp. 2467-2475

89 Yamakov, V., Wolf, D., Phillpot, S.R., and Gleiter, H.: ‘Grain-boundary diffusion creep in nanocrystalline palladium by molecular-dynamics simulation’, Acta Materialia, 2002, 50, (1), pp. 61-73

90 Haslam, A.J., Yamakov, V., Moldovan, D., Wolf, D., Phillpot, S.R., and Gleiter, H.: ‘Effects of grain growth on grain-boundary diffusion creep by molecular-dynamics simulation’, Acta Materialia, 2004, 52, (7), pp. 1971-1987

91 Suresh, S.: ‘FATIGUE CRACK DEFLECTION AND FRACTURE SURFACE CONTACT: MICROMECHANICAL MODELS’, Metallurgical Transactions A (Physical Metallurgy and Materials Science), 1985, 16A, (2), pp. 249-260

92 Witney, A.B., Sanders, P.G., Weertman, J.R., and Eastman, J.A.: ‘Fatigue of nanocrystalline copper’, Scripta Metallurgica et Materialia, 1995, 33, (12), pp. 2025-2030

93 Hanlon, T., Kwon, Y.N., and Suresh, S.: ‘Grain size effects on the fatigue response of nanocrystalline metals’, Scripta Materialia, 2003, 49, (7), pp. 675-680

94 Hanlon, T., Tabachnikova, E.D., and Suresh, S.: ‘Fatigue behavior of nanocrystalline metals and alloys’, in Editor (Ed.)^(Eds.): ‘Book Fatigue behavior of nanocrystalline metals and alloys’ (Elsevier Ltd, Oxford, OX5 1GB, United Kingdom, 2005, 10-12 edn.), pp. 1147-1158

95 Agnew, S.R., and Weertman, J.R.: ‘Cyclic softening of ultrafine grain copper’, Materials science & engineering. A, Structural materials: properties, microstructure and processing, 1998, 244, (2), pp. 145-153

96 Vinogradov, A., Kaneko, Y., Kitagawa, K., Hashimoto, S., Stolyarov, V., and Valiev, R.: ‘Cyclic response of ultrafine-grained copper at constant plastic strain amplitude’, Scripta Materialia, 1997, 36, (11), pp. 1345-1351

97 Hashimoto, S., Kaneko, Y., Kitagawa, K., Vinogradov, A., and Valiev, R.Z.: ‘On the cyclic behaviour of ultra-fine grained copper produced by equi-channel angular pressing’, Materials Science Forum, 1999, 312, pp. 593-598

98 Mughrabi, H., Hoppel, H.W., and Kautz, M.: ‘Fatigue and microstructure of ultrafine-grained metals produced by severe plastic deformation’, Scripta Materialia, 2004, 51, (8 SPEC ISS), pp. 807-812

99 Hoppel, H.W., Zhou, Z.M., Mughrabi, H., and Valiev, R.Z.: ‘Microstructural study of the parameters governing coarsening and cyclic softening in fatigued ultrafine-grained copper’, Philosophical Magazine A, 2002, 82, (9), pp. 1781-1794

100 Chang, W.-J., and Fang, T.-H.: 'Influence of temperature on tensile and fatigue behavior of nanoscale copper using molecular dynamics simulation', Journal of the Physics and Chemistry of Solids, 2003, 64, (8), pp. 1279-1283

101 Chang, W.-J.: 'Molecular-dynamics study of mechanical properties of nanoscale copper with vacancies under static and cyclic loading', Microelectronic Engineering, 2003, 65, (1-2), pp. 239-246

102 Farkas, D., Van Petegem, S., Derlet, P.M., and Van Swygenhoven, H.: 'Dislocation activity and nano-void formation near crack tips in nanocrystalline Ni', Acta Materialia, 2005, 53, (11), pp. 3115-3123

103 Farkas, D., Willemann, M., and Hyde, B.: 'Atomistic mechanisms of fatigue in nanocrystalline metals', Physical Review Letters, 2005, 94, (16), pp. 165502

104 Miyazaki, N., and Nishimura, K.: 'Molecular dynamics simulation of crack growth under cyclic loading', Computational Materials Science, 2004, 31, (3-4), pp. 269-278

105 Hugo, R.C., Kung, H., Weertman, J.R., Mitra, R., Knapp, J.A., and Follstaedt, D.M.: 'In-situ TEM tensile testing of DC magnetron sputtered and pulsed laser deposited Ni thin films', Acta Materialia, 2003, 51, (7), pp. 1937-1943

106 Derlet, P.M., Hasnaoui, A., and Van Swygenhoven, H.: 'Atomistic simulations as guidance to experiments', Viewpoint Set No. 31. Mechanical Properties of Fully Dense, 2003, 49, (7), pp. 629-635

107 Youngdahl, C.J., Hugo, R.C., Kung, H., and Weertman, J.R.: 'TEM observation of nanocrystalline copper during deformation', in Editor (Ed.)^(Eds.): 'Book TEM observation of nanocrystalline copper during deformation' (Materials Research Society, 2001, edn.), pp. 1-2

108 Wu, X.-L., and Ma, E.: 'Dislocations in nanocrystalline grains', Applied Physics Letters, 2006, 88, (23), pp. 231911

109 Youngdahl, C.J., Weertman, J.R., Hugo, R.C., and Kung, H.H.: 'Deformation behavior in nanocrystalline copper', Scripta Materialia, 2001, 44, (8-9), pp. 1475-1478

110 Van Swygenhoven, H., Derlet, P.M., and Froseth, A.G.: 'Nucleation and propagation of dislocations in nanocrystalline fcc metals', Acta Materialia, 2006, 54, (7), pp. 1975-1983

111 Ke, M., Hackney, S.A., Milligan, W.W., and Aifantis, E.C.: 'Observation and measurement of grain rotation and plastic strain in nanostructured metal thin films', Nanostructured Materials, 1995, 5, (6), pp. 689

112 Shan, Z., Stach, E.A., Wiezorek, J.M.K., Knapp, J.A., Follstaedt, D.M., and Mao, S.X.: 'Grain boundary-mediated plasticity in nanocrystalline nickel', Science, 2004, 305, (5684), pp. 654-657

113 Wang, Y.M., Hamza, A.V., and Ma, E.: 'Temperature-dependent strain rate sensitivity and activation volume of nanocrystalline Ni', Acta Materialia, 2006, 54, (10), pp. 2715-2726

114 Van Swygenhoven, H.: 'Grain boundaries and dislocations', Science, 2002, 296, (5565), pp. 66-67

115 Schiotz, J., Vegge, T., Di Tolla, F.D., and Jacobsen, K.W.: 'Atomic-scale simulations of the mechanical deformation of nanocrystalline metals', Physical Review B (Condensed Matter), 1999, 60, (17), pp. 11971-11983

116 van Swygenhoven, H., Derlet, P.M., and Froseth, A.G.: 'Stacking fault energies and slip in nanocrystalline metals', Nature Materials, 2004, 3, (6), pp. 399-403

117 Zhu, B., Asaro, R.J., Krysl, P., and Bailey, R.: 'Transition of deformation mechanisms and its connection to grain size distribution in nanocrystalline metals', Acta Materialia, 2005, 53, (18), pp. 4825-4838

118 Humphreys, F.J., and Hatherly, M.: 'Recrystallization and Related Annealing Phenomena, 1995', Oxford, Pergamon Press.

119 Herring, C., and Kingston, W.E.: 'The Physics of Powder Metallurgy', McGraw-Hill, New York, 1951, pp. 143

120 Haslam, A.J., Phillpot, S.R., Wolf, D., Moldovan, D., and Gleiter, H.: 'Mechanisms of grain growth in nanocrystalline fcc metals by molecular-dynamics simulation', Materials Science & Engineering A (Structural Materials: Properties, Microstructure and Processing), 2001, A318, (1-2), pp. 293-312

121 Li, J.C.M.: 'Mechanical grain growth in nanocrystalline copper', Physical Review Letters, 2006, 96, (21), pp. 215506-215501

122 Haslam, A.J., Moldovan, D., Yamakov, V., Wolf, D., Phillpot, S.R., and Gleiter, H.: 'Stress-enhanced grain growth in a nanocrystalline material by molecular-dynamics simulation', Acta Materialia, 2003, 51, (7), pp. 2097-2112

123 Schiotz, J.: 'Strain-induced coarsening in nanocrystalline metals under cyclic deformation', Materials Science and Engineering A, 2004, 375-377, (1-2 SPEC ISS), pp. 975-979

124 Weissmuller, J., Krauss, W., Haubold, T., Birringer, R., and Gleiter, H.: 'Atomic structure and thermal stability of nanostructured Y-Fe alloys', Nanostructured Materials, 1992, 1, (6), pp. 439-447

125 Gertsman, V.Y., and Birringer, R.: 'On the room-temperature grain growth in nanocrystalline copper', Scripta Metallurgica et Materialia, 1994, 30, (5), pp. 577-581

126 Wendrock, H., Bruckner, W., Hecker, M., Koetter, T.G., and Schloerb, H.: 'Room temperature grain growth in electroplated copper thin films', in Editor (Ed.)^(Eds.): 'Book Room temperature grain growth in electroplated copper thin films' (Elsevier, 2000, 8-10 edn.), pp. 1301-1304

127 Detavernier, C., Deduytsche, D., Van Meirhaeghe, R.L., De Baerdemaeker, J., and Dauwe, C.: 'Room-temperature grain growth in sputter-deposited Cu films', Applied Physics Letters, 2003, 82, (12), pp. 1863-1865

128 Haber, J.A., and Buhro, W.E.: 'Kinetic instability of nanocrystalline aluminum prepared by chemical synthesis; facile room-temperature grain growth', Journal of the American Chemical Society, 1998, 120, (42), pp. 10847-10855

129 Schell, N., Jensen, T., Petersen, J.H., Andreasen, K.P., Bottiger, J., and Chevallier, J.: 'The nanostructure evolution during and after magnetron deposition of Au films', Thin Solid Films, 2003, 441, (1-2), pp. 96-103

130 Pantleon, K., and Somers, M.A.J.: 'In situ investigation of the microstructure evolution in nanocrystalline copper electrodeposits at room temperature', Journal of Applied Physics, 2006, 100, (11), pp. 114319

131 Spearot, D.E., Jacob, K.I., and McDowell, D.L.: 'Nucleation of dislocations from [001] bicrystal interfaces in aluminum', Acta Materialia, 2005, 53, (13), pp. 3579-3589

132 Bansal, S.: 'Characterization of Nanostructured Metals and Metal Nanowires for Chip-To-Package Interconnections', Georgia Institute of Technology, 2006

133 Ghauri, I.M., Butt, M.Z., and Raza, S.M.: 'Grain growth in copper and alpha-brasses', Journal of Materials Science, 1990, 25, (11), pp. 4782-4784

134 Mengelberg, H.D., Meixner, M., and Lücke, K.: 'The Kinetics of the Recrystallization of Copper Deformed at Low Temperatures', Acta Metallurgica, 1965, 13, (7), pp. 835-844

135 Gust, W., Mayer, S., Bogel, A., and Predel, B.: 'Generalized representation of grain boundary self-diffusion data', in Editor (Ed.)^(Eds.): 'Book Generalized representation of grain boundary self-diffusion data' (1985, C-4 edn.), pp. 537-544

136 Natter, H., Schmelzer, M., Loffler, M.S., Krill, C.E., Fitch, A., and Hempelmann, R.: 'Grain-growth kinetics of nanocrystalline iron studied in situ by synchrotron real-time X-ray diffraction', Journal of Physical Chemistry B, 2000, 104, (11), pp. 2467-2476

137 Molodova, X., Gottstein, G., Winning, M., and Hellmig, R.J.: ‘Thermal stability of ECAP processed pure copper’, Materials Science & Engineering A (Structural Materials: Properties, Microstructure and Processing), 2007, 460-461, pp. 204-213

138 Tanimoto, H., Farber, P., Wurschum, R., Valiev, R.Z., and Schaefer, H.E.: ‘Self-diffusion in high-density nanocrystalline Fe’, in Editor (Ed.)^(Eds.): ‘Book Self-diffusion in high-density nanocrystalline Fe’ (Elsevier, 1999, 5-8 edn.), pp. 681-684

139 Zhang, K., Weertman, J.R., and Eastman, J.A.: ‘The influence of time, temperature, and grain size on indentation creep in high-purity nanocrystalline and ultrafine grain copper’, Applied Physics Letters, 2004, 85, (22), pp. 5197-5199

140 Zhu, B., Asaro, R.J., Krysl, P., Zhang, K., and Weertman, J.R.: ‘Effects of grain size distribution on the mechanical response of nanocrystalline metals: Part II’, Acta Materialia, 2006, 54, (12), pp. 3307-3320

141 Gai, P.L., Kai, Z., and Weertman, J.: ‘Electron microscopy study of nanocrystalline copper deformed by a microhardness indenter’, Scripta Materialia, 2007, 56, (1), pp. 25-28

142 Sansoz, F., and Dupont, V.: ‘Grain growth behavior at absolute zero during nanocrystalline metal indentation’, in Editor (Ed.)^(Eds.): ‘Book Grain growth behavior at absolute zero during nanocrystalline metal indentation’ (American Institute of Physics, 2006, edn.), pp. 111901-111901

143 Gutkin, M.Y., and Ovid'Ko, I.A.: ‘Grain boundary migration as rotational deformation mode in nanocrystalline materials’, Applied Physics Letters, 2005, 87, (25), pp. 251916

144 Ovid'ko, I.A., and Sheinerman, A.G.: ‘Special rotational deformation in nanocrystalline metals and ceramics’, Scripta Materialia, 2008, 59, (1), pp. 119-122

145 Ovid'ko, I.A., and Sheinerman, A.G.: ‘Special rotational deformation in nanocrystalline metals and ceramics’, Scripta Materialia, 2008, 59, (1), pp. 119-122

146 Randle, V.: 'The Role of the Coincidence Site Lattice in Grain Boundary Engineering' (The Institute of Materials, 1996. 1996)

147 Krill, C.E., Klein, R., Janes, S., and Birringer, R.: 'Thermodynamic stabilization of grain boundaries in nanocrystalline alloys', Proceedings of the International Symposium on Metastable, Mechanically Alloyed and Nanocrystalline Materials, Jun 27-Jul 1 1994, 1995, 179-181, pp. 443-448

148 Millett, P.C., Selvam, R.P., Bansal, S., and Saxena, A.: 'Atomistic simulation of grain boundary energetics - Effects of dopants', Acta Materialia, 2005, 53, (13), pp. 3671-3678

149 Millett, P.C., Selvam, R.P., and Saxena, A.: 'Stabilizing nanocrystalline materials with dopants', Acta Materialia, 2007, 55, (7), pp. 2329-2336

150 Bakonyi, I., Toth-Kadar, E., Toth, J., Tarnoczil, T., and Cziraki, A.: 'Microstructure, electrical transport and magnetic studies of electrodeposited nanocrystalline Ni, Co and Cu metals', in Editor (Ed.)^(Eds.): 'Book Microstructure, electrical transport and magnetic studies of electrodeposited nanocrystalline Ni, Co and Cu metals' (Minerals, Metals & Materials Soc (TMS), 1996, edn.), pp. 465-476

151 Allen, M.P., and Tildesley, D.J.: 'Computer Simulation of Liquids' (Oxford University Press, USA, 1989. 1989)

152 Frenkel, D., and Smit, B.: 'Understanding Molecular Simulation' (Academic Press, Inc. Orlando, FL, USA, 2001. 2001)

153 Haile, J.M.: 'Molecular Dynamics Simulation: Elementary Methods', J. Am. Chem. Soc, 1976, pp. 98

154 Liu, J.S., and Chen, R.: 'Sequential Monte Carlo Methods for Dynamic Systems', JOURNAL-AMERICAN STATISTICAL ASSOCIATION, 1998, 93, pp. 1032-1044

155 Metropolis, N., Rosenbluth, A.W., Rosenbluth, M.N., Teller, A.H., and Teller, E.: 'Equation of state calculations by fast computing machines', Journal of Chemical Physics, 1953, 21, pp. 1087-1092

156 Vanderplaats, G.N.: 'Numerical optimization techniques for engineering design' (McGraw-Hill)

157 Shewchuk, J.R.: 'An introduction to the conjugate gradient method without the agonizing pain', unpublished paper

158 Spearot, D.E.: 'Interface cohesion relations based on molecular dynamics simulations'

159 Martyna, G.J., Tuckerman, M.E., Tobias, D.J., and Klein, M.L.: 'Explicit reversible integrators for extended systems dynamics', Molecular Physics, 1996, 87, (5), pp. 1117-1157

160 Swope, W.C., Andersen, H.C., Berens, P.H., and Wilson, K.R.: 'A computer simulation method for the calculation of equilibrium constants for the formation of physical clusters of molecules: application to small water clusters', Journal of Chemical Physics, 1982, 76, (1), pp. 637-649

161 http://lammps.sandia.gov/bench.html Accessed Jan 2007

162 Hoover, W.G.: 'Canonical dynamics: equilibrium phase-space distributions', Physical Review A (General Physics), 1985, 31, (3), pp. 1695-1697

163 Parrinello, M., and Rahman, A.: 'Polymorphic transitions in single crystals: a new molecular dynamics method', Journal of Applied Physics, 1981, 52, (12), pp. 7182-7190

164 Nose, S.: 'A molecular dynamics method for simulations in the canonical ensemble', Molecular Physics, 1984, 52, (2), pp. 255-268

165 Melchionna, S., Ciccotti, G., and Holian, B.L.: 'Hoover NPT dynamics for systems varying in shape and size', Molecular Physics, 1993, 78, (3), pp. 533-544

166 Yamakov, V., Wolf, D., Salazar, M., Phillpot, S.R., and Gleiter, H.: 'Length-scale effects in the nucleation of extended dislocations in nanocrystalline Al by molecular-dynamics simulation', Acta Materialia, 2001, 49, (14), pp. 2713-2722

167 Spearot, D.E.: 'Atomistic Calculations of Nanoscale Interface Behavior in FCC Metals', Georigia Insititute of Technology, 2005

168 Zhou, M.: 'The virial stress is not a measure of mechanical stress', in Editor (Ed.)^(Eds.): 'Book The virial stress is not a measure of mechanical stress' (Materials Research Society, 2002, edn.), pp. 59-70

169 Zimmerman, J.A., Webb Iii, E.B., Hoyt, J.J., Jones, R.E., Klein, P.A., and Bammann, D.J.: 'Calculation of stress in atomistic simulation', Modelling and Simulation in Materials Science and Engineering, 2004, 12, (4), pp. 319-332

170 Carlsson, A.E.: 'Beyond Pair Potentials in Elemental Transition Metals and Semiconductors', Solid State Physics, 1990, 43, (1)

171 Frattini, R., and Della Valle, R.G.: 'Molecular-dynamics simulation of glassy Cu_{33} Y_{67}', Physical Review B, 1994, 50, (6), pp. 3620-3624

172 Albano, F., Lacevic, N., Falk, M.L., and Glotzer, S.C.: 'Relating metallic glass mechanical properties to liquid structure', Materials Science & Engineering A, 2004, 375, pp. 671-674

173 Lennard-Jones, J.E., and Devonshire, A.F.: 'The Interaction of Atoms and Molecules with Solid Surfaces. VI. The Behaviour of Adsorbed Helium at Low Temperatures', Proceedings of the Royal Society of London. Series A, Mathematical and Physical Sciences, 1937, 158, (894), pp. 242-252

174 Millett, P.C.: 'Atomistic Simulations of the Role of Dopant Atoms in Grain Growth and Deformation in Nanocrystalline Materials', University of Arkansas, Fayetteville, 2006

175 Chang, H.K., Weidman, R.S., and Lee, J.K.: 'An atomistic study of grain boundary segregation and cracking', in Editor (Ed.)^(Eds.): 'Book An atomistic study of grain boundary segregation and cracking' (1984, 1 edn.), pp. 224-252

176 Rajgarhia, R.K., Spearot, D.E., and Saxena, A.: 'Interatomic Potential for Copper-Antimony in Dilute Solid-Solution Alloys ', (To be published)

177 Leach, A.: 'Molecular Modelling: Principles and Applications' (Prentice Hall, 2001. 2001)

178 Daw, M.S., and Baskes, M.I.: 'Embedded-atom method: derivation and application to impurities, surfaces, and other defects in metals', Physical Review B (Condensed Matter), 1984, 29, (12), pp. 6443-6453

179 Stott, M.J., and Zaremba, E.: 'Quasiatoms: An approach to atoms in nonuniform electronic systems', Physical Review B (Condensed Matter), 1980, 22, (4), pp. 1564-1533

180 Norskov, J.K.: 'Covalent effects in the effective-medium theory of chemical binding: hydrogen heats of solution in the 3d metals', Physical Review B (Condensed Matter), 1982, 26, (6), pp. 2875-2885

181 Foiles, S.M., Baskes, M.I., and Daw, M.S.: 'Embedded-atom-method functions for the FCC metals Cu, Ag, Au, Ni, Pd, Pt, and their alloys', Physical Review B (Condensed Matter), 1986, 33, (12), pp. 7983-7991

182 Baskes, M.I.: 'Modified embedded-atom potentials for cubic materials and impurities', Physical Review B (Condensed Matter), 1992, 46, (5), pp. 2727-2742

183 Zimmerman, J.A., Gao, H., and Abraham, F.F.: 'Generalized stacking fault energies for embedded atom FCC metals', Modelling and Simulation in Materials Science and Engineering, 2000, 8, (2), pp. 103-116

184 Hirth, J.P., Lothe, Jens: ‘Theory of dislocations ’ (New York : Wiley, c1982, 1982. 1982)

185 Rice, J.R.: ‘Dislocation nucleation from a crack tip. An analysis based on the Peierls concept’, Journal of the Mechanics and Physics of Solids, 1992, 40, (2), pp. 239

186 Kelchner, C.L., Plimpton, S.J., and Hamilton, J.C.: ‘Dislocation nucleation and defect structure during surface indentation’, Physical Review B (Condensed Matter), 1998, 58, (17), pp. 11085-11088

187 Clarke, A.S., and Jonsson, H.: ‘Structural changes accompanying densification of random hard-sphere packings’, Physical Review E (Statistical Physics, Plasmas, Fluids, and Related Interdisciplinary Topics), 1993, 47, (6), pp. 3975-3984

188 Zimmerman, J.A., Kelchner, C.L., Klein, P.A., Hamilton, J.C., and Foiles, S.M.: ‘Surface step effects on nanoindentation’, Physical Review Letters, 2001, 87, (16), pp. 165507-165501

189 Ju, L., Ngan, A.H.W., and Gumbsch, P.: ‘Atomistic modeling of mechanical behavior’, Acta Materialia, 2003, 51, (19), pp. 5711-5742

190 Tschopp, M.A.: ‘Atomistic Simulations of Dislocation Nucleation in Single Crystals and Grain Boundaries’, Georgia Institute of Technology, 2007

191 Du, Q., Faber, V., and Gunzburger, M.: ‘Centroidal Voronoi tessellations: applications and algorithms’, SIAM Review, 1999, 41, (4), pp. 637-676

192 Saxena, A.: ‘Nonlinear Fracture Mechanics for Engineers’ (CRC Press, 1998. 1998)

193 Newman, J.C., Jr., and Raju, I.S.: ‘stress-intensity factor equations for cracks in three-dimensional finite bodies’, in Editor (Ed.)^(Eds.): ‘book stress-intensity factor equations for cracks in three-dimensional finite bodies’ (ASTM, Philadelphia, Pa, USA, 1983, edn.), pp. 238-265

194 Findley, K.O., Koh, S.W., and Saxena, A.: ‘J-integral expressions for semi-elliptical cracks in round bars’, International Journal of Fatigue, 2007, 29, (5), pp. 822-828

195 Aggarwal, A.: ‘Chip-Package Nano-Structured Copper and Nickel Interconnections with Metallic and Polymeric Bonding Interfaces’, Georgia Institute of TEchnology, 2006

196 Lamba, H.S.: ‘The J-integral applied to cyclic loading. [Life prediction for fatigue crack initiation]’, Engineering Fracture Mechanics, 1975, 7, (4), pp. 693-701

197 Findley, K.O.: ‘Physically-based models for elevated temperature low cycle fatigue crack initiation and growth in Rene 88DT’, Georgia Institute of Technology, 2005

198 Ramberg, W., Osgood, W.R., National Advisory Committee for, A., and United, S.: ‘Description of Stress-strain Curves by Three Parameters’ (National Advisory Committee for Aeronautics, 1943. 1943)

199 Plimpton, S.: ‘Fast parallel algorithms for short-range molecular dynamics’, Journal of Computational Physics, 1995, 117, (1), pp. 1-19

200 Xiang, Y., Chen, X., and Vlassak, J.J.: ‘The mechanical properties of electroplated Cu thin films measured by means of the bulge test technique’, in Editor (Ed.)^(Eds.): ‘Book The mechanical properties of electroplated Cu thin films measured by means of the bulge test technique’ (Materials Research Society, 2002, edn.), pp. 189-194

201 Ogata, S., Ju, L., and Yip, S.: ‘Ideal pure shear strength of aluminum and copper’, Science, 2002, 298, (5594), pp. 807-811

202 Tschopp, M.A., Spearot, D.E., and McDowell, D.L.: ‘Atomistic simulations of homogenous dislocation nucleation in single crystal’, Modelling Simulation Mater. Sci. Eng. , 2007, (in Print)

203 Wang, Y.M., and Ma, E.: ‘Strain hardening, strain rate sensitivity, and ductility of nanostructured metals’, Materials Science and Engineering A, 2004, 375-377, (1-2 SPEC ISS), pp. 46-52

204 Asaro, R.J., and Suresh, S.: ‘Mechanistic models for the activation volume and rate sensitivity in metals with nanocrystalline grains and nano-scale twins’, Acta Materialia, 2005, 53, (12), pp. 3369-3382

205 Carter, C.B., and Ray, I.L.F.: ‘On the stacking-fault energies of copper alloys’, Philosophical Magazine, 1977, 35, (1), pp. 189-200

206 Mishin, Y., Mehl, M.J., Papaconstantopoulos, D.A., Voter, A.F., and Kress, J.D.: ‘Structural stability and lattice defects in copper: Ab-initio, tight-binding, and embedded-atom calculations’, Physical Review B (Condensed Matter and Materials Physics), 2001, 63, (22), pp. 224106-224101

207 Crow, E.L., and Shimizu, K.: ‘Lognormal Distributions: Theory and Applications’ (CRC Press, 1988. 1988)

208 Johnson, N.L., Kotz, S., and Balakrishnan, N.: ‘Continuous univariate distributions. Vol. 1’ (Wiley, 1994. 1994)

209 Mackenzie, J.K.: ‘Second Paper on Statistics Associated with the Random Disorientation of Cubes’, Biometrika, 1958, 45, (1/2), pp. 229-240

210 Raj, R., and Ashby, M.F.: ‘On grain boundary sliding and diffusional creep’, Metallurgical and Materials Transactions B, 1971, 2, (4), pp. 1113-1127

211 Yin, W.M., and Whang, S.H.: ‘Creep in boron-doped nano crystalline nickel’, Scripta Materialia, 2001, 44, (4), pp. 569-574

212 Yin, W.M., Whang, S.H., and Mirshams, R.A.: ‘Effect of interstitials on tensile strength and creep in nanostructured Ni’, Acta Materialia, 2005, 53, (2), pp. 383-392